

# UNCLASSIFIED

AD NUMBER
AD879498
NEW LIMITATION CHANGE
TO Approved for public release, distribution unlimited
FROM Distribution authorized to U.S. Gov't. agencies and their contractors; Critical Technology; SEP 1970. Other requests shall be referred to Air Force Aero Propulsion Laboratory, Attn: AFTC, Wright-Patterson AFB, OH 45433.
AUTHORITY
AFRPL ltr, 30 Jun 1975

THIS PAGE IS UNCLASSIFIED

THIS REPORT HAS BEEN DELIMITED  
AND CLEARED FOR PUBLIC RELEASE  
UNDER DOD DIRECTIVE 5200.20 AND  
NO RESTRICTIONS ARE IMPOSED UPON  
ITS USE AND DISCLOSURE,

DISTRIBUTION STATEMENT A

APPROVED FOR PUBLIC RELEASE;  
DISTRIBUTION UNLIMITED.

AD879498

AFAPL-TR-70-60

2

# ATTENUATION OF INFRARED RADIATION EMITTED FROM HOT SURFACES BY TRANSPIRATION OF AN ABSORBING GAS

D. H. Quick, Captain, USAF

R. W. Bergstrom, Jr.

E. E. Anderson

et al.

Heat Transfer Laboratory  
School of Mechanical Engineering  
Purdue University  
Lafayette, Indiana

AD No. \_\_\_\_\_  
FILE COPY

TECHNICAL REPORT AFAPL-TR-70-60

September 1970

1971

This document is subject to special export controls and each transmittal to foreign governments or foreign nationals may be made only with prior approval of the Air Force Aero Propulsion Laboratory (APTC), Wright-Patterson Air Force Base, Ohio.

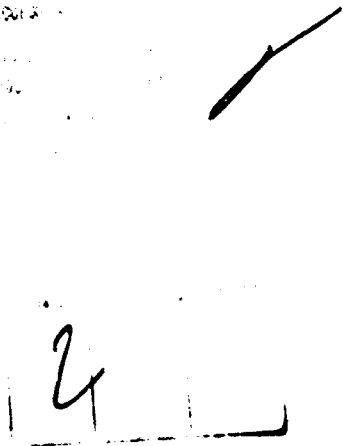
AIR FORCE AERO PROPULSION LABORATORY  
Air Force Systems Command  
Wright-Patterson Air Force Base, Ohio

## NOTICE

When Government drawings, specifications, or other data are used for any purpose other than in connection with a definitely related Government procurement operation, the United States Government thereby incurs no responsibility nor any obligation whatsoever; and the fact that the government may have formulated, furnished, or in any way supplied the said drawings, specifications, or other data, is not to be regarded by implication or otherwise as in any manner licensing the holder or any other person or corporation, or conveying any rights or permission to manufacture, use, or sell any patented invention that may in any way be related thereto.

This document is subject to special export controls and each transmittal to foreign governments or foreign nationals may be made only with prior approval of the Air Force Aero Propulsion Laboratory (APTC), Wright-Patterson Air Force Base, Ohio.

Distribution of this document is limited because it concerns technology identifiable with the DOD Strategic Embargo List.



Copies of this report should not be returned unless return is required by security considerations, contractual obligations, or notice on a specific document.

AFAPL-TR-70-60

**ATTENUATION OF INFRARED RADIATION EMITTED FROM  
HOT SURFACES BY TRANSPIRATION OF AN ABSORBING GAS**

**D. H. Quick, Captain, USAF**

**R. W. Bergstrom, Jr.**

**E. E. Anderson**

**et al.**

**This document is subject to special export controls and each transmittal to foreign governments or foreign nationals may be made only with prior approval of the Air Force Aero Propulsion Laboratory (APTC), Wright-Patterson Air Force Base, Ohio.**

## FOREWORD


This report was prepared by the School of Mechanical Engineering, Purdue University, under Contract No. F 33615-68-C-1642. The program was administered by the Air Force Aero Propulsion Laboratory, Wright-Patterson Air Force Base, Ohio. The Project Engineer was Mr. Kenneth N. Hopkins/APTC.

The study presented herein covers the contracting period from September 3, 1968 through August 31, 1970. The work was performed by E. E. Anderson, R. W. Bergstrom, Jr., F. Dierolf, D. L. McCoy, D. H. Quick, R. Viskanta and E. R. F. Winter. The principal investigators were Professors R. Viskanta and E. R. F. Winter.

This technical report covers the feasibility study on suppression of infrared radiation emitted from a heated porous surface by transpiration of an absorbing gas or gas mixtures through the plate. It contains information which is preliminary in nature and has to be ascertained by more extensive analytical and experimental studies.

The manuscript was released by the authors in September 1970 for publication as an AFAPL Technical Report.

This technical report has been reviewed and is approved.

  
Ernest C. Simpson  
Director, Turbine Engine Division  
Air Force Aero Propulsion Laboratory

## ABSTRACT

Analyses and measurements of attenuation of thermal radiation leaving a heated plate caused by a layer of absorbing gas are discussed. Both a near stagnant fluid and flow over a flat plate were investigated by analysis and experiment. An apparatus in which various porous plates were heated electrically was designed and constructed so that it could be adopted to either the stagnant or flow systems. Radiant energy fluxes in specified wavelength bands leaving the plate were measured with an infrared radiometer developed and built for this purpose.

Specifically, radiometric measurements for the  $4.3\mu$  band of carbon dioxide were made for various plate surface temperatures, injection rates, thicknesses of the absorbing gas layer and viewing angles. In addition to the above parameters the Reynolds number was varied and the effect of the starting length investigated for flow over a flat plate. It was found that the gas is capable of attenuating a significant fraction of the radiation leaving the hot plate. Increases in the plate temperature and gas layer thickness increased the attenuation. For a given mass injection rate of an absorbing gas the attenuation increased with an increase with the Reynolds number. The analyses and experiments show that in order to obtain significant attenuation over large spectral regions a mixture of selected gases or gas particulate mixtures would have to be injected.

## TABLE OF CONTENTS

Section	Page
LIST OF TABLES . . . . .	vi
LIST OF FIGURES. . . . .	vii
LIST OF SYMBOLS. . . . .	x
1. INTRODUCTION . . . . .	1
2. DISCUSSION OF THE PROBLEM . . . . .	3
2.1 Attenuation of Infrared Radiation by Gases. . . . .	3
2.2 Absorption Characteristics of Gases . . . . .	4
2.3 Heat Transfer in Radiating Gases . . . . .	5
3. ATTENUATION OF RADIATION BY A NEAR-STAGNANT ABSORBING GAS . . . . .	16
3.1 Analysis . . . . .	16
3.1.1 Physical Model and Assumptions . . . . .	16
3.1.2 Conservation Equations . . . . .	16
3.1.3 Radiation Flux and Emergent Intensity . . . . .	18
3.1.4 Method of Solution . . . . .	21
3.2 Experiments . . . . .	21
3.2.1 Description of Experimental Facility . . . . .	21
3.2.2 Test Assembly . . . . .	23
3.2.3 Instrumentation and Calibration . . . . .	25
3.2.4 Calibration and Test Procedure . . . . .	27
3.3 Results and Discussion . . . . .	31
3.3.1 Analytical Results . . . . .	31
3.3.2 Experimental Results. . . . .	40
3.3.3 Comparison of Analysis and Experiment . . . . .	40
4. ATTENUATION OF RADIATION BY AN ABSORBING GAS FLOWING OVER A HOT PLATE . . . . .	46
4.1 Analysis . . . . .	46
4.1.1 Physical Model and Assumptions . . . . .	46
4.1.2 Conservation Equations . . . . .	48
4.1.3 Justification for Decoupling of Convection from Radiation . . . . .	50
4.1.4 Integral Forms of the Conservation Equations . . . . .	51



Section	Page
4.1.5 Solution of Conservation Integral Equations . . . . .	53
4.1.6 Prediction of Attenuation . . . . .	57
4.2 Experiment . . . . .	58
4.2.1 Description of Experimental Facility . . . . .	58
4.2.2 Test Assembly . . . . .	60
4.2.3 Instrumentation and Calibration . . . . .	60
4.2.4 Test Procedure. . . . .	63
4.3 Results and Discussion . . . . .	66
4.3.1 Analytical Results . . . . .	66
4.3.2 Experimental Results. . . . .	73
4.3.3 Comparison of Analysis and Experiment . . . . .	81
5. CONCLUSIONS AND RECOMMENDATIONS . . . . .	87
6. REFERENCES . . . . .	89

## LIST OF TABLES

Table	Page
1. Spectral Absorption Characteristics of Various Gases . . . . .	6
2. Hazardous Properties of Various Gases . . . . .	14
3. Effect of Blowing Reynolds Number on Attenuation for $\delta = 7.62$ cm, $T_p = 822^\circ\text{K}$ and $\theta = 0^\circ$ . . . . .	42
4. Effects of Plate Temperature and Gas Layer Thickness on Emergent Band Intensity for $\theta = 0^\circ$ . . . . .	42
5. Effect of Viewing Angle on Attenuation for $\delta = 5.08$ cm, $T_p = 960^\circ\text{K}$ and $Re = 29$ . . . . .	42
6. Effect of Injected Mass Flux (lbs/ft <sup>2</sup> sec) on Attenuation ( $I^*$ ) for Porous Heated Plate with $x_0 = 1$ in, $x = 2\text{-}1/2$ in, $T_w \approx 1460^\circ\text{R}$ and $\theta = 0^\circ$ . . . . .	79
7. Effect of Injected Mass Flux (lbs/ft <sup>2</sup> sec) on Attenuation ( $I^*$ ) for Solid Heated Plate with $x_0 = 3$ in, $x = 5$ in, $T_w \approx 1460^\circ\text{R}$ and $\theta = 0^\circ$ . . . . .	79

## LIST OF FIGURES

Figure	Page
1. Spectral Absorptance of Acetylene, Allene, Ammonia, and 1.3 Butadiene. . . . .	7
2. Spectral Absorptance of n-Butane, Carbon Dioxide, Carbon Monoxide, and Cyanogen. . . . .	8
3. Spectral Absorptance of Cyclopropane, Diazo-methane, Dimethyl Amine, and Dimethyl Ether . . . . .	9
4. Spectral Absorptance of Ethane, Ethylene, Isobutane, and Methane . . . . .	10
5. Spectral Absorptance of Methyl Chloride, Methyl Mercaptan, Monoethyl Amine, and Monomethyl Amine . . . . .	11
6. Spectral Absorptance of Nitric Oxide, Nitrous Oxide, Propane, and Propylene. . . . .	12
7. Spectral Absorptance of Propyne, Sulfur Dioxide, Trimethylamine, and Vinyl Chloride . . . . .	13
8. Physical Model and Coordinate System . . . . .	17
9. Photograph of Test Apparatus with a Radiometer Mounted Below the Test Section . . . . .	22
10. Sectional View of Test Assembly . . . . .	24
11. Sectional View of Gas Temperature Probe Tip . . . . .	26
12. Sectional View of Radiometer . . . . .	27
13. Spectral Transmittance Curve of 4.35 $\mu$ Wide Band Pass Filter. . . . .	28
14. Thermopile Calibration Curve . . . . .	30
15. Effect of Injection Rate on the Temperature Distribution; CO <sub>2</sub> , $\delta$ = 6 cm, T <sub>p</sub> = 836°K, $\epsilon$ = 0.6 . . . . .	33
16. Effect of Injection Rate on the Mass Fraction Distribution; CO <sub>2</sub> , $\delta$ = 6 cm, T <sub>p</sub> = 836°K, $\epsilon$ = 0.6 . . . . .	34

Figure	Page
17. Effect of Injection Rate on the Normalized Emergent Band Intensity; $\text{CO}_2$ , $\delta = 6$ cm, $T_0 = T_p = 836^\circ\text{K}$ , $\epsilon = 0.6$ . . . . .	35
18. Effect of the Plate Emittance on the Normalized Emergent Band Intensity; $\text{CO}_2$ , $\text{Re} = \delta = 2$ cm, $T_0 = T_p = 836^\circ\text{K}$ . . . . .	36
19. Dependence of Emergent Band Intensity on Layer Thickness; $\text{CO}_2$ , $\text{Re} = 2$ , $\epsilon = 0.6$ . . . . .	38
20. Emergent Intensity for $\text{CH}_4$ and $\text{SO}_2$ Gas Layers; $T_0 = T_p = 836^\circ\text{K}$ , $\epsilon = 0.6$ . . . . .	39
21. Measured Temperature Distribution with $\text{CO}_2$ Gas . . . . .	41
22. Effect of Gas Layer Thickness on Attenuation; $m = 0.01$ lb/min, $\theta = 0$ . . . . .	43
23. Normal Spectral Emittance of Oxidized and Unoxidized Poroloy Plates . . . . .	44
24. Physical Models of the Problem . . . . .	47
25. Schematic Diagram of the Facility . . . . .	59
26. Photograph of the Intake Side of the Wind Tunnel . . . . .	61
27. Photograph of the Test Section . . . . .	62
28. Schematic Diagram of the Gas Chromatograph . . . . .	64
29. Flow Diagram of the Gas Chromatograph . . . . .	65
30. Variation of the Parameters $\psi$ , $\lambda_v$ , $\lambda_t$ and $\lambda_m$ with $\zeta$ for Different $\Gamma$ ; $\zeta_0 = 0$ , $\text{Pr} = 0.7$ , $\text{Sc} = 0.5$ . . . . .	68
31. Variation of the Parameters $\psi$ , $\lambda_v$ , $\lambda_t$ and $\lambda_m$ with $\zeta - \zeta_0$ for Different $\Gamma$ ; $\zeta_0 = 5.0$ , $\text{Pr} = 0.7$ , $\text{Sc} = 0.5$ . . . . .	69
32. Variation of Wall Temperature and Wall Mass Fraction Along the Plate for Different $\Gamma$ ; $\zeta_0 = 0$ , $\text{Pr} = 0.7$ , $\text{Sc} = 0.5$ . . . . .	70
33. Temperature Distribution in the Boundary Layer for Different $\phi$ ; $\zeta_0 = 0$ , $\text{Pr} = 0.7$ , $\text{Sc} = 0.5$ . . . . .	71
34. Effect of $\phi$ and $\Gamma$ on the Normalized Emergent Spectral Intensity with $\text{CO}_2$ Injection; $x_0 = 0$ , $\text{Re}_x = 10 \times 10^4$ , $T_\infty = 530^\circ\text{R}$ , $\epsilon = 1$ . . . . .	72

Figure	Page
35. Effect of Injection on the Normalized Emergent Band Intensity; $x_0 = 0$ , $T_\infty = 530^\circ\text{R}$ . . . . .	73
36. Schlieren Photographs of Boundary Layer Development with $\text{CO}_2$ Injection through a Cold Porous Plate. . . . .	74
37. Schlieren Photographs Illustrating the Effect of Free Stream Velocity on Boundary Layer Development with $\text{CO}_2$ Injection through a Cold Porous Plate . . . . .	75
38. Measured Velocity Profile in the Boundary Layer with $\text{CO}_2$ Injection through a Heated Porous Plate; $x_0 = 1$ in, $x = 2\text{-}1/2$ in, $\text{Re}_x = 5.75 \times 10^4$ , $T_\infty = 530^\circ\text{R}$ , $T_w = 1460^\circ\text{R}$ . . . . .	76
39. Measured Temperature Profile in the Boundary Layer with $\text{CO}_2$ Injection through a Heated Porous Plate; $x_0 = 1$ in, $x = 2\text{-}1/2$ in, $\text{Re}_x = 5.75 \times 10^4$ , $T_\infty = 530^\circ\text{R}$ , $T_w = 1460^\circ\text{R}$ . . . . .	77
40. Measured Mass Fraction Profile in the Boundary Layer with $\text{CO}_2$ Injection through a Heated Porous Plate; $x_0 = 1$ in, $x = 2\text{-}1/2$ in, $T_\infty = 530^\circ\text{R}$ , $T_w = 1460^\circ\text{R}$ . . . . .	78
41. Effect of $\text{CO}_2$ Injection on Measured Band Attenuation with a Heated Porous Plate; $x_0 = 1$ in, $x = 2\text{-}1/2$ in, $T_\infty = 530^\circ\text{R}$ , $T_w = 1460^\circ\text{R}$ . . . . .	80
42. Effect of $\text{CO}_2$ Injection through a Cold Porous Leading Edge on Measured Band Attenuation with a Solid Heated Plate; $x_0 = 3$ in, $x = 5$ in, $T_\infty = 530^\circ\text{R}$ , $T_w = 1460^\circ\text{R}$ . . . . .	82
43. Comparison between Analysis and Experiment of Temperature Profiles in the Boundary Layer with $\text{CO}_2$ Injection through a Heated Porous Plate; $x_0 = 1$ in, $x = 2\text{-}1/2$ in, $\text{Re}_x = 5.75 \times 10^4$ , $T_\infty = 530^\circ\text{R}$ , $T_w = 1460^\circ\text{R}$ . . . . .	83
44. Comparison between Analysis and Experiment of Mass Fraction Profiles in the Boundary Layer with $\text{CO}_2$ Injection through a Heated Porous Plate; $x_0 = 1$ in, $x = 2\text{-}1/2$ in, $T_\infty = 530^\circ\text{R}$ , $T_w = 1460^\circ\text{R}$ . . . . .	84
45. Comparison between Analysis and Experiment of Normalized Band Attenuation with $\text{CO}_2$ Injection through a Porous Heated Plate; $x_0 = 1$ in, $x = 2\text{-}1/2$ in, $T_\infty = 530^\circ\text{R}$ , $T_w = 1460^\circ\text{R}$ , $\epsilon = 0.7$ . . . . .	86

## LIST OF SYMBOLS

$A$	=	Area or total band absorption
$a$	=	Exponent in Eq. (4.12)
$a_i$	=	Constants in Eq. (4.24) or in Eq. (3.18)
$A_0$	=	Band width parameter in Eq. (3.27)
$Bo$	=	Boltzmann number, $\sigma T^3/mc_p$
$b$	=	Exponent in Eq. (3.12) and (4.12)
$b_i$	=	Constants in Eq. (4.25) or in Eq. (3.18)
$C_0^2$	=	Line intensity to spacing ratio in Eq. (3.27)
$c_i$	=	Constants in Eq. (4.26)
$c_p$	=	Specific heat at constant pressure
$D$	=	Diffusion coefficient or diameter
$E_b$	=	Black-body emissive power
$E_n$	=	Exponential integral function of order $n$
$F$	=	Radiative flux
$Gr$	=	Grashoff number, $g\beta\delta^3 T_r/\nu^2$
$I$	=	Intensity of radiation
$I^*$	=	Normalized emergent band intensity, Eq. (2.5)
$j_i$	=	Diffusional mass flux of the $i$ -th species defined by Eq. (3.3)
$k$	=	Thermal conductivity
$M$	=	Molecular weight also Mach number
$m$	=	Injected mass flow rate, $\rho_w v_w$
$p$	=	Pressure

$Pe$  = Peclet number,  $(m\delta c_p/k) = Pr \cdot Re$   
 $Pr$  = Prandtl number,  $\mu c_p/k$   
 $q$  = Heat flux  
 $R$  = Gas constant  
 $Re$  = Blowing Reynolds number,  $m\delta/\mu$   
 $Re_x$  = Local Reynolds number,  $u_\infty x/\nu_\infty$   
 $q_t$  = Total imposed heat flux at the plate  
 $Sc$  = Schmidt number,  $\nu/D$   
 $T$  = Temperature  
 $t$  = Transmittance  
 $u$  = Velocity component parallel to the plate  
 $v$  = Velocity component perpendicular to the plate  
 $w_i$  = Mass fraction,  $\rho_i/\rho$   
 $x$  = Coordinate parallel to the surface  
 $y$  = Coordinate normal to the surface also molar fraction

### Greek Symbols

$\alpha$  = Thermal diffusion coefficient  
 $\beta$  = Thermal expansion coefficient  
 $\Gamma$  = Dimensionless parameter,  $[(T_c/T_\infty) - (q_r - q_t)/c_{p_2} \rho_w v_w T_\infty]$   
 $\delta$  = Layer thickness or boundary layer thickness  
 $\epsilon$  = Emissivity  
 $\zeta$  = Dimensionless parameter,  $Re_x \phi^2$   
 $\eta$  = Dimensionless (transformed) boundary layer thickness,  $\tau/\delta$   
 $\theta$  = Dimensionless temperature,  $T/T_r$   
 $\theta$  = Polar angle  
 $\kappa$  = Absorption coefficient

$\Lambda$	=	Dimensionless boundary layer thickness, $\rho_{\infty} u_{\infty} \delta / \mu_{\infty}$
$\lambda$	=	Wavelength
$\mu$	=	Dynamic viscosity, micron or $1/\cos\theta$
$\nu$	=	Kinematic viscosity, or frequency
$\xi$	=	Dimensionless length, $y/\delta$
$\rho$	=	Density
$\sigma$	=	Stefan-Boltzmann constant
$\tau$	=	Optical depth
$\tau_0$	=	Optical thickness of layer
$\phi$	=	Injection parameter, $\rho_w v_w / \rho_{\infty} u_{\infty}$
$\psi$	=	Parameter, $(\rho_w v_w \delta / \mu_{\infty}) = \phi \Lambda$
$\omega$	=	Wave number, $1/\lambda$

### Subscripts

$c$	=	Refers to band center
$e$	=	Refers to external
$m$	=	Refers to mass
$p$	=	Refers to plate
$r$	=	Reference condition
$t$	=	Refers to thermal
$w$	=	Refers to wall
$v$	=	Refers to velocity
$1$	=	Main stream gas
$2$	=	Injected species
$\infty$	=	Free stream
$\lambda, \nu, \omega$	=	Spectral quantities



### Superscripts

+ = Dimensionless quantity

## 1. INTRODUCTION

The emission of thermal radiation from high temperature bodies has become of concern to design engineers. The structural components of a jet engine, for example, and the exhaust gases emit not only radiation in the visible but also in the infrared range of the spectrum. Furthermore, the soot and carbon particles suspended in the exhaust stream contribute to the radiation. The shielding of components and/or the environment from intense radiation can be an important objective in the design of aircraft and missiles, airfoil surfaces, etc. In most applications, shielding is used to reduce the heating or cooling of a system component; but radiant energy received by a sensor from a source may also be reduced by similar means to decrease the probability of detection.

The infrared radiation leaving a source may be decreased, for instance, by geometrical design and/or reduction of emittance. The radiation can also be reduced by transpiration of radiation—absorbing gas into the gas stream through a porous material. The injection of an absorbing fluid into the gas stream may shield the hot surfaces from an observer and will also cool the surfaces and thus reduce the radiant energy emitted. The extent of the second benefit would be increased by injecting a cold liquid which would vaporize as it transpires through the porous structure. A liquid additive might be preferred over a gaseous one since the storage volume for a given mass would be an order of magnitude smaller. The infrared suppression scheme would be used only when need arises, and the consumption of the radiation absorbing fluid could be kept at a minimum.

The present study has been conceived as an analytical and experimental investigation of the feasibility of attenuating the infrared radiation emitted from hot surfaces by injection of an absorbing gas between the source and the detector. The objective of the research program was to determine how effectively the transpiration of an absorbing gas attenuates the radiation. The purpose of the investigation conducted was twofold and can best be described by briefly summarizing the essential elements of the research program:

1. Prediction of attenuation of radiation emitted from a hot surface through which an absorbing emitting gas is injected.

2. Performance of experiments to verify the analytically predicted attenuation.

The program as stated above is too ambitious and too inclusive to be treated thoroughly within the limits of the time and funding of the program. The specific tasks undertaken were the following:

1. Prediction and measurement of attenuation by a near-stagnant layer of absorbing gas.
2. Prediction and measurement of attenuation of infrared radiation emitted by a hot, flat plate through or ahead of which an absorbing gas is injected into the stream.

In Chapter 2 the problem is discussed in more detail and the literature is reviewed. Chapter 3 describes the analysis and apparatus used for the investigation of attenuation of radiation by a near-stagnant layer of radiating gas and the comparison of the results is given. In Chapter 4, an analysis is presented and the experimental facility is described for the study of attenuation of radiation in boundary layer flow over a flat plate. Detailed comparison is made between predicted attenuation and experimentally obtained results. Chapter 5 contains conclusions and recommendations.

## 2. DISCUSSION OF THE PROBLEM

### 2.1 Attenuation of Infrared Radiation by Gases

To be specific, consider a plane layer of absorbing-emitting gas of thickness  $\delta$  which is in contact with a hot surface. The spectral intensity of radiation emerging from the top of the layer,  $I_\lambda(\delta, \theta)$ , neglecting scattering and assuming local thermodynamic equilibrium is given by [1]\*

$$I_\lambda(\delta, \theta) = I_{\ell\lambda}(0, \theta) e^{-\int_0^\delta \kappa_\lambda dy / \cos\theta} + \int_0^\delta I_{b\lambda}(y) e^{-\int_y^\delta \kappa_\lambda dt / \cos\theta} \kappa_\lambda dy / \cos\theta \quad (2.1)$$

In writing this equation we have assumed that the surface and the layer are axisymmetric, i.e., the radiation surface characteristics and the spectral intensity are independent of the azimuthal angle. The physical meaning of Eq. (2.1) is clear: It expresses the fact that the intensity emerging from the layer in a given direction,  $\theta$ , results from a contribution due to radiation leaving the boundary plane,  $y = 0$ , attenuated by the factor  $\exp[-\int_0^\delta \kappa_\lambda dy / \cos\theta]$  and contributions from gaseous emission at all interior points,  $y$ , reduced by the factor  $\exp[-\int_y^\delta \kappa_\lambda dt / \cos\theta]$  to allow for absorption by the intervening gas. The spectral intensity of radiation leaving the surface  $I_{\ell\lambda}(0, \theta)$  is the sum of the emitted and reflected radiation and can be expressed as [1]

$$I_{\ell\lambda}(0, \theta) = \epsilon_\lambda(\theta) I_{b\lambda}(T_p) + 2 \int_{\pi}^{\pi/2} \left[ I_{e\lambda}(\theta') e^{\int_0^\delta \kappa_\lambda dy / \cos\theta'} - \int_0^\delta I_{b\lambda}(y) e^{\int_0^y \kappa_\lambda dt / \cos\theta'} \kappa_\lambda dy / \cos\theta' \right] \rho_\lambda(\theta \leftrightarrow \theta') \sin\theta' \cos\theta' d\theta' \quad (2.2)$$

where  $\epsilon_\lambda(\theta)$  is the directional emittance,  $\rho_\lambda(\theta' \leftrightarrow \theta)$  is the bi-directional reflectance, and  $I_{e\lambda}$  is the intensity of external incident radiation. The terms in Eq. (2.2) represent the surface emission, the reflection of the energy incident on the

\* Numbers in brackets denote references.

layer after being attenuated by the layer and the reflection of attenuated gaseous emission, respectively. For a transparent layer of gas  $\kappa_\lambda = 0$  and Eq. (2.1) reduces to

$$I_\lambda(\delta, \theta) = I_{\ell\lambda}(0, \theta) \quad (2.3)$$

The effectiveness of a layer of a participating gas placed over a surface to absorb radiation can be expressed by the normalized spectral intensity, which is defined as the ratio of intensity at the edge of the layer to the intensity leaving the surface if the gas layer was transparent, i.e.,

$$I_\lambda^*(\delta, \theta) = I_\lambda(\delta, \theta) / I_{\ell\lambda}(0, \theta) \Big|_{\text{Transparent}} \quad (2.4)$$

and serves as a measure of the spectral attenuation. Gases absorb and emit radiation in bands, and hence the normalized intensity for band  $i$  is given by

$$I_{\Delta\lambda_i}^*(\delta, \theta) = \int_{\Delta\lambda_i} I_\lambda^*(\delta, \theta) d\lambda \quad (2.5)$$

The linear (volumetric) spectral absorption coefficient,  $\kappa_\lambda$ , does not only depend on the nature of the gas but on concentration, temperature and total pressure of the gas. The spectral absorption coefficient can also be expressed as

$$\kappa_\lambda = \rho\kappa'_\lambda = p\kappa''_\lambda \quad (2.6)$$

where  $\kappa'_\lambda$  and  $\kappa''_\lambda$  are referred to as the spectral mass absorption coefficients. The quantity  $\rho\kappa'_\lambda / N_g$ , where  $N_g$  is the number density (number per unit volume) of gas molecules, has the dimension of an area and can be interpreted as a cross-section for absorption of radiation of wavelength  $\lambda$ . Since the Planck's function  $I_{b\lambda}$  is a function of temperature it is clear from Eqs. (2.4), (2.5) and (2.6) that the prediction of the normalized (spectral or band) intensity emerging from the gas layer is straight forward once the heat and mass transfer problem has been solved.

## 2.2 Absorption Characteristics of Gases

The description of the radiation properties of gases from a quantum mechanical viewpoint is discussed in Reference [2]. The problem of predicting the properties of gases is very complex and has been the subject of much recent work [2, 3]. The experimental evaluation of the spectral absorption coefficient is extremely difficult and time consuming because of a large number of independent parameters. In theory, it is possible to predict it from quantum mechanics; however, for gases the complexity of the calculations makes this approach in general impractical. Hence the absorption properties are conveniently taken from experimental data and/or from analytical models [3].

An extensive bibliography on infrared radiative properties of gases has been compiled recently [4], and there is no need to repeat that survey.

A literature search was undertaken to compile a list of gases which have desirable absorption characteristics in the infrared region of the spectrum and could be employed as injected gases. The common gases such as oxygen, nitrogen, and hydrogen have symmetrical molecules and for all practical purposes are transparent to thermal radiation. On the other hand, gases and vapors such as carbon dioxide, sulfur dioxide, ammonia, water vapor, carbon monoxide and various hydrocarbons absorb and emit thermal radiation in bands. For example, the important radiation bands for  $\text{CO}_2$ , lie in wavelength region, 2.36 to 3.02 $\mu$ , 4.01 to 4.80 $\mu$ , and 12.5 to 16.5 $\mu$  [5]. A list of 28 absorbing gases is presented in Table 1. Figures 1 through 7 illustrate the infrared transmission spectra of these gases. All of the spectral data were obtained with a Perkin-Elmer Model 21 spectrometer having the following features; sodium chloride optics, 10-cm gas layer cell at room temperature (23°C) with sodium chloride windows, and a wavelength range from 2 to 15  $\mu$  [6].

Table 2 contains brief qualitative remarks as to the toxicity, fire, and explosive hazards of the gases. The information contained in Table 2 was taken from Reference [7]. It should be noted that, in general, those substances classified as having "slight toxicity" produce changes in the human body which are readily reversible and which will disappear following termination of exposure, either with or without medical treatment. Those substances classified as having "moderate toxicity" may produce irreversible as well as reversible changes in the human body. These changes are not of such severity as to threaten life or produce serious permanent physical impairment. "Severe toxicity" includes those substances which on a single exposure lasting seconds or minutes can cause injury sufficient to threaten life or to cause permanent impairment, disfigurement, or irreversible changes.

Since the absorption properties of carbon dioxide are well known and the gas is relatively non-hazardous, it was chosen as working fluid for this investigation. The fundamental 4.3 $\mu$  band was chosen for the study. The choice of the gas and the band was somewhat arbitrary.

### 2.3 Heat Transfer in Radiating Gases

The presence of a finite interfacial velocity normal to a surface where simultaneous heat, mass and momentum transfer are taking place alters appreciably the temperature, concentration and velocity profiles. It has been found that one of the most effective ways of cooling a high performance surface is that of mass transfer cooling which involves the injection of a foreign gas (or liquid) into the boundary layer. A detailed

Table 1. Spectral Absorption Characteristics  
of Various Gases

Spectrum No.	Compound	Chemical Formula
3	Acetylene	HC : CH
5	Allene	CH <sub>2</sub> : C : CH <sub>2</sub>
6	Ammonia	NH <sub>3</sub>
9	1.3 Butadiene	CH <sub>2</sub> : CH • CH : CH <sub>2</sub>
10	n-Butane	CH <sub>3</sub> CH <sub>2</sub> CH <sub>2</sub> CH <sub>3</sub>
11	Carbon Dioxide	CO <sub>2</sub>
12	Carbon Monoxide	CO
13	Cyanogen	(CN) <sub>2</sub>
14	Cyclopropane	(CH <sub>2</sub> ) <sub>3</sub>
15	Diazomethane	CH <sub>2</sub> N <sub>2</sub>
18	Dimethylamine	(CH <sub>3</sub> ) <sub>2</sub> NH
19	Dimethyl Ether	CH <sub>3</sub> O CH <sub>3</sub>
22	Ethane	CH <sub>3</sub> CH <sub>3</sub>
28	Ethylene	CH <sub>2</sub> : CH <sub>2</sub>
38	Isobutane	(CH <sub>3</sub> ) <sub>2</sub> CH
39	Methane	CH <sub>4</sub>
42	Methyl Chloride	CH <sub>3</sub> Cl
43	Methyl Mercaptan	CH <sub>3</sub> SH
45	Monoethylamine	C <sub>2</sub> H <sub>5</sub> NH <sub>2</sub>
46	Monomethylamine	CH <sub>3</sub> NH <sub>2</sub>
48	Nitric Oxide	NO
56	Nitrous Oxide	N <sub>2</sub> O
58	Propane	CH <sub>3</sub> CH <sub>2</sub> CH <sub>3</sub>
59	Propylene	CH <sub>3</sub> • CH : CH <sub>2</sub>
60	Propyne	CH <sub>3</sub> • C : CH
61	Sulfur Dioxide	SO <sub>2</sub>
64	Trimethylamine	(CH <sub>3</sub> ) <sub>3</sub> N
66	Vinyl Chloride	CH <sub>2</sub> : CH • Cl

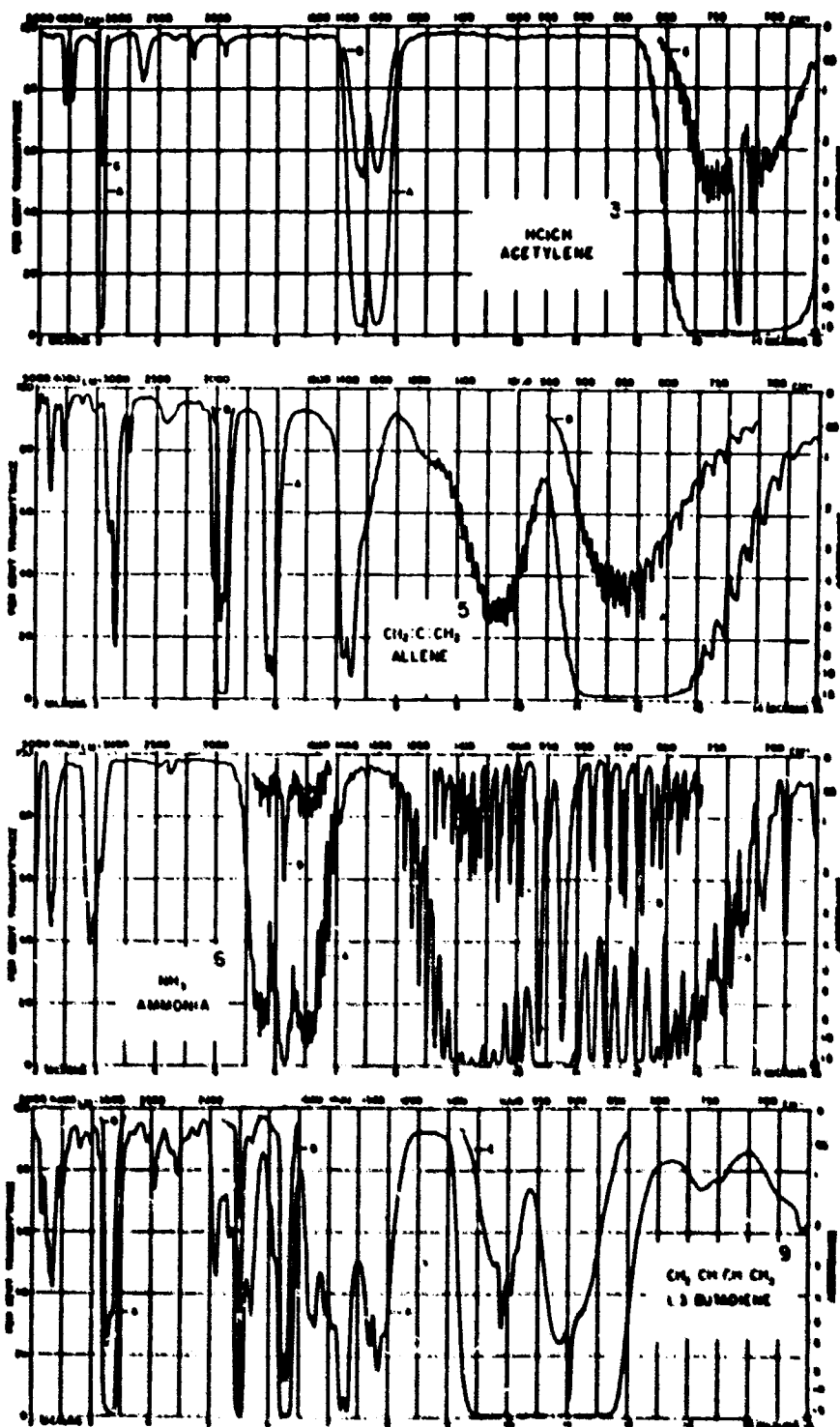
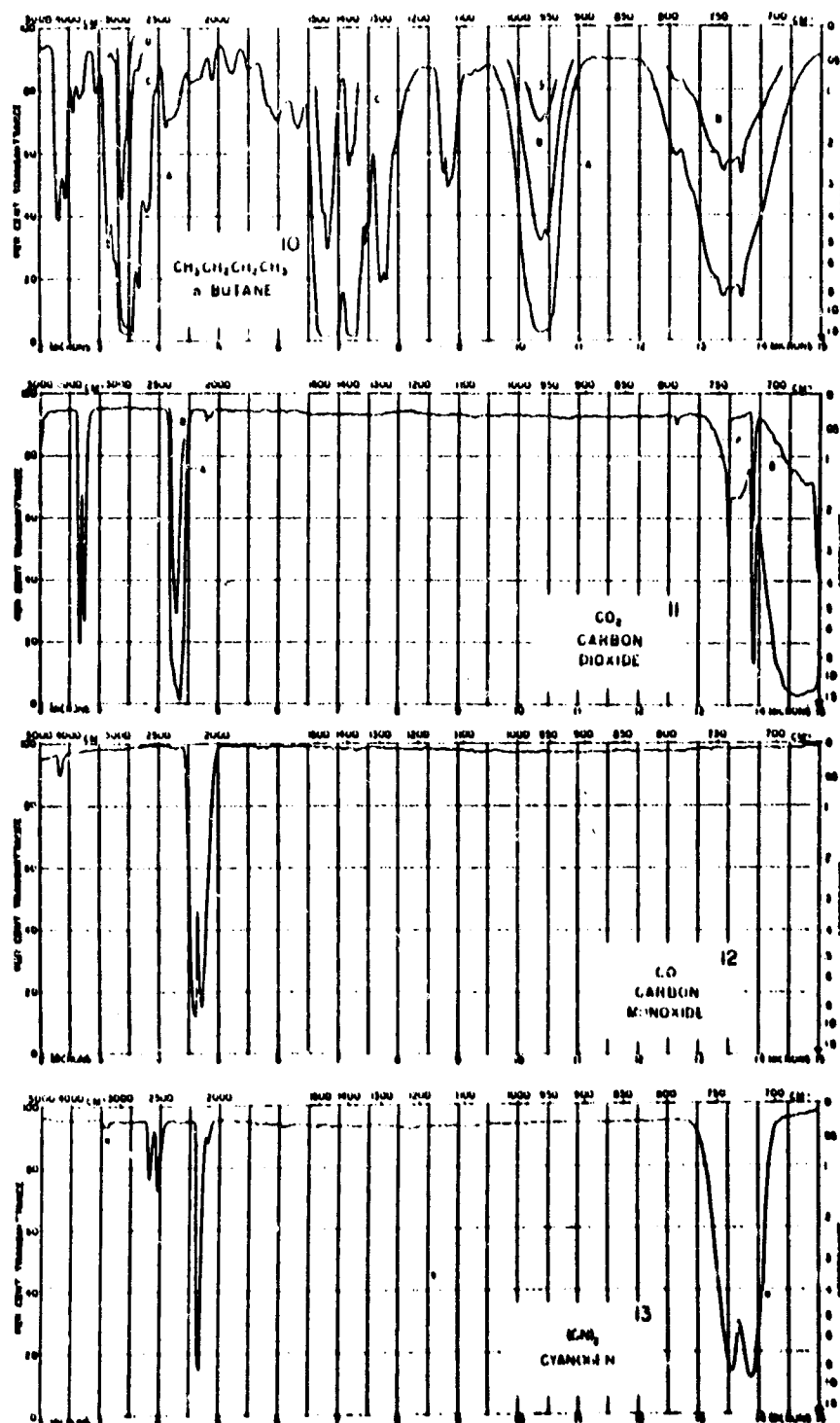


Figure 1. Spectral Absorbance of Acetylene, Allene, Ammonia, and 1,3 Butadiene

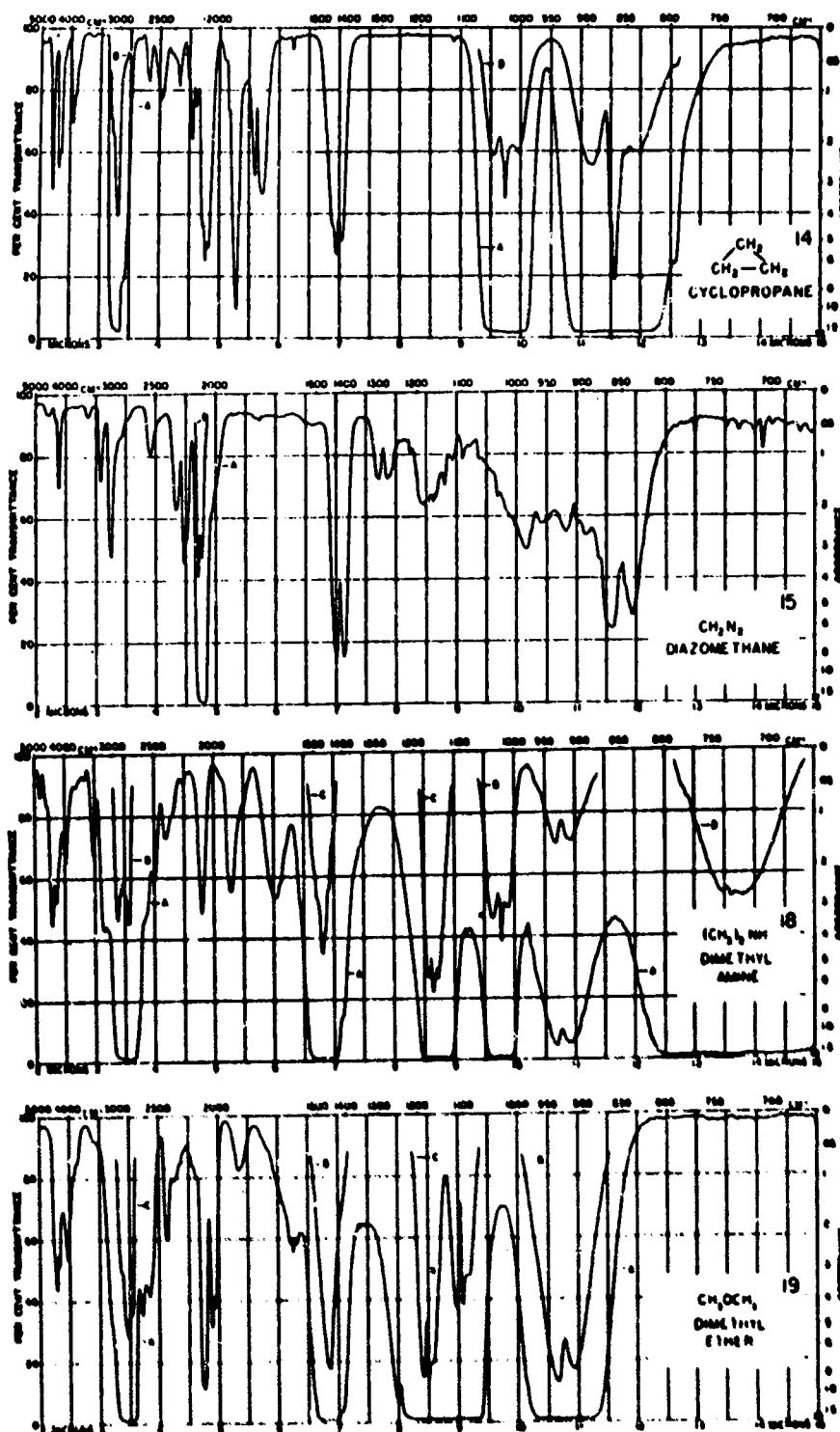




Curve letter  
Pressure, mm.  
Resolution

No. 10  $\frac{4}{100}$   $\frac{2}{100}$   $\frac{2}{100}$   $\frac{2}{100}$  No. 11  $\frac{4}{100}$   $\frac{2}{100}$  No. 12  $\frac{4}{100}$  No. 13  $\frac{4}{100}$

Figure 2. Spectral Absorptance of n-Butane, Carbon Dioxide, Carbon Monoxide, and Cyanogen



Curve letter  
Preparation, mm.  
Resolution

No. 14	$\frac{4}{700}$	$\frac{8}{900}$	No. 15	$\frac{4}{700}$	$\frac{8}{900}$	No. 18	$\frac{4}{700}$	$\frac{8}{900}$	$\frac{9}{1000}$	No. 19	$\frac{4}{700}$	$\frac{8}{900}$	$\frac{9}{1000}$
--------	-----------------	-----------------	--------	-----------------	-----------------	--------	-----------------	-----------------	------------------	--------	-----------------	-----------------	------------------

Figure 3. Spectral Absorptance of Cyclopropane, Diazo-  
methane, Dimethyl Amine, and Dimethyl Ether

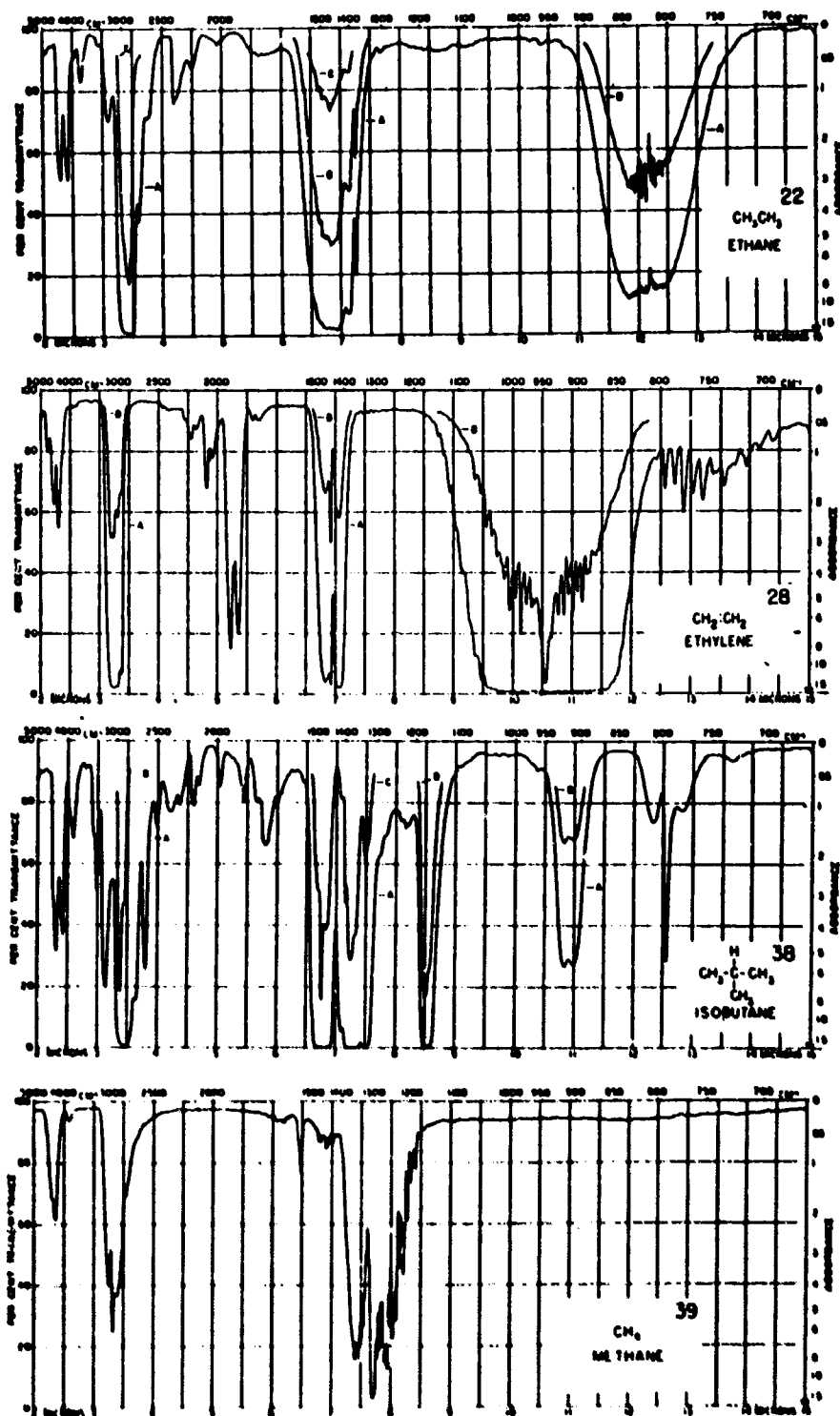


Figure 4. Spectral Absorptance of Ethane, Ethylene, Isobutane, and Methane

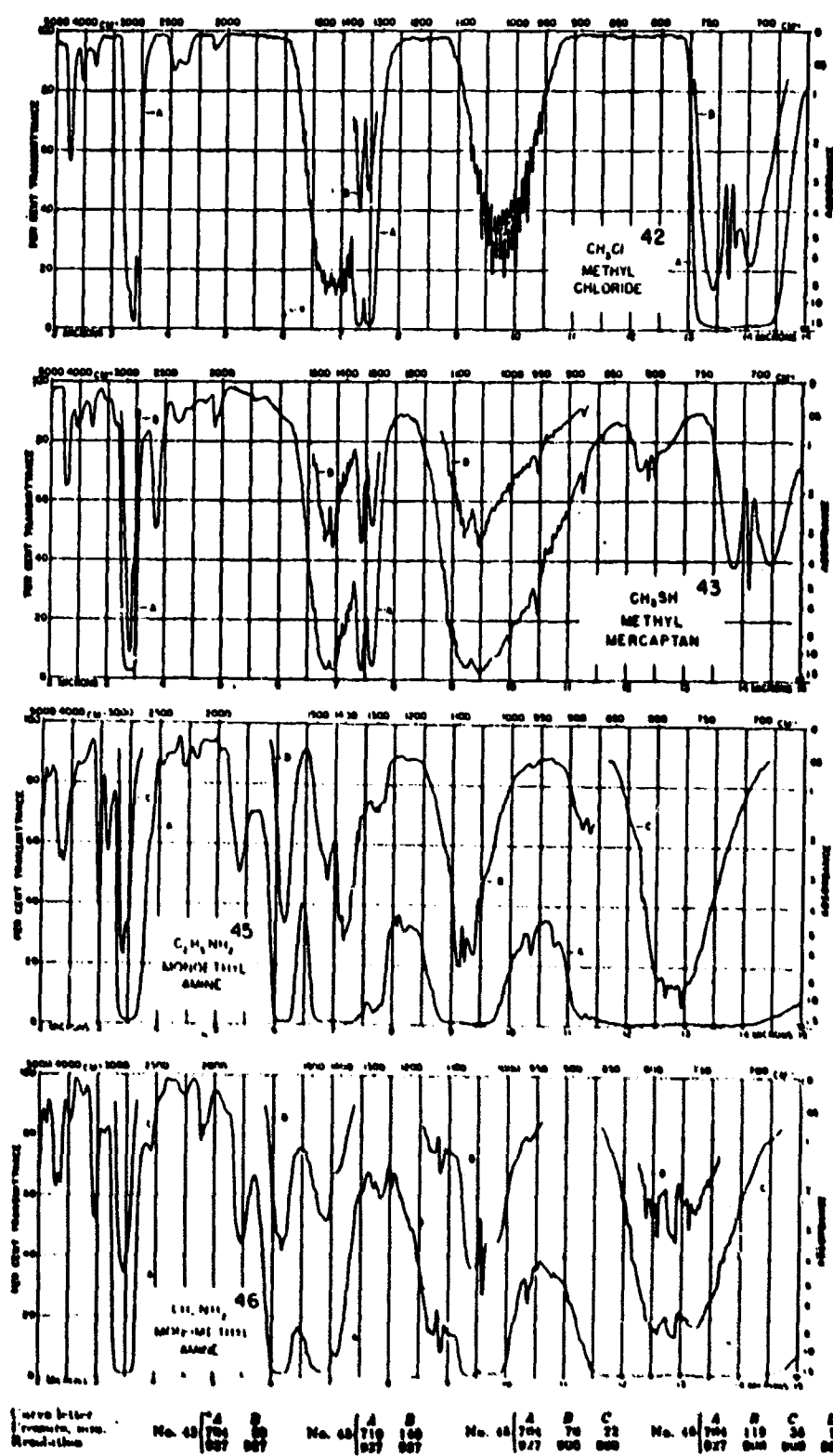
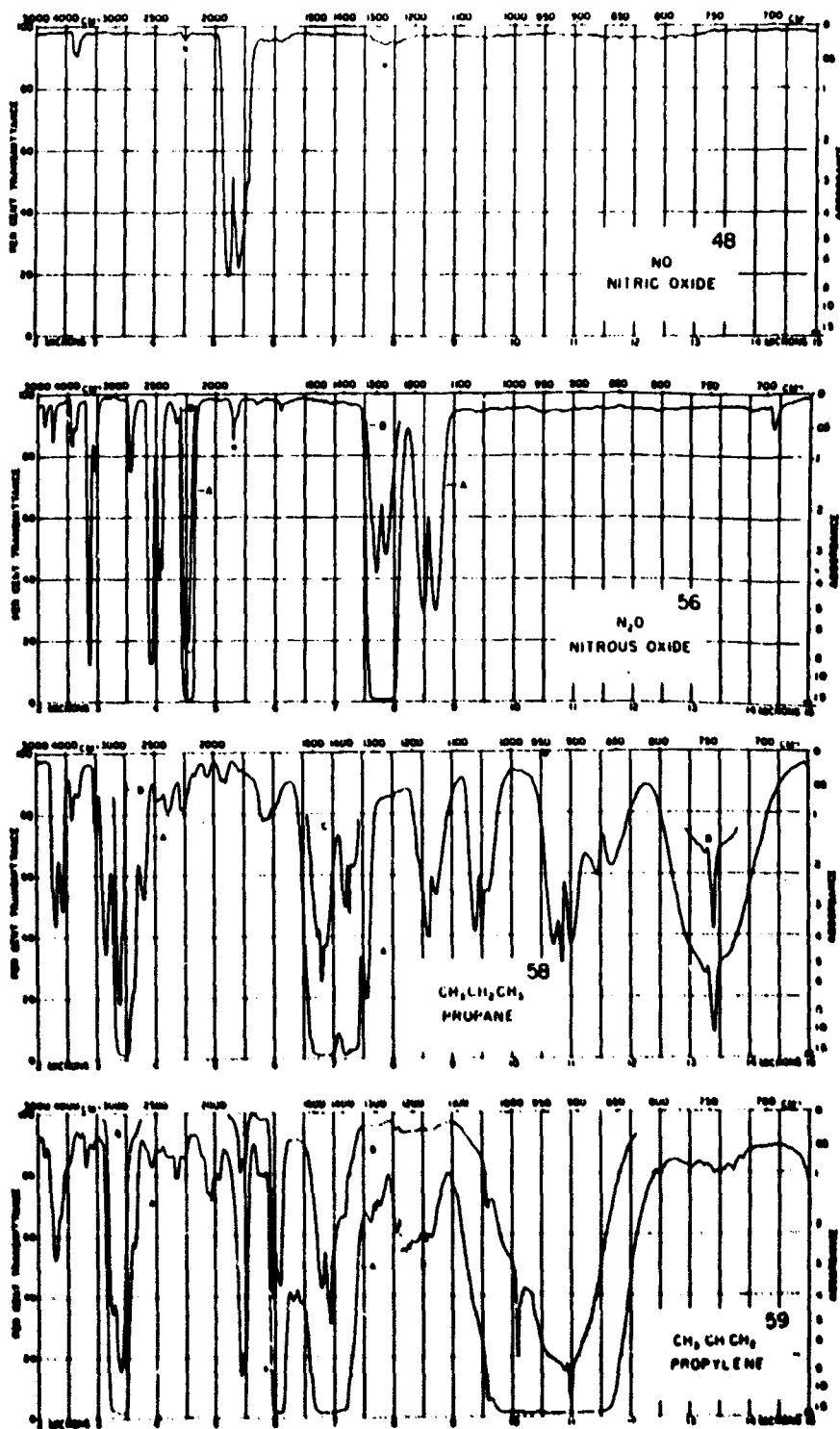


Figure 5. Spectral Absorptance of Methyl Chloride, Methyl Mercaptan, Monoethyl Amine, and Monomethyl Amine



Curve Number: No. 48 (710) 527      No. 56 (721) 528      No. 58 (727) 529      No. 59 (719) 530

Figure 6. Spectral Absorptance of Nitric Oxide, Nitrous Oxide, Propane, and Propylene

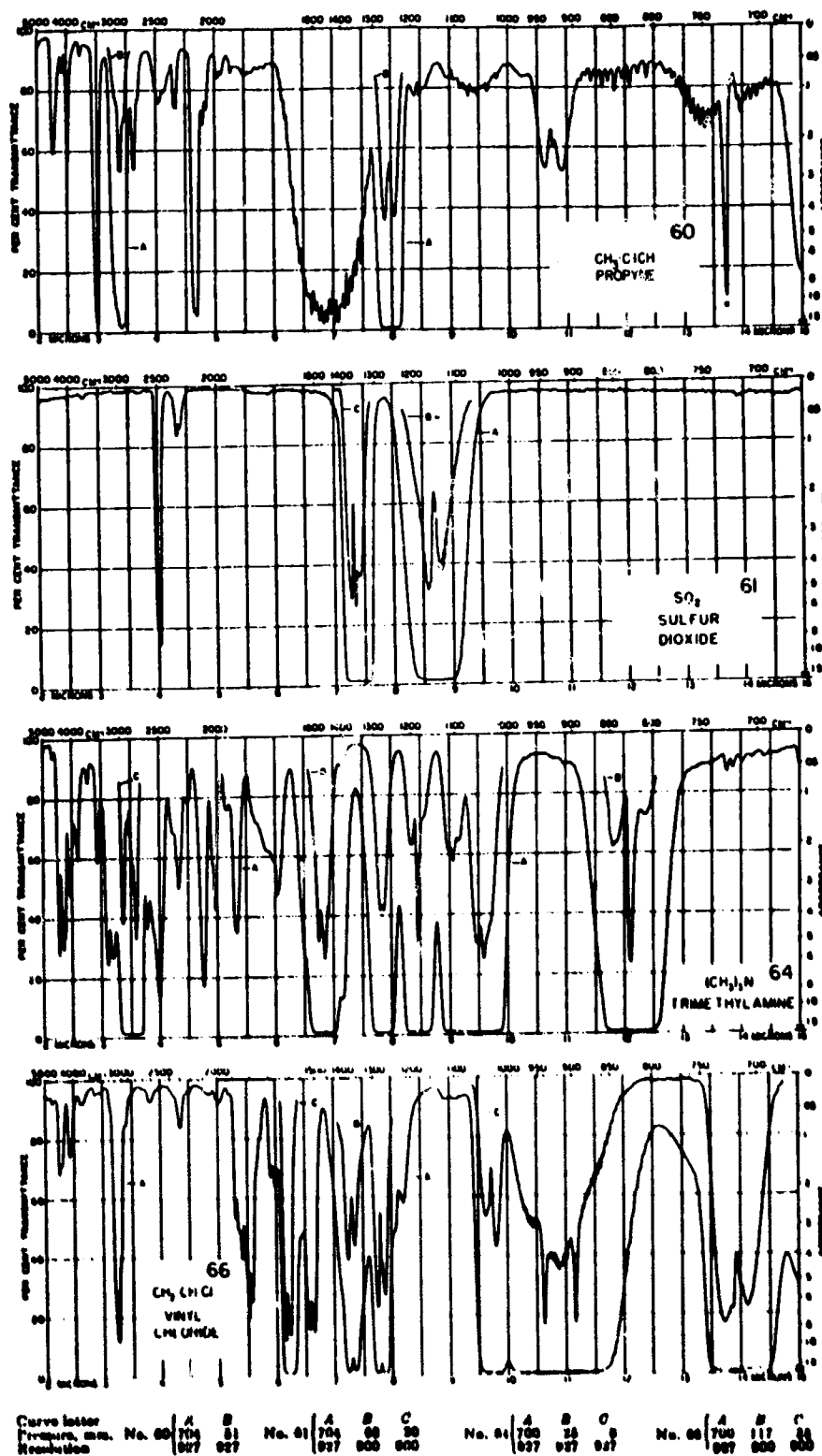


Figure 7. Spectral Absorbance of Propyne, Sulfur Dioxide, Trimethylamine, and Vinyl Chloride

Table 2. Hazardous Properties of Various Gases

Gas	Toxicity	Fire Hazard	Explosive Hazard
Acetylene	Slight-Moderate	Dangerous	Moderate
Allene	Unknown	Dangerous	Moderate
Ammonia	Severe	Moderate	Moderate
1.3 Butadiene	Moderate	Dangerous	Moderate
n-Butane	Slight-Moderate	Dangerous	Moderate
Carbon Dioxide	Slight	Non Flammable	-
Carbon Monoxide	Severe	Dangerous	Severe
Cyanogen	Severe	-	-
Cyclopropane	Moderate	Dangerous	Moderate
Diazomethane	Moderate	-	Severe
Dimethylamine	Moderate	Dangerous	Moderate
Dimethyl Ether	Moderate	Highly Dangerous	Moderate
Ethane	Slight-Moderate	Dangerous	Moderate
Ethylene	Slight-Moderate	Dangerous	Moderate
Isobutane	Slight	Dangerous	Severe
Methane	Slight	Dangerous	Dangerous
Methyl Chloride	Severe	Dangerous	Moderate
Methyl Mercaptan	Moderate	Dangerous	-
Monoethylamine	Unknown	Unknown	-
Monomethylamine	Severe	Dangerous	Moderate
Nitric Oxide	Severe	Unknown	-
Nitrous Oxide	Slight-Moderate	Moderate	Moderate
Propane	Slight	Highly Dangerous	Severe
Propylene	Slight-Moderate	Dangerous	Moderate
Propyne	Slight-Moderate	Dangerous	Moderate
Sulfur Dioxide	Severe	Non Flammable	-
Trimethylamine	Moderate	Moderate	Moderate
Vinyl Chloride	Severe	Dangerous	Severe

description concerning specific examples of some mass transfer cooling processes can be found in Reference [8]. A method of particular interest in this investigation is that of transpiration cooling associated with the injection of coolant gas through a porous structure into the surrounding high temperature boundary layer. A very extensive (over 100 references) bibliography of studies relating to transpiration cooling has been compiled recently by Nealy [9] and will not be repeated here; instead the emphasis will be placed on the interaction of convection and radiation when the injected gas is capable of absorbing and emitting radiation.

The problem of convection-radiation interaction has been a subject of considerable study during the last decade. A summary of these studies dealing primarily with external type flow of gray gases without mass injection can be found in publications [1, 4, 10]. The Couette flow geometry has received considerable attention [11-13] primarily because it represents a simple model of boundary layer flow. The analytical studies [14-17] dealing with the radiation effects in boundary layer flow over a flat plate of an absorbing gas have been extended by Kennedy [18] to account for mass addition. The effect on the convection and radiation heat transfer by injection of an absorbing gas in two-dimensional and axisymmetric stagnation point regions has been reported by Macken and Hartnett [19]. Howe [20, 21] with a specific problem in mind studies the effect of foreign species on the convection-radiation for an axisymmetric stagnation region in the presence of a shock front; his results are applicable only to his specific case studied.

In the above references the gray gas assumption has been employed. Although physically questionable, the simplifications have been necessitated by the lack of spectral data for the absorption coefficients and the need to reduce the complexity of the conservation equations. The utility of this approach has been that the simplified solutions illustrated the effects of various parameters. Only very recently has the gray assumption been relaxed and a number of solutions reported [22-26]. In all of these studies the fluid was considered to be stagnant and use was made of the total band absorptance correlation for the gases [3]. The solutions reported in References [25, 26] were for linearized radiative transfer. Nongray analyses of radiant heat transfer for flow of high temperature air over a flat plate without mass injection [27] and over symmetric bodies with massive blowing [28, 29] have been reported.

To the authors' knowledge no pertinent experimental studies dealing with combined convection and radiation heat transfer with transpiration of an absorbing gas have been published. Some related experiments dealing with combined conduction and radiation through a stagnant plane layer of infrared radiation absorbing gas confined between two opaque walls have been carried out [30, 31]; and the analysis based on wide band total absorptance model have been substantiated.



### 3. ATTENUATION OF RADIATION BY NEAR-STAGNANT ABSORBING GAS

#### 3.1 Analysis

##### 3.1.1 Physical Model and Assumptions

The physical model together with its coordinate system is shown in Figure 8. An absorbing-emitting gas is injected steadily and uniformly downward through a heated porous plate. The hot gas is held adjacent to the plate by buoyancy forces aided by retaining sidewalls which are assumed not to participate in the radiant energy transfer. The plate dimensions are large compared to the layer thickness, so that the flow and heat transfer can be considered to be one-dimensional. The thin two-dimensional layer in which the gas escapes the sidewalls is neglected. This neglect is justifiable as long as the injection rates are small. Surrounding the system is a medium which is transparent to radiation of all wavelengths investigated here. A spectral radiation intensity originating from sources external to the system and incident on the gas layer is denoted by  $I_{e\omega}$ . Only binary mixtures composed of the injected and surrounding gases are considered. The mechanisms of diffusion are ordinary and thermal diffusion; pressure and body-force diffusion are neglected.

##### 3.1.2 Conservation Equations

In the steady state, conservation of mass is satisfied by a constant mass flux through the layer equal to the injected mass flux. The momentum conservation equation for the physical model is

$$m \frac{dv}{dy} = - \frac{dp}{dy} + g\beta\rho(T_{\infty} - T). \quad (3.1)$$

Conservation of species is expressed by

$$\frac{d}{dy} [mw_i + j_i] = 0 \quad (3.2)$$

where the diffusional mass flux of the  $i^{\text{th}}$  species is given by

$$j_i = - \rho D \left[ \frac{dw_i}{dy} + \frac{w_i(1-w_i)}{T} \frac{dT}{dy} \right]. \quad (3.3)$$

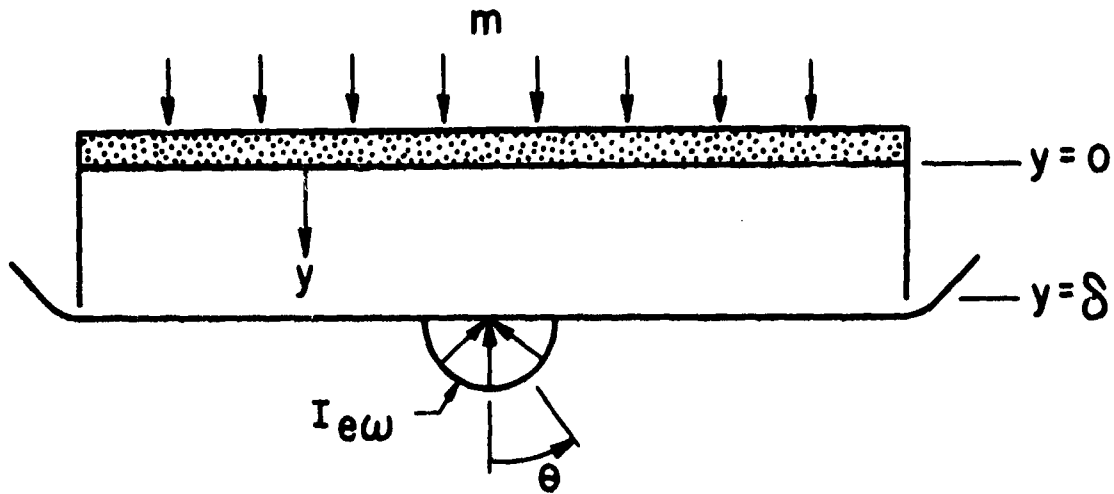


Figure 8. Physical Model and Coordinate System

The second term in the above equation represents the thermo-diffusion (T-D) effect [32]. The energy equation as applied to the system is expressed as

$$\frac{d}{dy} \left\{ \left[ mc_p + j_1 (c_{p1} - c_{p2}) \right] T + q \right\} = 0 \quad (3.4)$$

where the heat flux is given by

$$q = -k \frac{dT}{dy} + F + RT \left( \frac{M^2}{M_1 M_2} \right) \alpha j_1. \quad (3.5)$$

Included in the energy equation are the convection, inter-diffusion, conduction, radiant and diffusion-thermo (D-T) heat transfer mechanism terms.

Boundary conditions at the edge of the one-dimensional layer,  $\delta$ , are taken to be the same as those at the outer edge of the thin two-dimensional layer. Due to the diffusion and blowing, the gas temperature immediately adjacent to the plate may differ from the plate temperature [32, 33]. Hence the boundary conditions for the conservation equations are

$$\begin{aligned} y = 0; T = T_0 = T_r \\ y = \delta; \rho = \rho_\infty, T = T_\infty, w_1 = w_{1\infty}. \end{aligned} \quad (3.6)$$

Assuming that the porous plate is impermeable to the surrounding species provides the remaining required boundary condition.

The species (3.2) and energy (3.4) equations were integrated once to reduce the order of the equations. For the species equation, the resulting integration constant is derived from the impermeable plate condition and found to be the net injected mass flux,  $m$ . In the energy equation the integration constant is the energy flux,  $e_w$ , which is constant under steady state conditions. Defining dimensionless variables as the ratio of the actual variable to a reference value and collecting terms, the first integrals of the conservation relations take the following dimensionless forms,

$$\text{Momentum:} \quad \frac{d\rho^+}{d\xi} = \rho^{+2} \frac{d\rho^+}{d\xi} + \frac{Gr}{Re^2} \rho^+ (\theta - \theta_\infty) \quad (3.7)$$

$$\text{Species:} \quad w_1 = \frac{\rho^+ D^+}{Re Sc} \frac{dw_1}{d\xi} + \frac{\alpha w_1 (1 - w_1)}{\theta} \frac{d\theta}{d\xi} + 1 \quad (3.8)$$

$$\text{Energy:} \quad c_w^+ = \left[ c_p^+ + G \Delta c_p^+ + N M^+ G^+ \right] \theta - \frac{k^+}{Pe} \frac{d\theta}{d\xi} + Bo F^+ \quad (3.9)$$

with boundary conditions

$$\begin{aligned} \xi = 0; \quad \theta = \theta_0 = 1 \\ \xi = 1; \quad \rho^+ = 1, \theta = \theta_\infty, w_1 = w_{1\infty}. \end{aligned} \quad (3.10)$$

A parameter,  $N$ , is defined as

$$N \equiv Ra/c_p = RaT/c_p T \quad (3.11)$$

which in light of Eq. (3.5), represents the ratio of energy transport due to the diffusion-thermal effect to the energy transport by convection. Since diffusion-thermo is a low-order effect, this parameter becomes significant only when the convection and diffusion-thermo energy transport are of the same order of magnitude as in free convection.

To complete the system of equations, expressions for the radiation flux and an equation of state are required. In general, the properties are functions of the thermodynamic state. For simplicity, however, the necessary transport properties are considered to be only temperature dependent and are expressed by simple power law relations

$$k^+ = \theta^b, D^+ = \theta^c \quad (3.12)$$

where  $b$  and  $c$  are selected for each gas over the temperature range of interest.

### 3.1.3 Radiation Flux and Emergent Intensity

In the absence of scattering the spectral radiation flux is [1]

$$\begin{aligned}
F_{\omega}(\tau) = & 2\pi \int_0^1 I_{\ell\omega}(0, \mu) \exp(-\tau_{\omega}/\mu) \mu d\mu \\
& - 2\pi \int_0^1 I_{e\omega}(\mu) \exp\left[-(\tau_{0\omega} - \tau_{\omega})/\mu\right] \mu d\mu \\
& + 2 \int_0^{\tau_{0\omega}} \text{sign}(\tau_{\omega} - t) E_{\omega\omega}(\tau_{\omega}) E_2(|\tau_{\omega} - t_{\omega}|) dt_{\omega} \quad (3.13)
\end{aligned}$$

with the optical depth and thickness being defined by

$$\tau_{\omega} = \int_0^Y \kappa_{\omega} dy \quad \text{and} \quad \tau_{0\omega} = \int_0^{\delta} \kappa_{\omega} dy \quad (3.14)$$

respectively.

The intensity of radiation leaving the plate which is the sum of the emitted and reflected contributions is given by Eq. (2.2). In terms of new variables it can be written as

$$\begin{aligned}
I_{\ell\omega}(0, \mu) = & \epsilon_{\omega}(\mu) I_{b\omega}(T_p) + 2 \int_{-1}^0 \rho_{\omega}(\mu' + \mu) I_{e\omega}(\mu') \exp(\tau_{0\omega}/\mu') \mu' d\mu' \\
& - 2 \int_0^{\tau_{0\omega}} \left[ \int_{-1}^0 \rho_{\omega}(\mu' + \mu) \exp(t/\mu') d\mu' \right] I_{b\omega}(t) dt \quad (3.15)
\end{aligned}$$

where the terms represent the surface emission, the reflection of the energy incident on the layer after being attenuated by the layer and the reflection of the attenuated gaseous emission, respectively. Although Eq. (3.15) has been formulated in general, bidirectional reflectance data is very seldom available for engineering surfaces and the diffusely and specularly reflecting models are often resorted to. When the surface is a diffuse emitter and reflector,  $\epsilon_{\omega}(\mu) = \epsilon_{\omega}$  and  $\rho_{\omega}(\mu' + \mu) = \rho_{\omega}$ , the integration over direction in Eq. (3.15) can be readily performed to give the familiar exponential integral form [1]. For a specular reflection, the bidirectional reflectance is

$$\rho_{\omega}(\mu' + \mu) = \frac{\rho_{\omega}(\mu)}{2\mu'} \delta(\mu' - \mu)$$

where  $\rho_{\omega}(\mu)$  is the directional reflectivity and  $\delta(\mu' - \mu)$  the Dirac delta function. The intensity leaving the plate then becomes

$$\begin{aligned}
I_{\ell\omega}(0, \mu) = & \epsilon_{\omega}(\mu) I_{b\omega}(T_p) + \rho_{\omega}(\mu) I_{e\omega}(\mu) \exp(-\tau_{0\omega}/\mu) \\
& + \int_0^{\tau_{0\omega}} \rho_{\omega}(\mu) I_{b\omega}(t) \exp(-t/\mu) dt/\mu. \quad (3.16)
\end{aligned}$$

In order to obtain the total radiant heat flux, Eq. (3.13) has to be integrated over the spectrum. For this integration the total band absorptance

$$A(t) = \int_{\Delta\omega} [1 - \exp(-\kappa_{\omega} t)] d\omega \quad (3.17)$$

is introduced. A correlation for  $A(t)$  based on an exponential representation of the mean line intensity and the statistical band model have been developed [34, 35] for the vibrational-rotational bands of several gases. As pointed out in the introduction, several researchers have used this model and have found it to be quite adequate for energy transfer predictions.

To facilitate the use of the total band absorptance an approximation for the exponential integral function of the form,

$$E_2(t) \approx \sum_{i=1}^n a_i \exp(-b_i t) \quad (3.18)$$

which represents an approximation to the angular distribution of the intensity is employed. Equation (3.18) is a generalization of the exponential kernel approximation [35] which can be shown to be equivalent to the Milne-Eddington approximation [37]. However, retaining additional terms is equivalent to fourth and higher order spherical harmonics expansion of the intensity. For this study a two-term approximation with coefficients derived by Murty [37] was used to achieve an improved accuracy.

Substitution of the exponential integral approximation and the total band absorptance into Eq. (3.13), and a subsequent integration over the spectrum leads to an expression for the total radiant flux

$$\begin{aligned} F^+(y) = & \frac{2}{\sigma T_r^2} \sum_{\text{bands}} \left\{ \pi \int_0^1 I_{\ell c}(0, \mu) [\Delta\omega - A(y/\mu)] \mu d\mu \right. \\ & - \pi \int_0^1 I_{cc}(\mu) \left[ \Delta\omega - A\left(\frac{\delta - y}{\mu}\right) \right] \mu d\mu \\ & \left. + \int_0^{\delta} \text{sign}(y - z) E_{bc}(z) \sum_i a_i A'(b_i |y - z|) dz \right\}. \end{aligned} \quad (3.19)$$

Equation (3.19) was obtained assuming that the absorption bands are narrow enough that the Planck function could be considered constant over the entire band width. Similarly, an expression for the intensity emerging from the layer within a given spectral band is

$$I_{\ell c}(\delta, \mu) = I_{\ell c}(0, \mu) [\Delta\omega - A(\delta/\mu)] + \int_0^{\delta} I_{bc}(z) \sum_i a_i A'(b_i |(\delta - z)/\mu|) dz \quad (3.20)$$

### 3.1.4 Method of Solution

When coupled to radiation transfer the governing equations represent a system of two-point, nonlinear, integro-differential equations for which a closed-form solution is not possible and numerical methods must be resorted to. Numerically, coupled integral equations are simpler to solve than coupled integro-differential equations. An integration of the non-dimensional conservation relations reduces them to a system of integral equations

$$\rho^+(\chi) = 1 + \int_0^\chi \rho^{+2} \left[ \frac{d\rho^+}{d\chi} + \frac{Gr}{Re^2} (\theta_\infty - \theta) \right] d\chi \quad (3.21)$$

$$w_1(\chi) = w_{1\infty} + \int_0^\chi \left[ \frac{ReSc}{\rho^+ D^+} (1 - w_1) - \frac{\alpha w_1 (1 - w_1)}{\theta} \frac{d\theta}{d\chi} \right] d\chi \quad (3.22)$$

$$\theta(\chi) = \theta_\infty + \int_0^\chi \frac{Pe}{k^+} \left[ q_t^+ - Bo F^+ + \left( c_p^+ + j^+ \Delta c_p^+ + NM^+ j^+ \right) \theta \right] d\chi \quad (3.23)$$

where  $\chi = 1 - \xi$ . The numerical solution was accomplished by successive approximations with a weighted averaging of the previous solutions. It was found that in the first approximations the weighting of the current approximation should be small to assure reasonably rapid convergence.

## 3.2 Experiments

### 3.2.1 Description of Experimental Facility

The test apparatus was installed in a fume hood in order to guarantee a sufficient degree of environmental control. A fan drew air into the hood from below the chamber and exhausted it through a duct into the atmosphere. A slightly reduced pressure in the fume hood prevented the transpired gases from endangering the personnel and also provided a means of controlling the flow field of the injected gas. The test apparatus consisted of the traversing mechanism, support stand, and test section. A photograph of the test apparatus is shown in Fig. 9.

The traversing mechanism was designed and constructed by Research Services Inc., St. Paul, Minn. The radiation detector was mounted on a yoke shaped scanning mechanism permitting the positioning of the detector at various polar angles. The arms of the yoke were adjustable such that the distance between the radiation detector and the axis of rotation could be varied from 4" to 24" at spacing intervals of one inch. The detector holder could be displaced along the yoke (6" to the left of the center line and 6" to the right). An angle indicator provided with locking pins served for variation of polar angles (from the vertical) in 5° increments. The rotating component of the scanning mechanism was mounted on a frame which could be moved longitudinally by about 12" sliding on rectangular rods. Besides serving for the positioning of the detector the

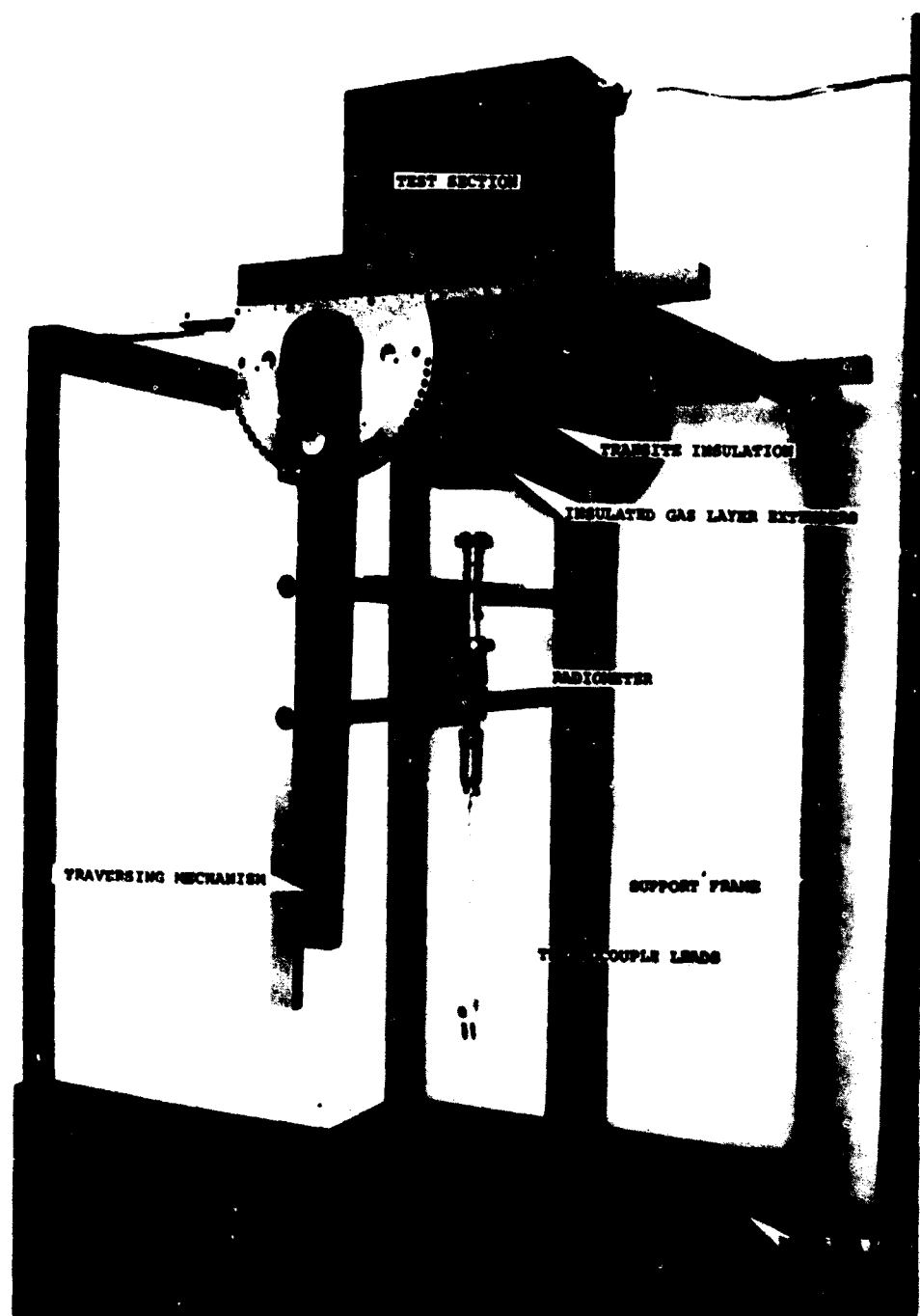


Figure 9. Photograph of Test Apparatus with Radiometer Mounted Below the Test Section

traversing mechanism was also utilized for the support of the aspirating-temperature probe. The test section was installed in the traversing mechanism such that its axis of rotation always remained in the surface of the porous plate, and the longitudinal and lateral motions were always parallel to the plate surface.

### 3.2.2 Test Assembly

The heated porous plate was housed in a 12" x 9" x 4" sheet metal box open at one end. Welded to the chamber were angle irons which served to attach it to the support frame. The test section consisted of a gas plenum chamber closed on one side by the porous plate, copper electrodes, transite insulating material, and sheet-metal gas layer extenders. The test section is shown in Fig. 10.

A porous plate with large internal surface area and uniform porosity is desired for effective heat transfer and flow distribution. A survey of available materials revealed that a nickel-base permeable alloy sheet, called Poroloy, produced by the Bendix Filter Division of the Bendix Corporation, was appropriate. The Poroloy sheet was composed of a nickel base with 22% chromium, 18.5% iron, 9% molybdenum, 1.5% cobalt, 6% tungsten, and small percentages of carbon, manganese, silicon, phosphorus, and sulfur. This alloy is oxidation resistant up to 2100°F and has a relatively high strength above 1500°F. The Poroloy plates were made from a 0.005 inch diameter wire, flattened to a ribbon, wound into a laminated structure at a nominal 30 degree wind angle (60 degree crossover angle), and sintered.

Two 6" x 12" sheets of different permeabilities were acquired. One sheet has a permeability of  $2.0 \times 10^{-9}$  ft and the other with a permeability of  $2.0 \times 10^{-8}$  ft was ten times more porous than the first. The permeability of the individual sheets was tested by the manufacturer to conform to within  $\pm 10\%$  of the level specified when subjected to a pressure difference of 10.0 psi with exit pressure equal to 14.7 psia and air temperature of 70°F.

Due to the alloy's relatively low electrical resistance (approximately  $6.9 \times 10^{-3}$  ohm at 70°F for a 2.2" x 3.5" x .025" sheet), a current of 150 to 250 amperes supplied by a DC arc welder was needed to reach the desired plate temperature. In order to minimize heat conduction losses from the plate and still maintain structural strength, transite pieces were placed in the box.

The upstream part of the sheet-metal box consisted of a plenum chamber. A gas line from a battery of supply bottles and various measuring and regulation devices were connected to the top of the plenum with the gas flowing into the chamber



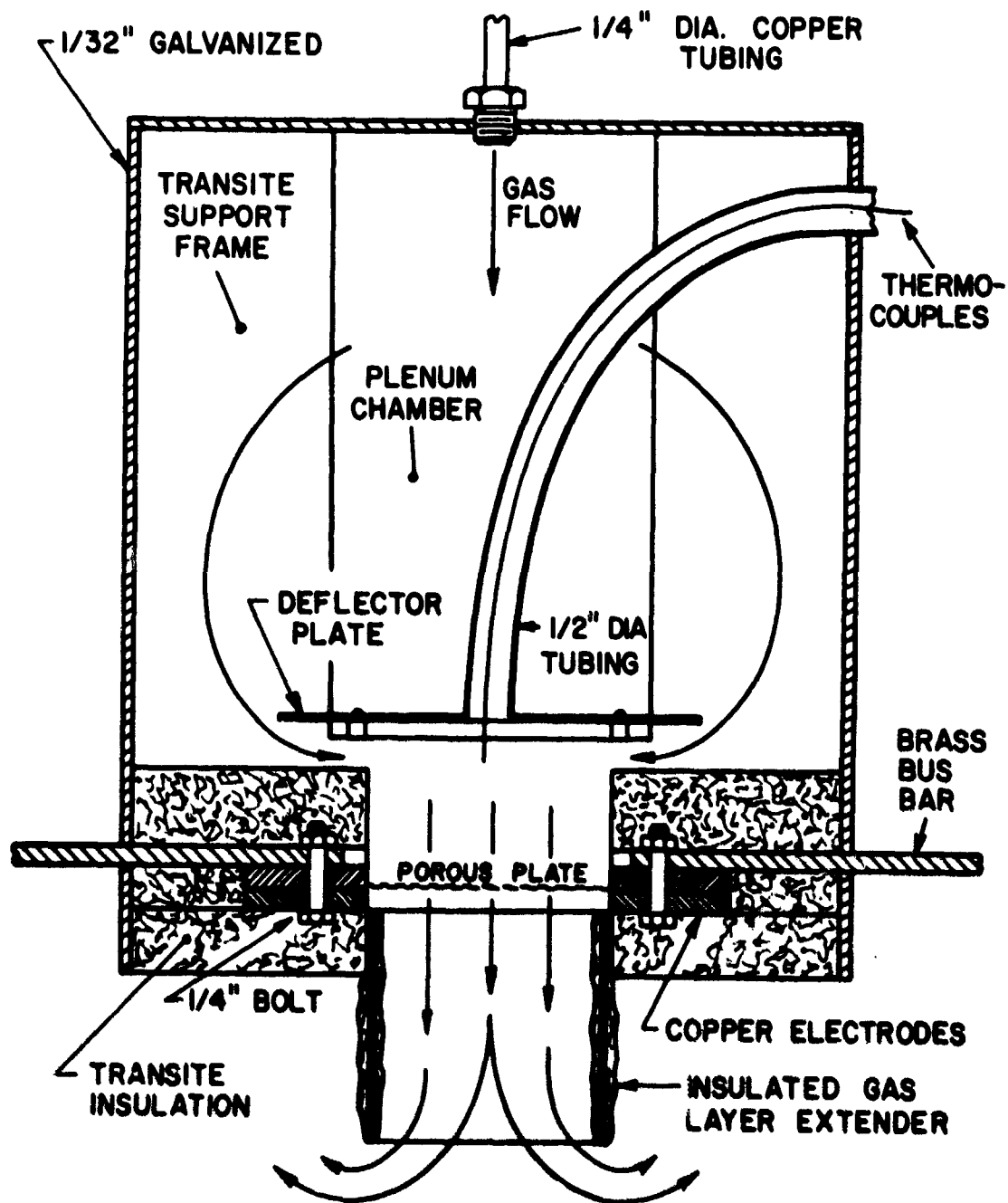


Figure 10. Sectional View of Test Assembly

and out through the porous plate. A deflector plate was mounted between the porous plate and the gas inlet in order to guarantee uniform gas flow through the plate and to shield the plenum from radiant heating. Attached to the deflector plate was a flexible steel conduit which served as an instrumentation port, allowing surface and gas temperature measurements inside the plenum.

Sheet metal guards of varying length could be mounted below the plate to serve as gas layer extenders. The gas layer extenders were thermally insulated on both sides with asbestos material in order to minimize heat conduction losses. The direction of the gas flow was downward until it reached the exit plane of the extenders where buoyancy reversed its flow direction.

### 3.2.3 Instrumentation and Calibration

In order to predict the radiation emitted by the plate its surface temperature and the local variation as well as the emittance have to be known. A Leeds and Northrup surface temperature probe ("Surtemp") was used to measure the temperature distribution. Its specifications were:

Accuracy: Ambient to 530°F:  $\pm 3^\circ\text{F}$ ; 530° to 1200°F:

$\pm (3/8\% \text{ of reading} + 1^\circ)\text{F}.$

The "Surtemp" probe had an absolute error of 5°F at 1000°F. Since the probe had to be operated manually (i.e., it had to be held in position touching the lower surface of the plate) and could not be used while radiation measurements were being taken, chromel-alumel surface thermocouples were employed during certain phases of the experiments.

Previous experience accumulated by research personnel at the Allison Division of the General Motors Corporation was utilized for the design and construction of an aspirating gas temperature probe for the measurement of gas layer temperature. The probe consisted of Inconel tubing with an insulated 0.02" O.D. Inconel tube containing the thermocouple wires, see Fig. 11. The thermocouple wires were of 36 gage (0.003"D) chromel-alumel. A tee with two air-line connections was positioned at the base of the tubing with one opening smaller than the other. As air was blown into the small opening and out of the large opening, the resulting jet lowered the pressure of the tube below atmospheric pressure causing the surrounding gas to be drawn into the probe through a 5/64" D hole in the tip. The tip was normal to the flow so that the hole faced in the flow direction. The thermocouple junction was made by a small bead weld (0.010"D) and was shielded by a Monel tube.

The transpiring gas flow was measured with a Fisher-Porter Rotameter which was calibrated against a standard integrated

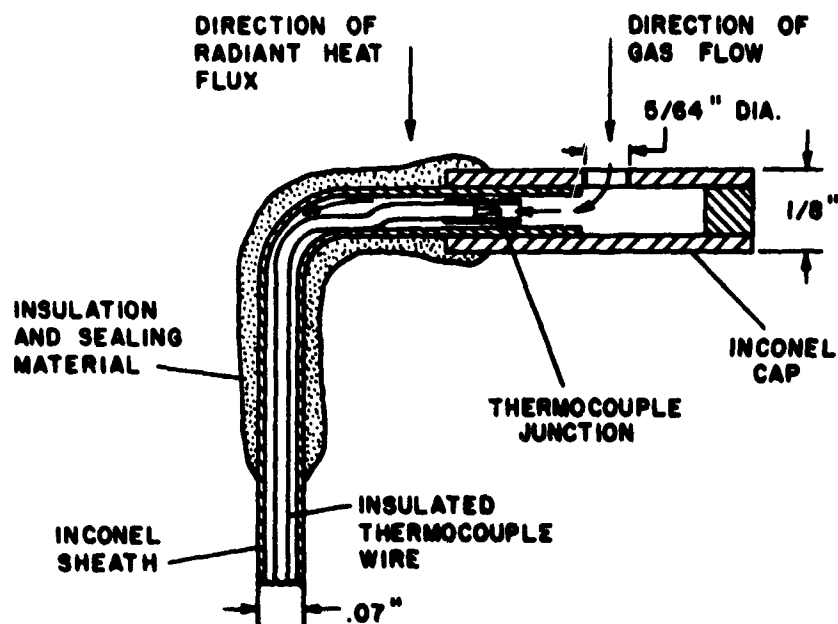


Figure 11. Sectional View of Gas Temperature Probe Tip

gas flow meter manufactured by American Meter Company. The two flow meters were mounted next to each other and connected in such a way that the flow through the rotameter could be directed through the integrating flow meter. Once the rotameter was calibrated, the integrating flow meter was by-passed to avoid an unnecessary pressure drop.

Power dissipation was determined from the product of the input voltage and current. The voltage drop across the test section was measured with a standard voltmeter. Electric current was determined by measuring the voltage drop across a shunt resistance of 125  $\mu$  ohms.

The radiant energy emerging from the gas layer was measured with an infrared radiometer which consisted of a wide-band-pass filter, a potassium-bromide lens, two diaphragms, and a detector, (see Fig. 12). The detector, a thermopile, was manufactured by Charles M. Reeder Company of Detroit, Michigan. The filter and 1/4" D diaphragm were mounted in front of the thermopile. A second 3/8" D diaphragm was positioned in front of the lens and both were held in a 1/2" D tube. The thermopile was then inserted into the tube behind the lens. The assembled radiometer was mounted and adjusted on the traversing mechanism so that any desired surface element of the plate could be brought into focus.

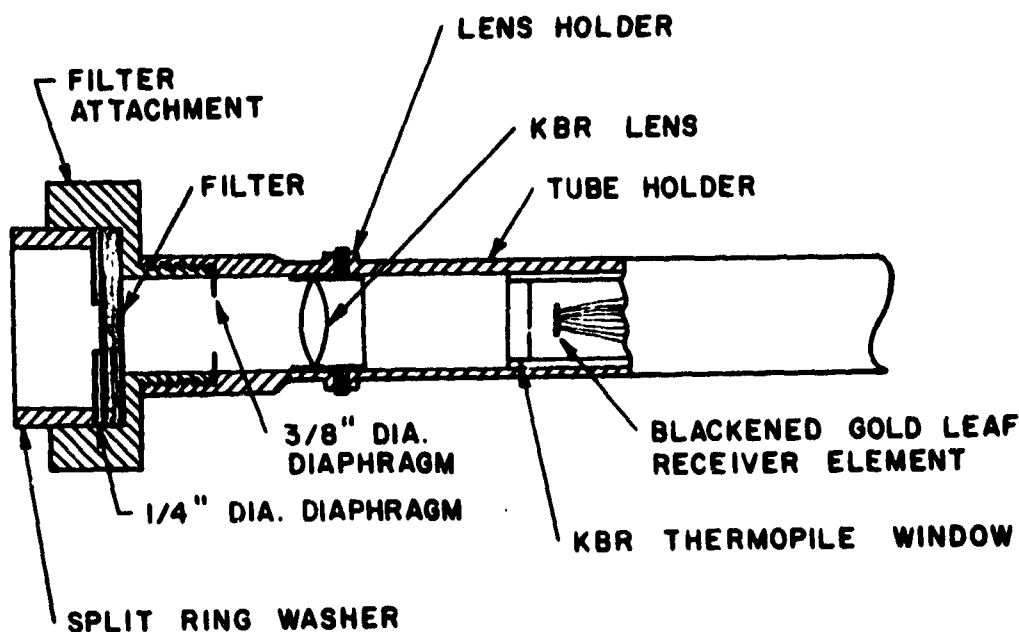


Figure 12. Sectional View of Radiometer

In order to measure the attenuation in a particular wavelength band a filter was used. For example, the filter employed for the  $4.3\mu$  (fundamental band of  $\text{CO}_2$ ) had a band center at  $4.35\mu$  and a half band width of  $0.43\mu$ . A transmittance curve is shown in Fig. 13. The filter, 0.040" thick, was manufactured by the Optical Coating Laboratory, Santa Rosa, California.

In order to investigate the attenuation due solely to the presence of participating gas, the emerging radiant energy was compared with that measured with a transparent gas (air) present. Thus the effect of transpiration cooling on the emitted radiation was practically eliminated. The measured normalized emergent band intensity was expressed as

$$I_{\text{exp}}^*(\delta, \theta) = \int_{\Delta\lambda_i} t_{\lambda} I_{\lambda}(\delta, \theta) d\lambda / \int_{\Delta\lambda_i} t_{\lambda} I_{\lambda}(0, \theta) d\lambda \quad (3.24)$$

This definition is analogous to that of Eq. (2.5), except that the spectral transmittance of the optical system  $t_{\lambda}$  (wide band pass filter together with the KBr lens and thermopile window, see Fig. 12) has been incorporated.

### 3.2.4 Calibration and Test Procedure

In order to determine the effective responsivity of the radiometer, it was necessary to evaluate the total transmittance

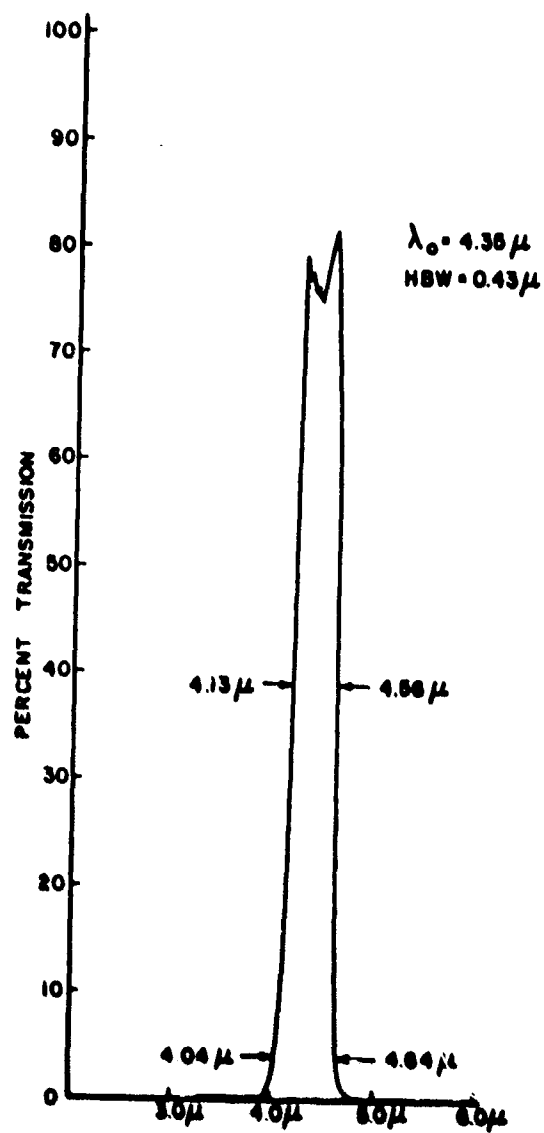


Figure 13. Spectral Transmittance Curve of 4.35 $\mu$  Wide Band Pass Filter

of the filter, the focal length of the lens, and the total and wavelength band responsivity of the thermopile. The fraction of the total radiant energy coming from a black body subtended by a small solid angle and passing through a filter is given by

$$t_F = \int_0^{\infty} t_{F\lambda} I_{b\lambda}(T) d\lambda / (\sigma T^4 / \pi) \quad (3.25)$$

The results were computed and found to be 0.0573 for  $T = 1000^\circ\text{F}$ , 0.0560 for  $T = 1250^\circ\text{F}$ , and 0.0514 for  $T = 1500^\circ\text{F}$ . The focal length of the lens was determined by two different methods [38]; both methods lead to a focal length of 0.866.

In order to determine the responsivity of the thermopile, a calibration curve was experimentally established. Since each thermopile had different characteristics it is important that this measurement be done with extreme care for each thermopile. The detector was irradiated with a calibrated standard black body source (Infrared Industries Model No. 406) as recommended by Nicodemus [39]. The output signal of the thermopile was recorded as a function of incident radiant energy. The black body temperature was controlled with a calibrated temperature controller. The control range extended from  $50^\circ\text{C}$  to  $1000^\circ\text{C}$  with a specified accuracy of  $\pm 1^\circ\text{C}$ .

In essence two types of calibration curves were determined for the radiometer. The first type pertains to the thermopile alone on a total energy basis and the second to the thermopile together with the filter on a band basis. Both types of calibration curves were established for source temperatures of  $1000^\circ\text{F}$ ,  $1250^\circ\text{F}$ ,  $1500^\circ\text{F}$ . One of these curves is illustrated in Fig. 14 and shows that the responsivity of the thermopile on a total energy basis is linear.

To determine the effective transmittance of the radiometer without a filter the lens and its tubular retainer were mounted at a fixed distance,  $s$ , from the blackbody source. The image plane of the lens was located by adjusting the distance between the thermopile and lens for the maximum thermopile output. From the black body temperature, geometry and thermopile calibration, the effective transmittance could be calculated. Transmittances as a function of the two independent geometric variables, object distance,  $s$ , and black body source diameter (the remainder of the geometry is given by the thin lens formulas) were obtained.

Voltage signals from the thermocouples and thermopile were connected by chromel-alumel couplings and leads to an ice bath reference junction. The signal was recorded through a 10 channel switching mechanism on either a Leeds and Northrup type K-3 potentiometer or a Honeywell Visicorder data acquisition system.

After the equipment was properly arranged and aligned, the arc welder was ignited and the current adjusted to the desired

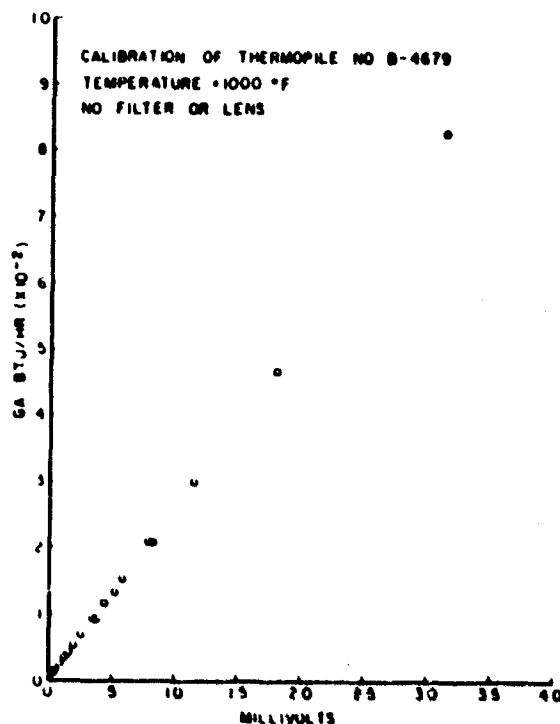


Figure 14. Thermopile Calibration Curve

level. The plate was allowed to reach the steady state, which required between one and one half to two hours of time. Subsequently, the gas flow was started and adjusted to the desired rate and the fan damper on the fume hood set. Final adjustments were made in the current level to reach the required temperature of the plate.

After the system reached steady state conditions the voltages of the thermocouples mounted on the plate surface were monitored and recorded. Simultaneously the plate surface temperature distribution was measured with the "Surtemp" probe. The temperature of the gas, its flow rate, and test section pressure were also recorded. The gas temperature probe was positioned 1" below the gas layer extender while the air flow through the expansion valve was recorded. To verify the steady state the data were monitored with the Visicorder with the final data being obtained with the K-3 potentiometer.

Radiation measurements were also made under steady state conditions. Since the temperature distribution of the plate changed with flow rate, it became necessary to compare the emerging radiation of an essentially transparent gas (air) to that of an absorbing-emitting gas under otherwise identical conditions. The injected air flow rate was set and the temperature distribution of the plate measured with the "Surtemp"-probe. Once radiation data were obtained with air as the working fluid, it was replaced by a radiation participating gas under corresponding conditions.

The signal from the radiometer was strong enough so that it could be read with a potentiometer without further amplification. During testing it was found that the temperature of the thermopile casing rose. In order to compensate for the drift of the thermopile output, a metal plate of uniform temperature was placed between the source and the radiometer and the output of the thermopile measured. The plate was subsequently removed and the signal corresponding to the radiation received by the thermopile was measured as quickly as possible. Subsequently the metal shield was returned to the radiation path in order to keep the radiometer at room temperature.

### 3.3 Results and Discussion

#### 3.3.1 Analytical Results

Since the independent parameters are numerous, a review of them seems appropriate. They are the Re, Gr, Sc, Pe, N, and Bo numbers, the gas temperature next to the plate, the radiation characteristics of the plate, the gas absorption properties, the incident radiation, and the optical or layer thickness. Results are presented for the diffusely emitting and reflecting surface in the absence of external radiation in order to reduce the number of parameters. Carbon dioxide, methane, and sulfur dioxide were selected for the computations because of their strong fundamental bands in the near infrared.

The results are presented in terms of a normalized emergent band intensity defined by, see Eqs. (2.4) and (2.5),

$$I^* = \int_{\Delta\omega} I_{\omega}(\delta, \nu) d\omega / \int_{\Delta\omega} I_{\omega t}(0, \nu) d\omega \quad (3.26)$$

where  $I_{\omega t}(0, \nu)$  is the intensity leaving the plate in the absence of an absorbing gas layer. The normalized band intensity  $I^*$  serves as a measure of the attenuation. A certain amount of ambiguity is associated with an effective band width for an exponential type band model. At high pressure, the exponential wide-band model is [34]

$$\kappa_{\omega}(T) = \rho C_0^2 \exp(-|\omega - \omega_c|/\Lambda_0) \quad (3.27)$$



where  $A_0$  is a bandwidth parameter which depends directly on temperature and  $C_0^2$  is the line intensity to spacing ratio which varies inversely with temperature for typical gas bands.  $A_0$ , the band half-width could be used as a representative bandwidth, but would be too narrow to be meaningful. From Eq. (3.27) an effective bandwidth may be defined as

$$\Delta\omega = 2A_0 \ln \left[ \kappa(\omega_{c0})/\kappa(\omega_c) \right] \quad (3.28)$$

where  $\omega_{c0}$  is the band cut-off wave number. The band cut-off to band center absorption coefficient ratio  $\kappa(\omega_{c0})/\kappa(\omega_c)$  was taken as 0.001 in order to remain consistent with the carbon monoxide effective bandwidth presented by Tien [3].

The effect which the blowing rate has on the temperature and concentration profiles is shown in Figs. 15 and 16. A measure of the T-D and D-T effects and the effect of coupled radiative transfer can be obtained from a comparison with an analysis neglecting these effects. From the concentration profile, it is seen that the T-D and D-T effects are quite weak and might well be neglected. The coupling of the radiative transfer is also quite small because of the low partial pressures of the absorbing gas and the fact that only about 3% of the radiant energy emitted by the plate lies within the absorbing bands. It is of interest to note that even with the weak coupling, the trends in the temperature profiles are the same as those for stronger coupling. Both the temperature and concentration increase with increasing blowing rate. Since the concentration is increasing, the gas layer is becoming more opaque within the absorption bands and the energy leaving the plate is more effectively attenuated. The net effect is one of reducing the emergent intensity as shown in Fig. 17.

A second effect is due to the variation of the total band absorptance parameters. Neglecting the pressure broadening, the total band absorptance is a function only of the integrated band intensity and bandwidth. For carbon-dioxide, the bandwidth variation is about the same for both bands, while the integrated band intensity is one order of magnitude higher for the fundamental  $4.3\mu$  band. The trends of the  $15\mu$  band which is a relatively broad band are primarily dependent on the bandwidth, whereas the  $4.3\mu$  band is primarily dependent on the integrated band intensity. Both parameters determine the attenuation of radiation by the gas layer, but from the results in Fig. 17 the integrated band intensity is the more dominant. This effect was also observed in calculations in which the gas temperature next to the plate was varied while the plate temperature was maintained constant.

The attenuation as a function of the plate emittance with polar angle and bandcenter wavelength as parameters is presented in Fig. 18. Although the temperature and concentration distributions are not shown, they were computed and found to vary only

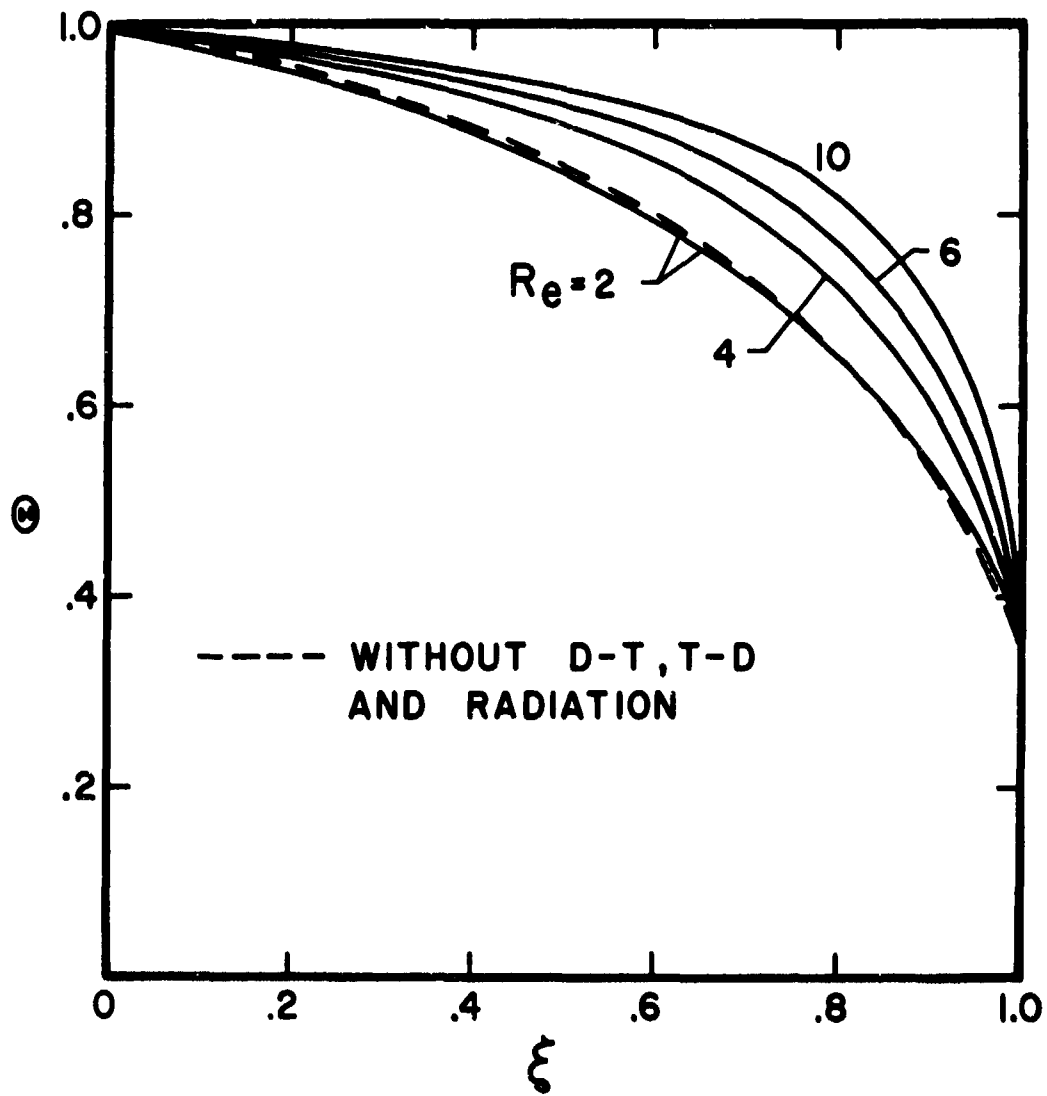


Figure 15. Effect of Injection Rate on the Temperature Distribution;  $\text{CO}_2$ ,  $\delta = 6\text{cm}$ ,  $T_p = 836^\circ\text{K}$ ,  $\epsilon = 0.6$

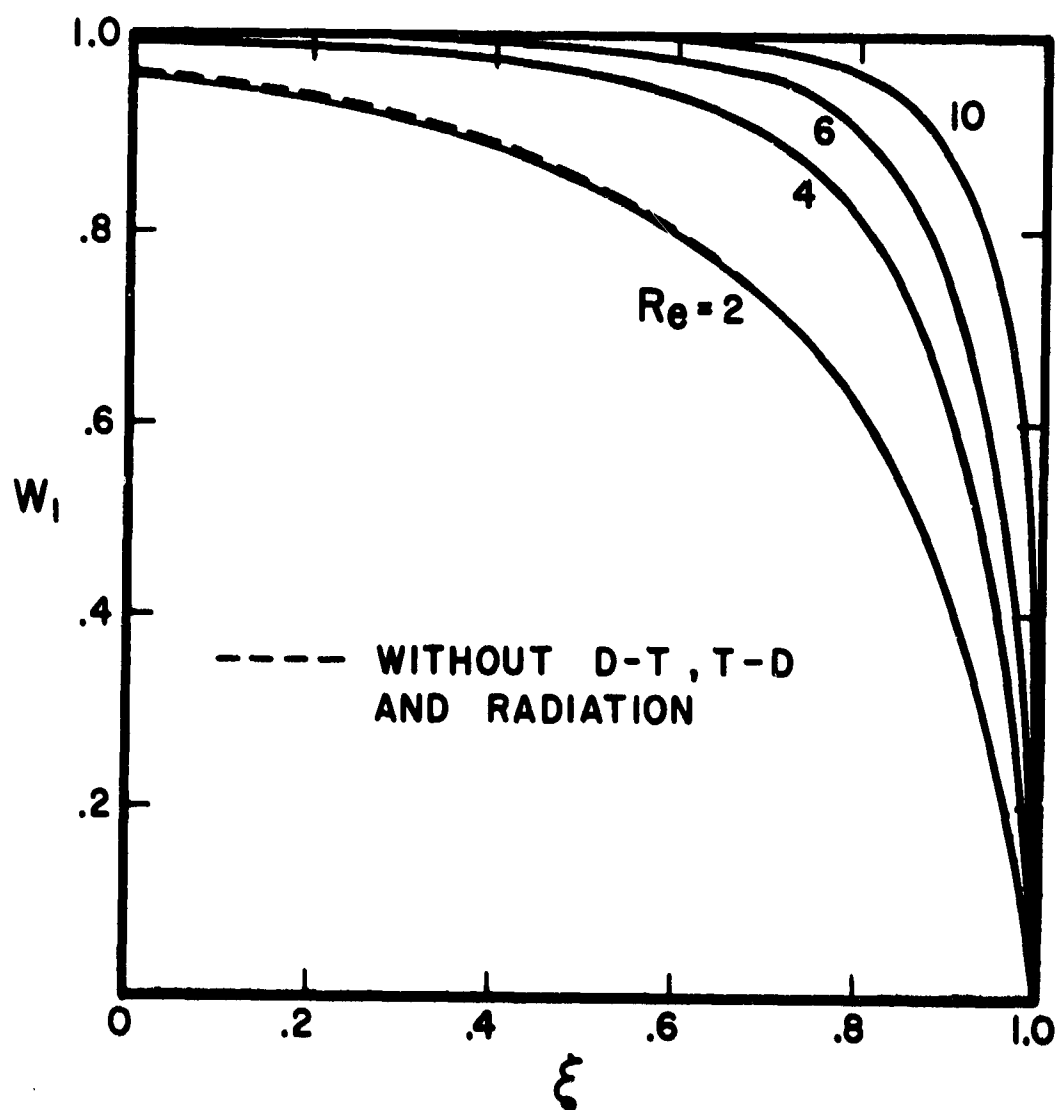


Figure 16. Effect of Injection Rate on the Mass Fraction Distribution;  $CO_2$ ,  $\delta = 6\text{cm}$ ,  $T_p = 836^\circ\text{K}$ ,  $\epsilon = 0.6$

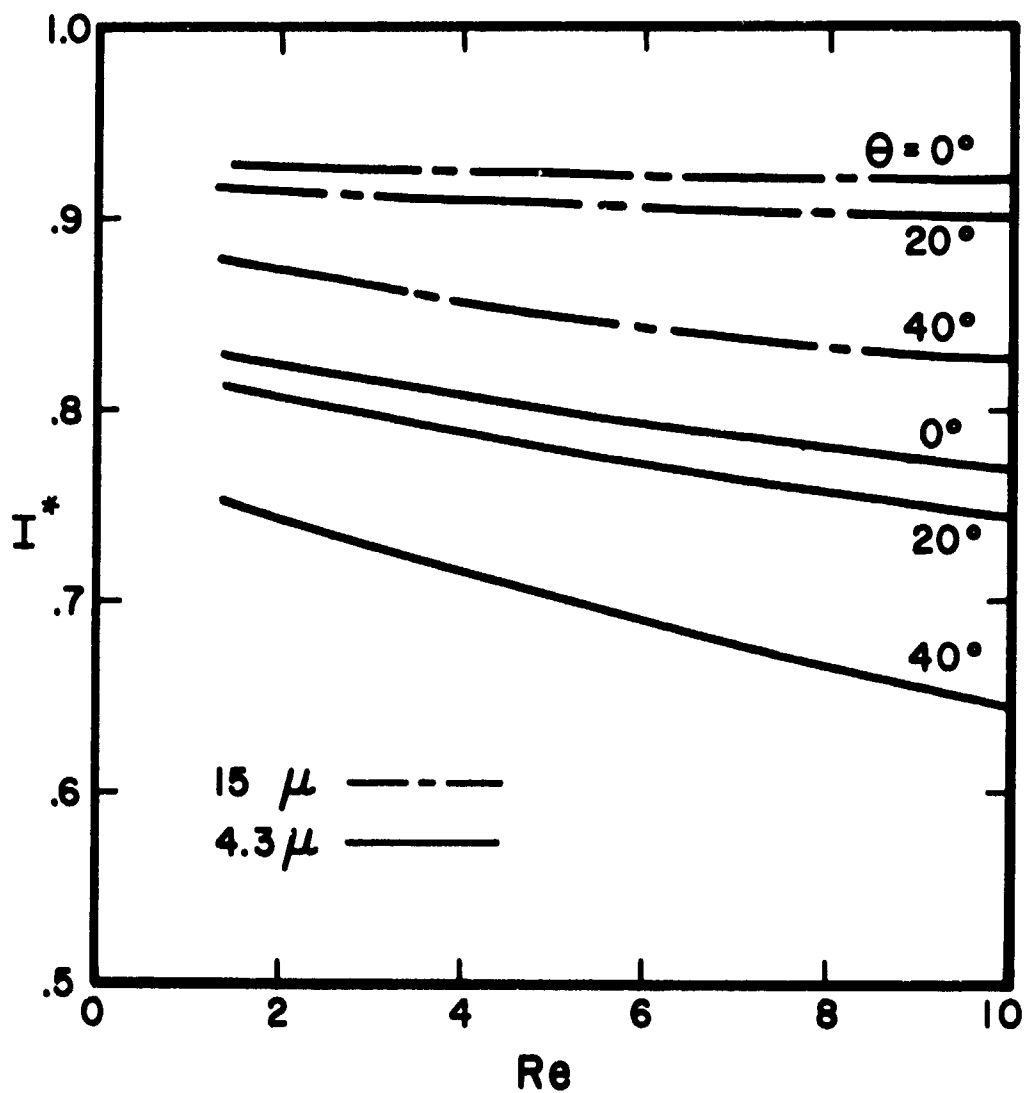


Figure 17. Effect of Injection Rate on the Normalized Emergent Band Intensity;  $\text{CO}_2$ ,  $\delta = 6\text{cm}$ ,  $T_0 = T_p = 836^\circ\text{K}$ ,  $\epsilon = 0.6$

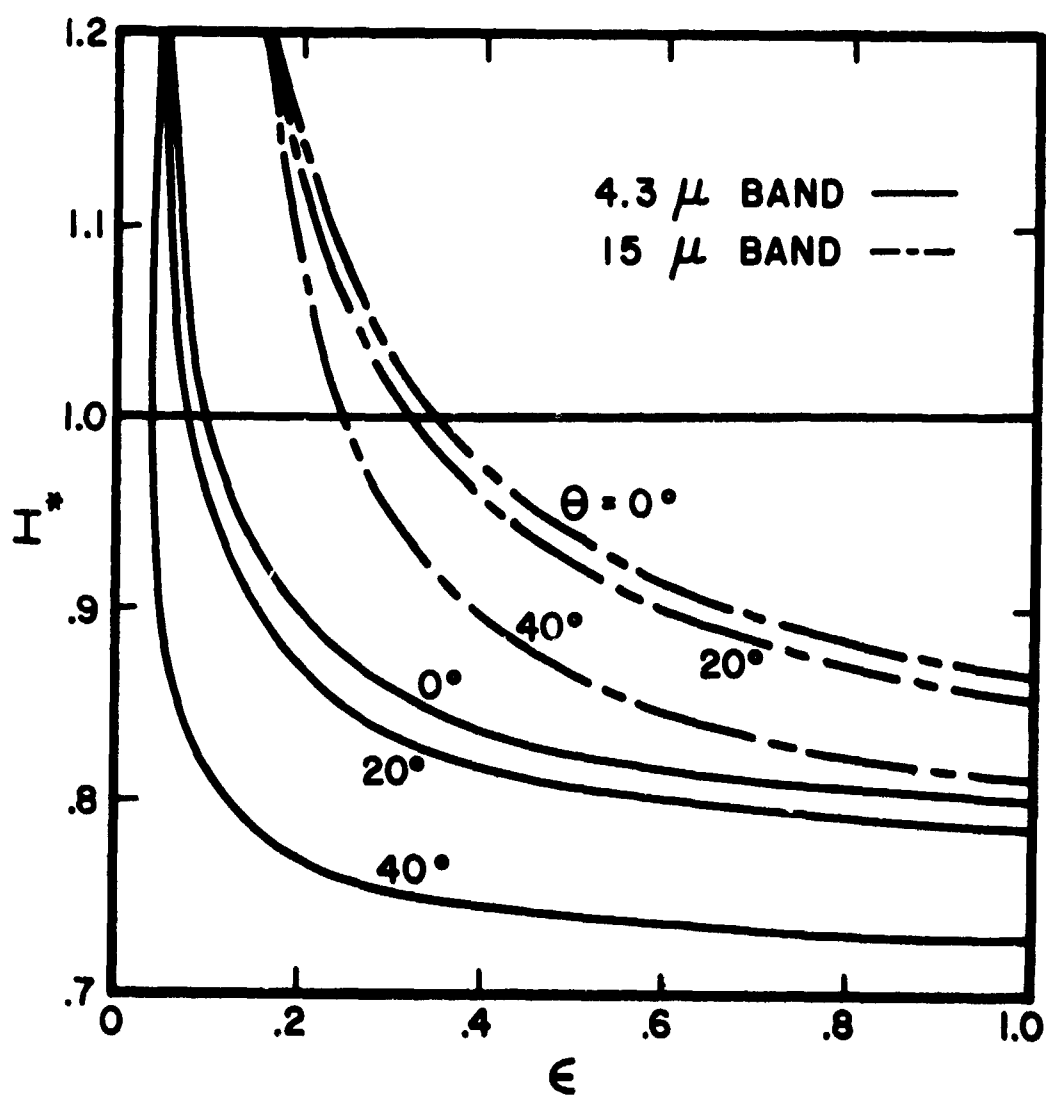


Figure 18. Effect of the Plate Emittance on the Normalized Emergent Band Intensity;  $\text{CO}_2$ ,  $\text{Re} = 2$ ,  $\delta = 2\text{cm}$ ,  $T_0 = T_p = 836^\circ\text{K}$

slightly with plate emittance. Inspection of Fig. 18 reveals that there is a plate emittance at which the actually emergent intensity in the presence of an absorbing gas equals that in presence of a non-absorbing gas. This behavior will be referred to as the "break-even emittance." As the plate emittance is decreased, the gas emission which emerges directly from the layer remains almost constant and the energy reflected by the plate increases. It follows that the emergent intensity of a surface with an absorbing gas present can exceed that in absence of an absorbing gas at low plate emittance values. An attenuation of the energy emitted from the plate takes place only when the emittance is greater than the "break-even emittance."

The dependence of the emergent intensity on the plate temperature and layer thickness is presented in Fig. 19. As expected, an increase of the layer thickness enhances the attenuation. Inspection of Fig. 19 reveals further that the attenuation is approaching a limit. In the  $4.3\mu$  band the results for a 12 cm. layer thickness were within one plotted linewidth of those for an 8 cm. layer. At this limit, the gas becomes opaque in the band center. Energy emitted by the plate continues to emerge from the layer through the band wings which do not become opaque as rapidly as the band center. The limit is thus the layer thickness at which the attenuation by the band center has reached an optimum and any further increases in the attenuation must be accomplished by the band wings.

In the near normal direction, the emergent intensity is almost isotropic since the path length does not change significantly. At oblique angles, the attenuation increases quite rapidly because of the increase in path length. Results were not obtained for  $\theta > 80^\circ$  because of the singularity in Eq. (3.22) as  $\mu = \cos\theta$  approaches zero. As  $\theta \rightarrow \pi/2$ ,  $I^* \rightarrow 0$  which is consistent with the results presented in Figs. 19 and 20.

To investigate the influence of the absorption properties of the injected gas, calculations using the absorption characteristics of methane [40] and sulfur dioxide [41], considering only their strongest absorption bands, were made. To make the results compatible with those obtained for carbon-dioxide, the Reynolds number was adjusted accordingly. The results for methane and sulfur dioxide with the layer thickness as a parameter are presented in Fig. 20. Since sulfur dioxide is the stronger absorber in the  $7.35\mu$  fundamental band than the  $4.3\mu$  fundamental  $\text{CO}_2$  band, the attenuation increases, especially for the smaller layer thicknesses. Hence,  $\text{SO}_2$  would be advantageous in physical systems with small boundary layers. The fundamental  $\text{SO}_2$  and  $\text{CH}_4$  bands are also wider than the fundamental  $\text{CO}_2$  bands and therefore cover a larger portion of the spectrum. Although  $\text{SO}_2$  is a stronger absorber and attenuates a larger portion of the spectrum, its fundamental band is remote from the maximum plate emission for the temperatures considered. The net amount of energy attenuated by the  $\text{SO}_2$  fundamental band is consequently

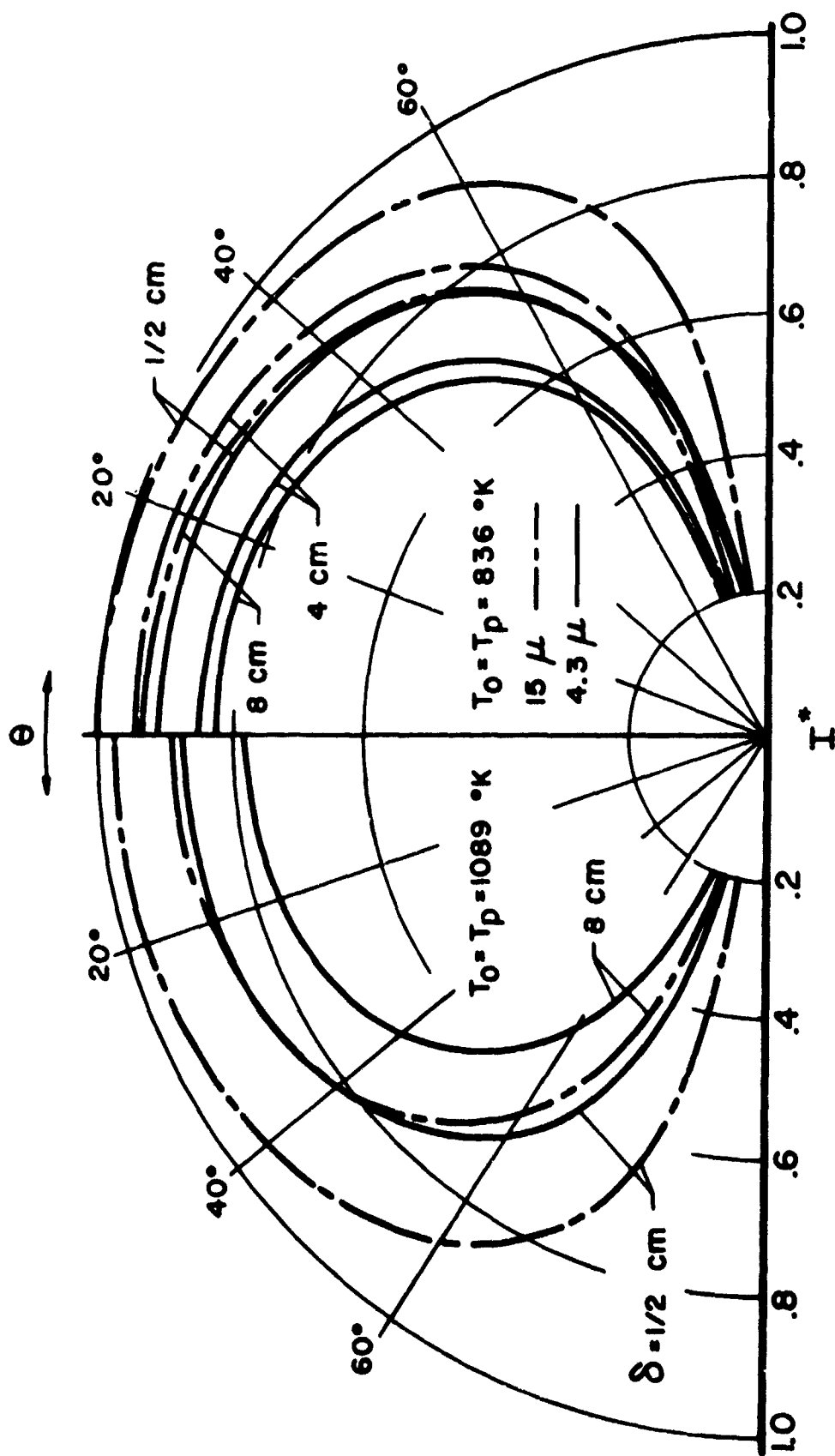


Figure 19. Dependence of Emergent Band Intensity on Layer Thickness;  $\text{CO}_2$ ,  $\text{Re} = 2$ ,  $\epsilon = 0.6$

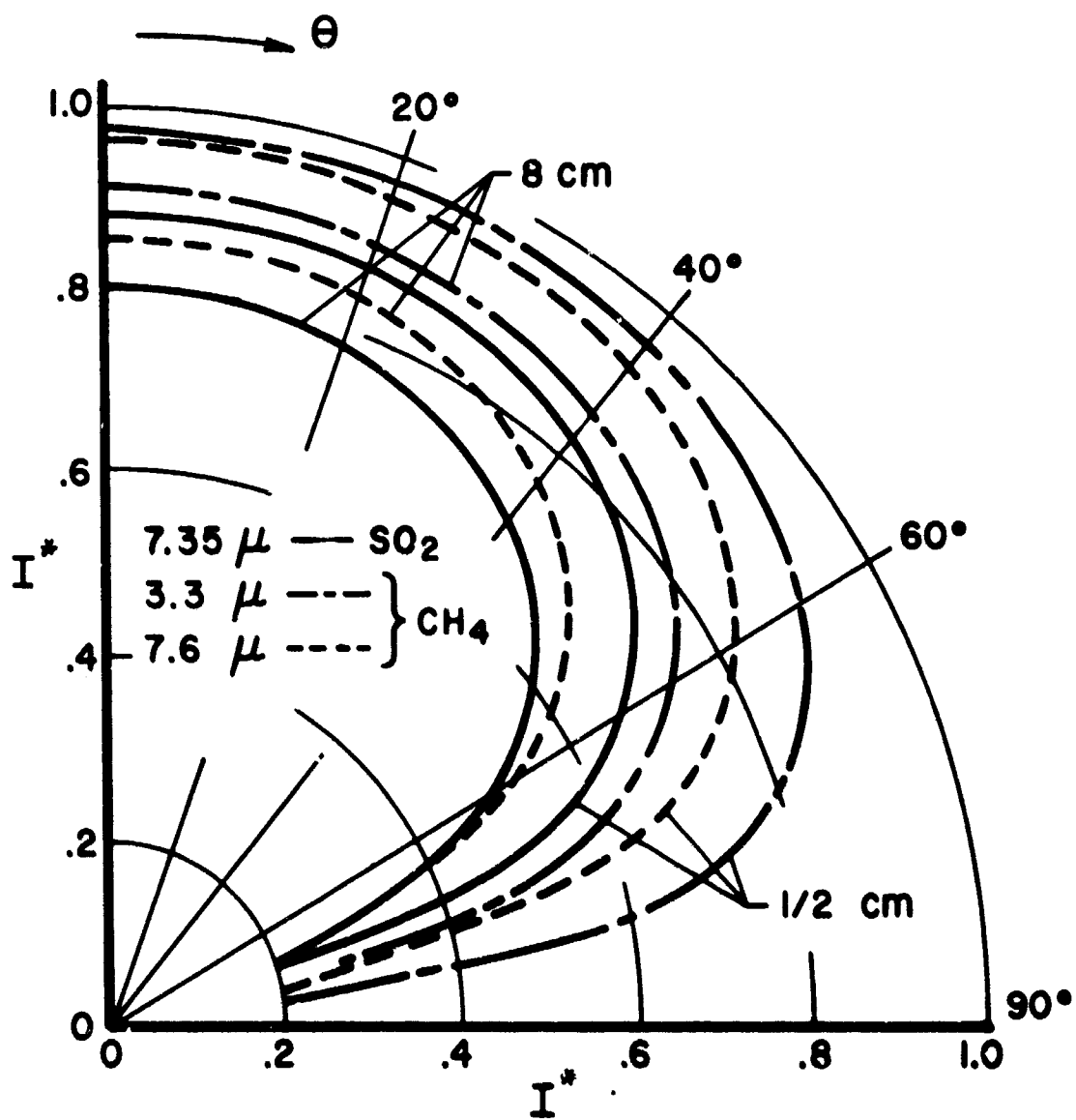


Figure 20. Emergent Intensity for  $\text{CH}_4$  and  $\text{SO}_2$  Gas Layers;  
 $T_0 = T_p = 836^\circ\text{K}$ ,  $\epsilon = 0.6$



not as great as that attenuated by the fundamental band of  $\text{CO}_2$ . On a total basis, the  $4.3\mu$   $\text{CH}_4$  band could be more effective than the  $\text{SO}_2$  fundamental band.

### 3.3.2 Experimental Results

The experimentally measured centerline gas temperature profiles with  $\text{CO}_2$  gas injected through the porous plate are shown in Fig. 21 with blowing Reynolds number as a parameter. The temperature profiles differ appreciably from those that would be expected for one-dimensional flow and heat transfer, particularly near the exit plane of the gas layer extenders. This is partly due to effective mixing of the gas streams. It was observed that the gas temperature in the exit plane could be controlled by the amount of air drawn through the hood. The air flow in the hood was so adjusted that the effect of the mixing region on the temperature distribution in the gas layer was as small as possible.

The radiation attenuation results are given in Tables 3, 4 and 5 and Fig. 22. The normal spectral emissivity of the plate increased with the level of oxidation. The emissivity of the Poroloy plate (see Fig. 23) was measured [42] and found to be a function of temperature and oxidation level. A well oxidized plate was used with a corresponding spectral normal emissivity of approximately 0.65 in the wavelength band of  $4.3\mu$ .

The effect of the blowing Reynolds number on attenuation was found to be small. The trend indicates an increase in attenuation with increasing blowing Reynolds number, but the data were not consistent enough to be conclusive. Increasing layer thickness and plate temperature enhanced the attenuation. The effect of the viewing angle was slight since only near normal directions could be observed ( $\theta < 20^\circ$ ). The polar angle affects the attenuation in two ways. First, the emissivity of the plate is a function of direction; however, the directional emissivity of metals does not vary appreciably with direction angles less than  $45^\circ$  [10]. Second, the optical path length of the radiation propagating through the gas is inversely proportional to the cosine of the angle of observation, see Eq. (2.1). For  $\theta = 20^\circ$ ,  $1/\cos\theta = 1.06$ , a value which indicates that the path length has not increased appreciably and hence no significant change is expected.

### 3.3.3 Comparison of Analysis and Experiment

The predicted temperature profiles differed appreciably from the measured ones. This discrepancy was especially large in the vicinity of the exit of the gas layer extenders. The reasons for this difference are clear. In the analysis the temperature and concentration at the edge of the layer ( $y = \delta$ ) were imposed, and the mixing region of the two opposing streams was assumed to be negligibly thin; however, flow visualization revealed extensive mixing in this region and that it extended

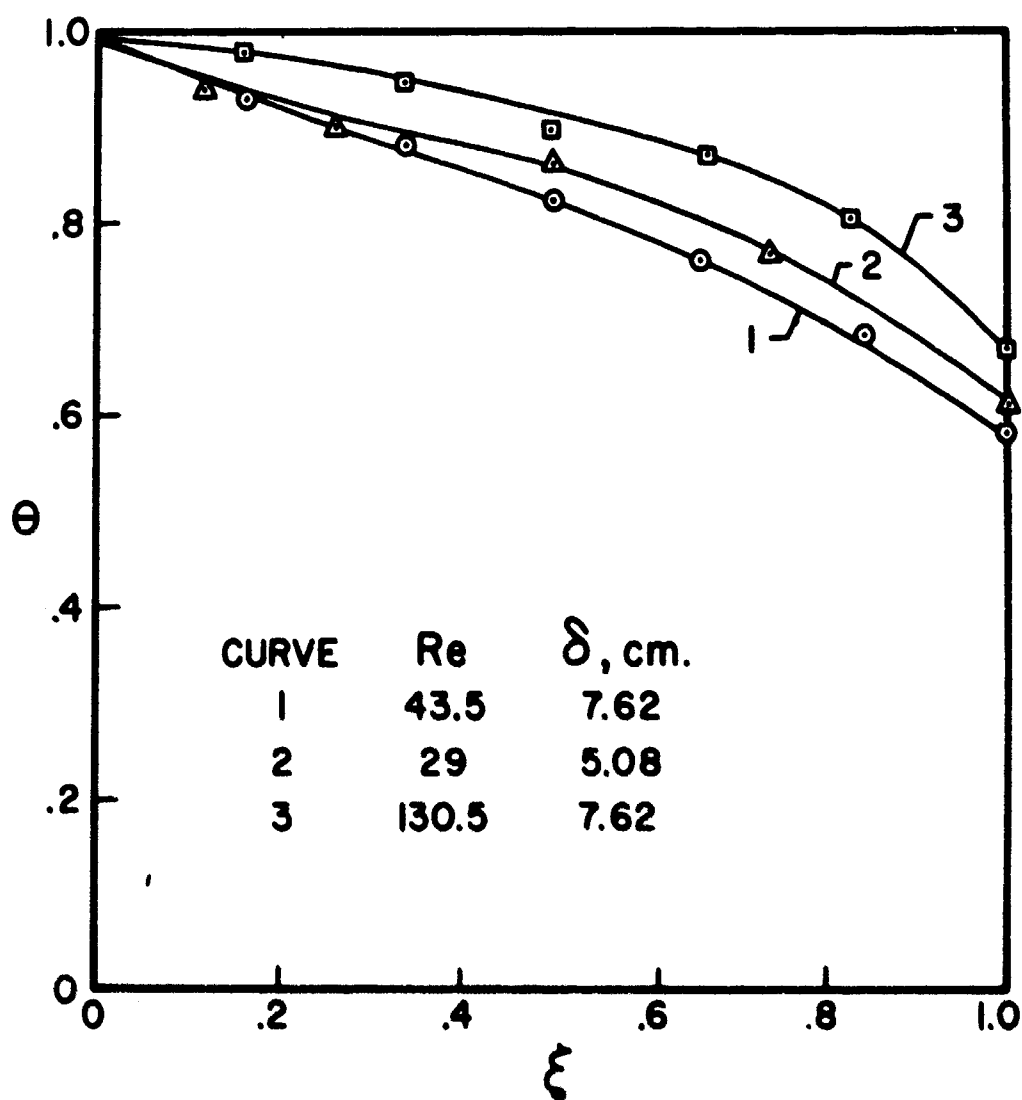


Figure 21. Measured Temperature Distribution with  $\text{CO}_2$  Gas,  
 $T_p = 822^\circ\text{K}$

Table 3. Effect of Blowing Reynolds Number on Attenuation  
for  $\delta = 7.62$  cm,  $T_p = 822^\circ\text{K}$ , and  $\theta = 0^\circ$

Re	43.5	97.0	130.5
$I_{\text{exp}}^*$	0.502	0.521	0.512

Table 4. Effects of Plate Temperature and Gas Layer Thickness  
on Emergent Band Intensity for  $\theta = 0^\circ$

$\delta$ (cm)	$T_p, ^\circ\text{K}$		
	822	960	1090
5.08	0.437	0.481	0.480
7.62	0.471	0.525	0.502
10.16	0.492	0.557	0.542

Table 5. Effect of Viewing Angle on Attenuation for  
 $\delta = 5.08$  cm,  $T_p = 960^\circ\text{K}$ , and  $\text{Re} = 29$

$\theta (^\circ)$	20	0	-20
$I_{\text{exp}}^*$	0.482	0.500	0.490

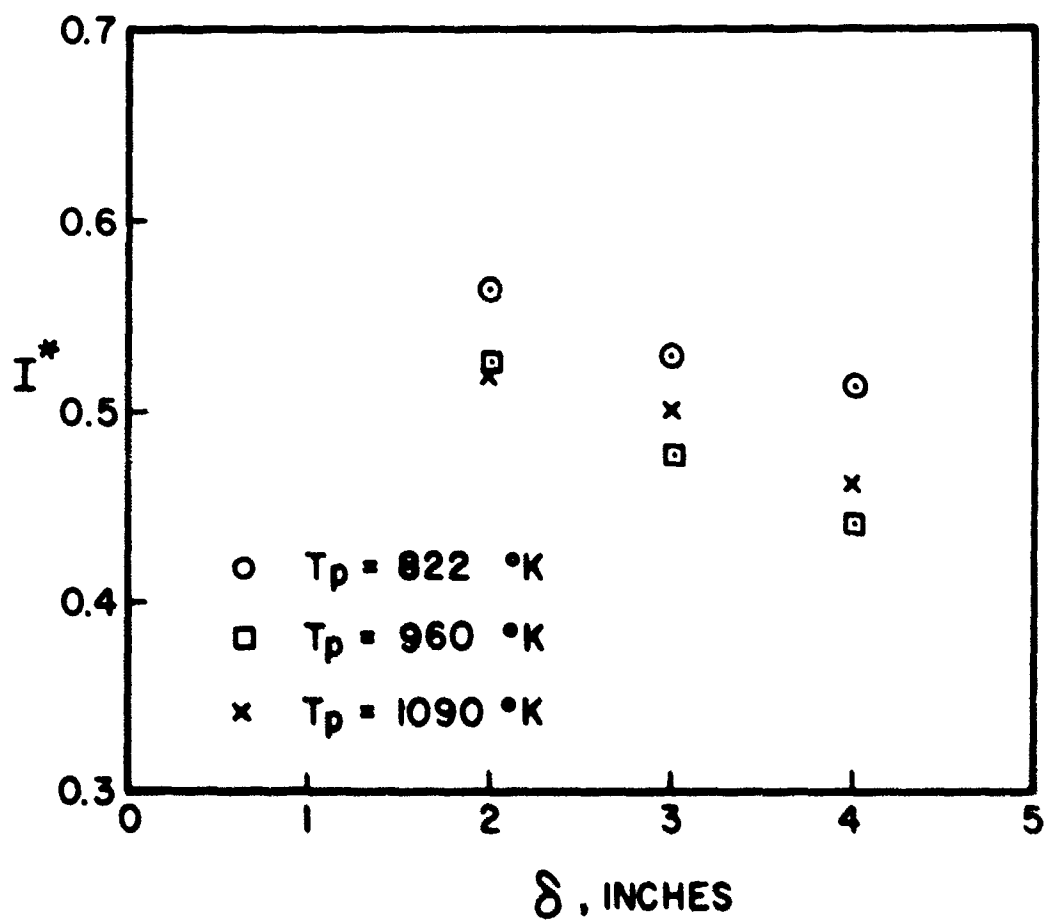


Figure 22. Effect of Gas Layer Thickness on Attenuation;  
 $m = 0.01$  lb/min,  $\theta = 0$

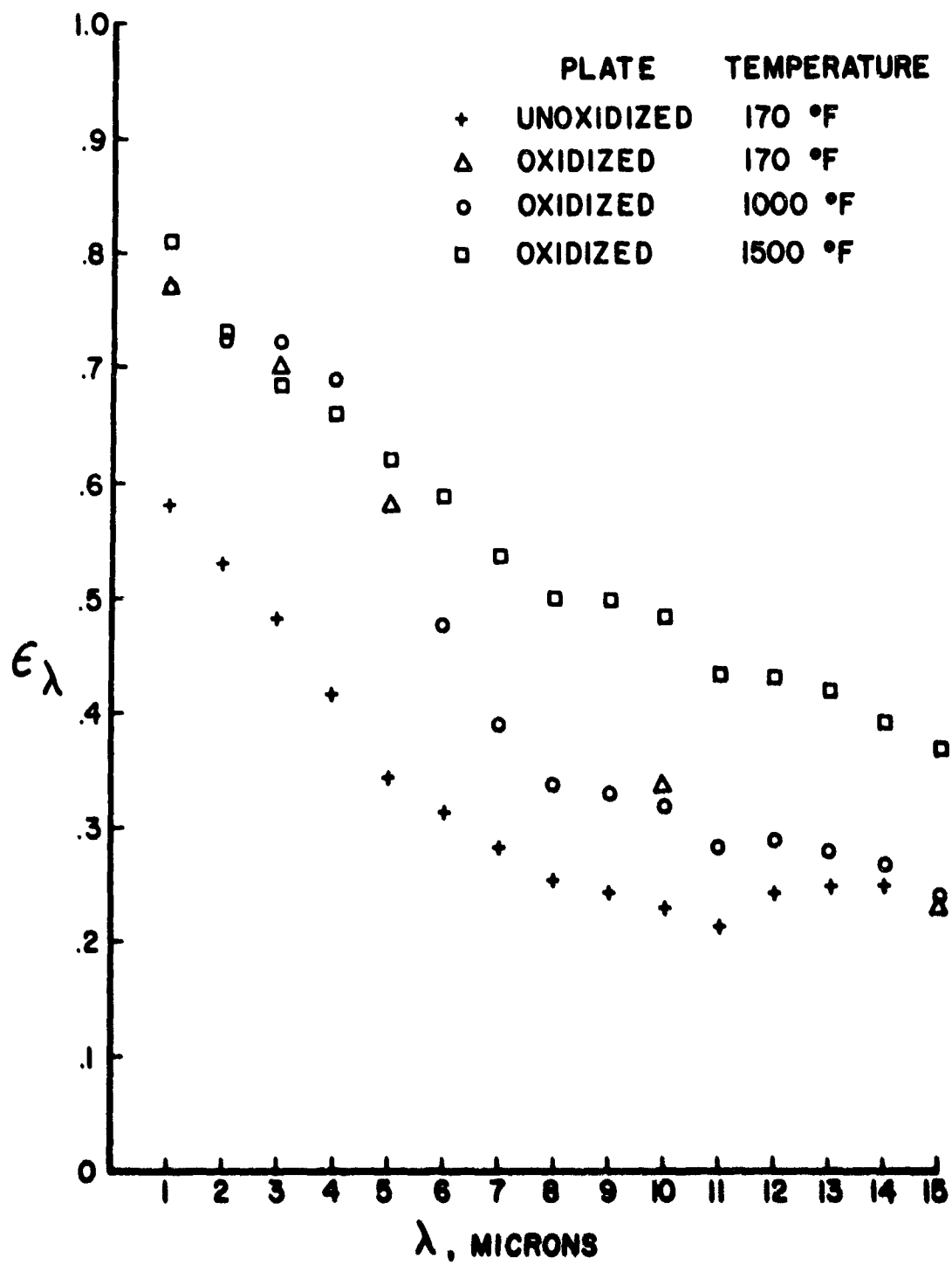


Figure 23. Normal Spectral Emittance of Oxidized and Unoxidized Poroloy Plates

below the exit plane of the gas layer curtain. Also in the analysis lateral heat conduction was neglected. Although conduction losses to the sides were reduced by insulating the metallic extenders, some energy transfer in the lateral direction could not be avoided.

The measured attenuation is larger than the predicted one. There are a number of reasons for this difference. The extension of  $\text{CO}_2$  concentration beyond the exit plane of the gas layer curtain, as already discussed, would increase the optical path and hence the attenuation. In addition, the filter band width used with the radiation detector was somewhat smaller than the effective band width defined in the analysis, Eq. (3.28), and hence a smaller attenuation has to be expected in the predictions. Also previous investigators have shown that the exponential wide band model for the total band absorptance underpredicts the total band absorptance for nonisothermal systems [43]. The introduction of an effective bandwidth was necessitated because the spectral absorption coefficient is a function of temperature, see Eq. (3.27). It should be emphasized here that the difference in the two definitions of the attenuation is caused by the fixed bandwidth of the filter as opposed to varying bandwidth in the analytical model. There was no possible logical and consistent way to adjust the correlation constants and the bandwidth in the total band absorptance equation [3, 34, 35] to correspond with the bandwidth of the wide band pass filter used with the radiation detector. For these reasons a direct comparison of experimental and analytical results remains somewhat ambiguous; however, the trends are correctly predicted by the analytical model.

## 4. ATTENUATION OF RADIATION BY AN ABSORBING GAS FLOWING OVER A HOT PLATE

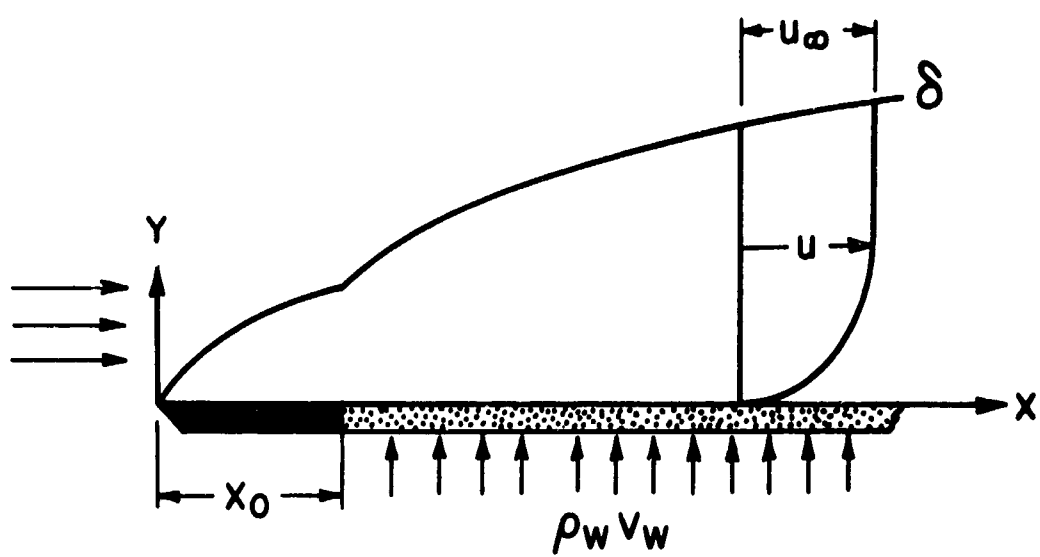
### 4.1 Analysis

#### 4.1.1 Physical Model and Assumptions

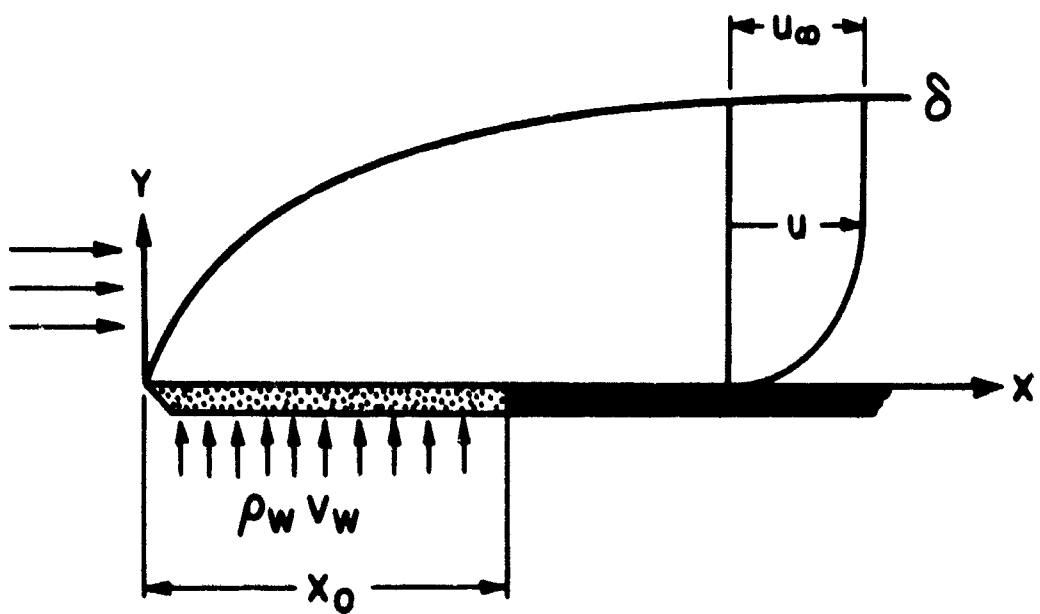
The transpiration cooling of critical structural components of jet engines, rocket motors, airfoil surfaces, etc., which are subjected to high temperatures, is an effective cooling technique and has received considerable attention [9]. This can be done by designing the porosity of the surfaces so as to obtain a desired distribution, along the walls, of normal mass flow of the coolant. In addition to the cooling, if the injected gas is also capable of absorbing radiation, the radiation leaving the hot surface will be partly attenuated and would decrease the amount of radiant energy incident on a detector some distance away. The main purpose of the present analysis is to predict the flow variables and the attenuation for an injected gas which is capable of absorbing and emitting radiation only in certain wavelength bands.

The physical model considered in the analysis is shown in Fig. 24. The model shown in Fig. 24a has a solid starting length,  $x_0$ , followed by a heated porous section. The solid plate upstream of the heated porous one is adiabatic. The coolant gas under uniform flow conditions is injected into the free stream air from the bottom of the plate. In the model illustrated in Fig. 24b the coolant is injected through a cold porous plate followed by a solid heated section having a starting length  $x_0$ . The porous plate is adiabatic and the coolant is injected uniformly into the main stream. In both models the porous and the solid plates are heated uniformly. The following assumptions are made in the analysis:

1. The flow is laminar and two-dimensional with zero pressure gradient.
2. There are no chemical reactions in the fluid.
3. The thermal diffusion and diffusion-thermo effects are negligible.
4. The transport properties are assumed to have a simple power law temperature dependence and the Prandtl and Schmidt numbers are taken to be constant.



(a)



(b)

Figure 24. Physical Models of the Problem



5. The variation of the specific heat of the coolant and mixture with temperature is neglected.
6. The velocities are low enough so that viscous heat dissipation effects can be neglected.
7. The analysis presented is restricted to porous walls of sufficient compactness to insure that the fluid and material temperatures are essentially the same throughout the wall and equal at the surface.
8. The conduction in the porous plate is one dimensional.

The multicomponent gas system is treated as an effective binary gas system composed of the main stream gas "1" and the injected gas "2". The properties of the gas mixture within the boundary layer are functions of the local temperature and concentration.

#### 4.1.2 Conservation Equations

The mathematical model for the assumed physical problem is prescribed by the conservation equations of mass, momentum, energy and species. The governing boundary layer equations for the flow of a binary, radiating gas over a porous flat plate can be written as [1, 10, 32]

$$\text{Mass:} \quad \frac{\partial(\rho u)}{\partial x} + \frac{\partial(\rho v)}{\partial y} = 0 \quad (4.1)$$

$$\text{Momentum:} \quad \rho \left( u \frac{\partial u}{\partial x} + v \frac{\partial u}{\partial y} \right) = \frac{\partial}{\partial y} \left( \mu \frac{\partial u}{\partial y} \right) \quad (4.2)$$

$$\text{Energy:} \quad \rho \left( u \frac{\partial h}{\partial x} + v \frac{\partial h}{\partial y} \right) = \frac{\partial}{\partial y} \left( k \frac{\partial T}{\partial y} \right) - \frac{\partial F}{\partial y} + \rho D_{12} \frac{\partial w}{\partial y} \frac{\partial (h_1 - h_2)}{\partial y} \quad (4.3)$$

$$\text{Species (injected):} \quad \rho \left( u \frac{\partial w}{\partial x} + v \frac{\partial w}{\partial y} \right) = \frac{\partial}{\partial y} \left( \rho D \frac{\partial w}{\partial y} \right) \quad (4.4)$$

In the formulation of Eq. (4.3), the radiative transfer in the x-direction has been neglected, following the rationale of Refs. 1 and 10. The total (integrated over the spectrum) radiative flux is given in terms of the monochromatic flux, Eq. (3.13), through the implicit definition  $F = \int_0 F_\lambda d\lambda$ .

The boundary conditions imposed are as follows:

$$\begin{aligned} \text{Momentum:} \quad u &= 0, v = v_w \text{ (a constant) at } y = 0 \\ u &\rightarrow u_\infty, v \rightarrow 0 \text{ as } y \rightarrow \infty \end{aligned} \quad (4.5)$$

Energy:  $T = T_w(x)$  at  $y = 0$  for  $x > x_0$   
 $T \rightarrow T_\infty$  as  $y \rightarrow \infty$  for  $x > x_0$  (4.6)

Species:  $w = w_w(x)$ ,  $v_{1w} = 0$  at  $y = 0$  for  $x > 0$   
or  
 $w = w_w(x)$ ,  $v_{1w} = 0$  at  $y = 0$  for  $x > x_0$  (4.7)  
 $w \rightarrow w_\infty$  as  $y \rightarrow \infty$

In transpiration cooling the local heat transfer and the rate of injection of the coolant are not independent but are coupled. Furthermore, for the case of constant heat transfer and mass injection rate at the plate, the temperatures and mass fraction distributions at the wall are not known a priori and must be determined from local heat and mass balances within the porous heat generating plate. This introduces the coolant reservoir temperature,  $T_c$ , and mass fraction,  $w_c$ , which may be realistically taken as constant. In the region between the porous plate and the coolant reservoir, it is assumed that the temperature gradients are negligible and that the coolant is in one-dimensional flow normal to the plate. Making an energy balance on an infinitesimal strip of the porous plate and neglecting axial heat conduction along the plate, leads to

$$- \left( k \frac{\partial T}{\partial y} \right)_w + c_{p2w} \rho_w v_w (T_w - T_c) + q_r = q_t \quad (4.8)$$

where  $q_t$  is the total imposed heat flux at the plate taken to be constant and  $q_r$  is the total radiant heat flux which is expressed by

$$q_r = \epsilon_w T^4 (T_{wT} - T_s^4) + \epsilon_{wB} T^4 (T_{wB} - T_s^4) \quad (4.9)$$

In writing the expression for the radiant heat transfer rate a number of assumptions and approximations have been made. The temperatures of the walls surrounding the plate,  $T_s$ , were taken to be constant and the same on both the top and bottom sides of the plate. The plate itself was treated as a gray, diffuse body having a much smaller area than the walls surrounding it. A zonal approximation [10] was employed in writing the expression for  $q_r$ . The temperatures of the top ('T') and bottom ('B') surfaces of the plate are different. The boundary condition  $v_{1w} = 0$  at  $y = 0$  asserts that the plate is impermeable to the main stream gas. Making a mass balance on an infinitesimal control volume which includes both the plate as well as the two interfaces, under the above assumption, it can be shown that  $v_w$  and  $w_w$  are related by the following equation

$$(w_c - w_w) \rho_w v_w = - \left( \rho D \frac{\partial w}{\partial y} \right)_w \quad (4.10)$$

The equation of state is given by the ideal gas law

$$p = \rho \bar{R} T \quad (4.11)$$

where

$$\bar{R} = R/\bar{M} \quad \text{and} \quad \bar{M} = 1/[(w_1/M_1) + (w_2/M_2)]$$

For a perfect gas the specific heat is independent of temperature. The mixing rules for specific heat, viscosity, thermal conductivity and diffusion coefficient are available in the literature [44]. The variation with temperature of viscosity, thermal conductivity and diffusion coefficient was approximated by the power law relations

$$\mu/\mu_\infty = (T/T_\infty)^a, \quad k/k_\infty = (T/T_\infty)^b, \quad D/D_\infty = (T/T_\infty)^c \quad (4.12)$$

where  $a$ ,  $b$  and  $c$  are empirical constants determined from experimental data over the temperature range of interest.

#### 4.1.3 Justification for Decoupling Convection from Radiation

Problems similar to the one posed in the preceding section have been considered by numerous investigators and extensive results have been reported for both gray and nongray gases as discussed previously. Similarity solutions are not possible and the presence of radiation has introduced the nonlinear integral terms in the energy equation. Approximate, iterative or finite difference approaches are some possible methods for solving the equations.

The results of nongray gas calculations have shown [45] that the use of gray absorption coefficient in the analysis overestimates the interaction of convection and radiation on temperature distribution and wall heat flux. Hence, the use of the gray approximation should also overestimate the interaction in the present problem in assessing the coupling between convection and radiation. To be specific, consider  $\text{CO}_2$  gas to be gray. Analyses have shown [10] that in addition to the classical dimensionless groups there arise several additional parameters which govern the flow and temperature fields. The parameters are the wall emissivity, and the dimensionless numbers:

$$N = k_\infty \kappa_\infty / 4\sigma T_\infty^3$$

$$\xi = 2\sigma T_\infty^3 \kappa_\infty x / \rho_\infty u_\infty c_{p\infty}$$

The parameter  $N$  represents the relative importance of conduction versus radiation, whereas  $\xi$  is a measure of the relative importance of the radiation flux to the enthalpy flux. The optical thickness based on the boundary layer thickness is estimated to be  $\tau_\delta = \kappa \delta = C(\text{Pr}N\xi)^{1/2}$  where the constant  $C$  is approximately in the range of  $5 < C < 10$  depending on  $\rho_w v_w / \rho_\infty u_\infty$ . For the conditions expected in the experimental phase of the program of interest ( $N < 0.3$ ,  $\text{Re} < 5 \times 10^5$ ,  $\text{Pr} < 1$ ,  $T_p < 1500^\circ\text{K}$  and  $(\rho_w v_w) / (\rho_\infty u_\infty) < 0.05$ ) it can readily be shown, using the data

for  $N$  [10], that the boundary layer can be definitely considered as thin,  $\tau_\delta \ll 1$ . The results of extensive calculations by numerous investigators [14, 15, 45, 46] for an optically thin boundary layer with negligible viscous dissipation, hot wall and no radiation incident on the boundary layer from some external source indicate that the effect of radiation on temperature distribution is negligible. Hence, for the present conditions it is justifiable to compute the temperature distribution by decoupling the radiation from the other modes of energy transfer and neglecting the term  $-\partial F/\partial y$  in the energy Eq. (4.3).

Additional justification for neglecting the radiation term in the energy equation is given in Figs. 15 and 16 which show that for near-stagnant  $\text{CO}_2$  gas the temperature profiles differ only by about 1% from those when radiation was neglected. Finally, the results of Schimmel et al. [26] who have studied heat transfer in a plane layer of stagnant  $\text{CO}_2$  gas bounded by two opaque walls show that the interaction is very small for wall emissivities greater than about 0.2, even when energy transfer by convection is absent.

#### 4.1.4 Integral Forms of the Conservation Equations

The mathematical difficulties of an exact solution can be circumvented by an approximate analysis which simplifies the mathematical manipulations. The justification for doing this is that in cases where exact solutions are available, they agree with satisfactory accuracy with the solutions obtained by the approximate method.

Multiplying the continuity Eq. (4.1) by  $u$ , then adding to the momentum Eq. (4.2), integrating the latter with respect to  $y$  between the limits  $y = 0$  and  $y = \delta_v$ , and by utilizing the boundary conditions, Eq. (4.5) leads to

$$\frac{d}{dx} \int_0^{\delta_v} \rho u(u_\infty - u) dy = \rho_w v_w u_\infty + \left[ \mu \frac{\partial u}{\partial y} \right]_w \quad (4.13)$$

Similarly, integrating the energy Eq. (4.3) over the thermal boundary layer thickness between  $y = 0$  and  $y = \delta_t$ , satisfying the boundary conditions Eq. (4.6) and noting that due to the dependence of  $c_p$  on composition, the enthalpy differential is given by

$$dh = c_p dT + c_{p_2} (1 - c_{p_{12}}) T dw \quad (4.14)$$

with  $c_{p_{12}} = c_{p_1}/c_{p_2}$ , the integral relation for the energy equation can be written in the form

$$\frac{d}{dx} \int_0^{\delta_t} c_p u (T_\infty - T) dy = \rho_w v_w c_p (T_\infty - T_w) + \left[ k \frac{\partial T}{\partial y} \right]_w \quad (4.15)$$

Finally, integrating the species Eq. (4.4) over the diffusion boundary layer thickness between  $y = 0$  and  $y = \delta_m$ , and by satisfying the boundary conditions, Eq. (4.7), the integral form of the species equation is obtained

$$\frac{d}{dx} \int_0^{\delta_m} \rho u (w_\infty - w) dy = \rho_w v_w (w_\infty - w_w) + \left[ \rho D \frac{\partial w}{\partial y} \right]_w \quad (4.16)$$

Since the density varies appreciably over the boundary layer thickness, Eqs. (4.13), (4.14) and (4.15) can be handled more conveniently by introducing the Dorodnitsyn transformation [47]. A new variable  $t$  is defined such that at a given value of  $x$

$$dt = (\rho/\rho_\infty) dy \quad (4.17)$$

The velocity boundary layer thickness, for example, is defined by the inverse transformation

$$\delta_v = \int_0^\delta (\rho_\infty/\rho) dt \quad (4.18)$$

If Eq. (4.17) and (4.18) are applied Eqs. (4.13) to (4.15) can be written in dimensionless form as

$$\Lambda \frac{d}{dx^*} (\Lambda F_1) = \phi \Lambda + (\rho_w \mu_w / \rho_\infty \mu_\infty) \left[ \frac{\partial}{\partial \eta} (u/u_\infty) \right]_w \quad (4.19)$$

$$\Lambda \frac{d}{dx^*} (\Lambda F_2) = \phi \Lambda (1 - T_w/T_\infty) + \frac{1}{Pr_\infty} (\rho_w k_w / \rho_\infty k_\infty) \left[ \frac{\partial}{\partial \eta} (T/T_\infty) \right]_w \quad (4.20)$$

and

$$\Lambda \frac{d}{dx^*} (\Lambda F_3) = \phi \Lambda (w_\infty - w_w) + \frac{1}{Sc_\infty} (\rho_w^2 D_w / \rho_\infty^2 D_\infty) \left[ \frac{\partial w}{\partial \eta} \right]_w \quad (4.21)$$

where

$$\begin{aligned} F_1 &= \int_0^{\delta_v/\delta} (u/u_\infty) (1 - u/u_\infty) d\eta \\ F_2 &= \int_0^{\delta_t/\delta} (c_p/c_{p_1}) (u/u_\infty) (1 - T/T_\infty) d\eta \\ F_3 &= \int_0^{\delta_m/\delta} (u/u_\infty) (w_\infty - w) d\eta \end{aligned} \quad (4.22)$$

We note that the velocity boundary layer thickness  $\delta_v$  is given by the inverse transformation, see Eq. (4.17),

$$\delta_v = \int_0^{\delta_v} (\rho_\infty/\rho) dt = \delta \int_0^1 (M_\infty T/M T_\infty) d\eta = \delta \int_0^1 [(1-w) + w(M_1/M_2)] (T/T_\infty) d\eta \quad (4.23)$$

Hence, after the temperature distribution has been determined the relationship between the velocity boundary layer thickness  $\delta_v$  and the transformed boundary layer thickness  $\delta$  can be found. Similar relations can be derived between  $\delta_t$  and  $\delta$  as well as  $\delta_m$  and  $\delta$ . For the flow treated here, however, the three thicknesses ( $\delta_v$ ,  $\delta_t$ , and  $\delta_m$ ) cannot be expected to differ greatly. Moreover, in the integral method there appear to be good mathematical reasons [48] for adopting the point of view of one thickness within which all fluid properties change from their wall values to their free stream values.

#### 4.1.5 Solution of Conservation Integral Equations

As is customary in the solution of Karman-Pohlhausen integral boundary layer equations we approximate the velocity, temperature and mass fraction profiles by nth order polynomials:

$$u = \sum_{i=0}^n a_i \eta^i \quad (4.24)$$

$$T = \sum_{i=0}^n b_i \eta^i \quad (4.25)$$

$$w = \sum_{i=0}^n c_i \eta^i \quad (4.26)$$

The coefficients  $a_i$ ,  $b_i$ , and  $c_i$  are determined so that the boundary conditions in the  $x^*-n$  plane corresponding to those [given by Eqs. (4.5-4.7)] in the  $x-y$  plane are satisfied for any value of  $\delta$  and for any value of  $T_w$  and  $w_w$ . Previous analyses have shown that sufficient accuracy for the purpose of the present investigation can be realized if fourth order polynomials are assumed.

The boundary conditions on  $u$ ,  $T$  and  $w$  in the  $x^*-n$  plane corresponding to those in the  $x-y$  plane given by Eqs. (4.5), (4.6) and (4.7) are

$$\begin{aligned} u &= 0, \quad \left[ \frac{\partial}{\partial \eta} \left( \frac{\rho u}{\rho_\infty \delta} \frac{\partial u}{\partial \eta} \right) - \rho v \frac{\partial u}{\partial \eta} \right] = 0 & \text{at } \eta = 1 \\ u &= u_\infty, \quad \frac{\partial u}{\partial \eta} = \frac{\partial^2 u}{\partial \eta^2} = 0 & \text{at } \eta = 1 \end{aligned} \quad (4.27)$$

$$\begin{aligned} T &= T_w, \quad \left[ \frac{\partial}{\partial \eta} \left( \frac{\rho k}{\rho_\infty \delta} \frac{\partial T}{\partial \eta} \right) - \rho v c_p \frac{\partial T}{\partial \eta} \right] = 0 & \text{at } \eta = 0 \\ T &= T_\infty, \quad \frac{\partial T}{\partial \eta} = \frac{\partial^2 T}{\partial \eta^2} = 0 & \text{at } \eta = 1 \end{aligned} \quad (4.28)$$

$$w = w_w, \left[ \frac{\partial}{\partial \eta} \left( \frac{\rho \rho D}{\rho_\infty \delta} \frac{\partial w}{\partial \eta} \right) - \rho v \frac{\partial w}{\partial \eta} \right] = 0 \quad \text{at } \eta = 0 \quad (4.29)$$

$$w = w_\infty, \frac{\partial w}{\partial \eta} = \frac{\partial^2 w}{\partial \eta^2} = 0 \quad \text{at } \eta = 1$$

The second boundary condition at the wall ( $\eta = 0$ ) follows from the constraint that the shear stress  $\tau_w$ , the heat flux  $q_w$  and the mass flux  $m_w$  are constant in the vicinity of the wall.

With Eqs. (4.27)-(4.29) the coefficients for the velocity, temperature and mass fraction profiles can be evaluated and they are

$$\begin{aligned} \frac{u}{u_\infty} &= (2\eta - 2\eta^3 + \eta^4) - \left( \frac{6\lambda_v}{1+\lambda_v} \right) \left( \frac{1}{3}\eta - \eta^2 + \eta^3 - \frac{1}{3}\eta^4 \right) \\ &= \left( \frac{2}{1+\lambda_v} \right) \eta + \left( \frac{6\lambda_v}{1+\lambda_v} \right) \eta^2 - \left( \frac{2+8\lambda_v}{1+\lambda_v} \right) \eta^3 + \left( \frac{1+3\lambda_v}{1+\lambda_v} \right) \eta^4 \end{aligned} \quad (4.30)$$

$$\frac{T - T_w}{T_\infty - T_w} = \left( \frac{2}{1+\lambda_t} \right) \eta + \left( \frac{6\lambda_t}{1+\lambda_t} \right) \eta^2 - \left( \frac{2+8\lambda_t}{1+\lambda_t} \right) \eta^3 + \left( \frac{1+3\lambda_t}{1+\lambda_t} \right) \eta^4 \quad (4.31)$$

$$\frac{w - w_w}{w_\infty - w_w} = \left( \frac{2}{1+\lambda_m} \right) \eta + \left( \frac{6\lambda_m}{1+\lambda_m} \right) \eta^2 - \left( \frac{2+8\lambda_m}{1+\lambda_m} \right) \eta^3 + \left( \frac{1+3\lambda_m}{1+\lambda_m} \right) \eta^4 \quad (4.32)$$

where

$$\begin{aligned} \lambda_v &= \frac{\psi}{\delta} \left( \frac{\rho_\infty \mu_\infty}{\rho_w \mu_w} - \frac{a}{6T_\infty} \left( \frac{\partial T}{\partial \eta} \right)_w \left( \frac{\mu_\infty}{\mu_w} \right) \right) = \frac{\psi}{\delta} \left( \frac{\rho_\infty \mu_\infty}{\rho_w \mu_w} \right) - \frac{ab_1}{6} \left( \frac{\mu_\infty}{\mu_w} \right) \\ \lambda_t &= \frac{\psi}{\delta} \left( \frac{\rho_\infty k_\infty}{\rho_w k_w} \frac{c_{p2}}{c_p} \right) Pr_\infty - \frac{bb_1}{6} \left( \frac{k_\infty}{k_w} \right) \\ \lambda_m &= \frac{\psi}{\delta} \left( \frac{\rho_\infty^2 D_\infty}{\rho_w^2 D_w} \right) Sc_\infty - \frac{b_1}{6} \left( c \frac{D_\infty}{D_w} - \frac{T_\infty}{T_w} \right) \end{aligned} \quad (4.33)$$

The temperature and mass fraction gradients at the wall are found from Eqs. (4.9) and (4.10). In terms of the variables here there result

$$\left[ \frac{\partial}{\partial \eta} (T/T_\infty) \right]_w = b_1 = \phi \Lambda Pr_\infty (\rho_\infty k_\infty c_{p2} / \rho_w k_w c_p) (T_w/T_\infty - \Gamma) \quad (4.34)$$

$$\left( \frac{\partial w}{\partial \eta} \right)_w = c_1 = \phi \Lambda Sc_\infty (\rho_\infty^2 D_\infty / \rho_w^2 D_w) (w_w - w_c) \quad (4.35)$$

With Eqs. (4.30), (4.31) and (4.32) the F integrals can be evaluated, and we obtain

$$F_1 = \frac{37}{315} - \frac{11}{1512} \left( \frac{6\lambda_v}{1+\lambda_v} \right) + \frac{71}{7560} \left( \frac{6\lambda_v}{1+\lambda_v} \right) - \frac{1}{2268} \left( \frac{6\lambda_v}{1+\lambda_v} \right)^2 \quad (4.36)$$

$$F_2 = \frac{37}{315} - \frac{11}{1512} \left( \frac{6\lambda_v}{1+\lambda_v} \right) + \frac{71}{7560} \left( \frac{6\lambda_t}{1+\lambda_t} \right) - \frac{1}{2268} \left( \frac{6\lambda_v}{1+\lambda_v} \right) \left( \frac{6\lambda_t}{1+\lambda_t} \right) \quad (4.37)$$

$$F_3 = (w_\infty - w_w) \left[ \frac{37}{315} - \frac{11}{1512} \left( \frac{6\lambda_v}{1+\lambda_v} \right) + \frac{71}{7560} \left( \frac{6\lambda_m}{1+\lambda_m} \right) - \frac{1}{2268} \left( \frac{6\lambda_v}{1+\lambda_v} \right) \left( \frac{6\lambda_m}{1+\lambda_m} \right) \right] \quad (4.38)$$

Since the mass injection rate along the plate is uniform,  $\rho_w v_w = \text{constant}$ , both  $T_w$  and  $w_w$  will vary in the x direction. Substituting Eqs. (4.30), (4.34) and (4.35) into Eqs. (4.19), (4.20) and (4.21), leads respectively to

$$\frac{d}{dx^*} (F_1 \Lambda) = \phi \Lambda + (\rho_w \mu_w / \rho_\infty \mu_\infty) (2\lambda_v / (1+\lambda_v)) \quad (4.39)$$

$$\frac{d}{dx^*} (F_2 \Lambda) = \phi \{ 1 - (T_w / T_\infty) + (c_{p_2} / c_p) [(T_w / T_\infty) - \Gamma] \} \quad (4.40)$$

$$\frac{d}{dx^*} (F_3 \Lambda) = \phi (w_\infty - w_c) \quad (4.41)$$

which define  $\Lambda$ ,  $T_w$  and  $w_w$  as functions of  $x$ . For an arbitrary variation of physical properties with temperature and the fact that the parameter  $\Gamma$  is a nonlinear function of  $T_w$ , no closed form solutions of the differential equations (4.39) through (4.41) are possible. Numerical integration of the equations is quite tedious and the effects of the various parameters cannot be readily determined. For this reason some justifiable assumptions and approximations will be made in order to eliminate the simultaneous solution of the equations. There are also some difficulties associated with the boundary conditions which will be discussed before the solutions can be obtained.

The radiant heat flux  $q_r$  appearing in the parameter  $\Gamma$  depends on  $x$  since  $T_w$  varies along the plate; however, for the conditions of interest  $q_r$  is considerably smaller than  $q_t$ . For this reason and the fact that Eq. (4.9) is only approximate in the first place  $q_r$  will be taken as constant. The assumption of constant  $q_r$  and hence of  $\Gamma$  is justified on the basis that the gray, diffuse, lumped parameter approximations made in deriving Eq. (4.9) and the uncertainty in the values of the emissivity are more serious than the assumption of  $q_r = \text{const}$ .



at the plate. The approximation can be improved by basing  $q_r$  on some mean plate temperature. The physical property variation with temperature is approximated by

$$\mu/\mu_\infty = k/k_\infty = T/T_\infty, D/D_\infty = (T/T_\infty)^2, c_{p2}/c_p = 1 \quad (4.42)$$

For the temperature range of interest the values of exponents  $a = b = 1$  and  $c = 2$  are slightly high. A somewhat better approximation would be  $a = b = 3/4$  and  $D = 3/2$ . Unfortunately, for this latter case an analytical solution would not be possible. It is further assumed that in the expressions for  $\lambda_v$ ,  $\lambda_t$  and  $\lambda_m$ , Eq. (4.33), the following approximations can be made:  $\Gamma(\mu_\infty/\mu_w) \approx \Gamma$ ,  $\Gamma(k_\infty/k_w) \approx \Gamma$  and  $\Gamma(D_\infty/D_w) \approx \Gamma$ . Again, in view of the assumptions already made this appears to be a reasonable compromise.

At the leading edge  $x = 0$  and at  $x = x_0$  a discontinuity in the solution exists because the boundary conditions are not continuous. Indeed, it is possible that in the immediate neighborhood thereof the boundary layer equations themselves may not be valid since the boundary layer hypothesis precludes such abrupt change in the flow variables in the  $x$ -direction. In the analysis the discontinuity has been handled by assuming that the boundary layer equations are valid. This approach can be expected to be valid provided the discontinuities of the local velocity, temperature and mass fraction within the boundary layer are relatively small [47].

The solutions of the equations corresponding to the starting conditions illustrated in Fig. 242, for example, will be presented. Substituting Eqs. (4.37) and (4.38) into Eq. (4.39) and making use of the above assumptions results in

$$\zeta - \zeta_0 = \int_{\lambda_{v,0}}^{\lambda_v} \{ [f(z) + g(z)]/h(z) \} dz \quad (4.43)$$

with

$$f(z) = [6z/\text{Pr}_\infty(1-\Gamma)]^2 \left\{ -\frac{11}{1512} \frac{1}{(1+z)^2} + \frac{71}{7560} \frac{1}{(1+z)^2} - \frac{12}{2268} \frac{2}{(1+z)^3} \right\}$$

$$g(z) = [6z/\text{Pr}_\infty(1-\Gamma)]^2 F_1(z)$$

$$h(z) = 6z/\text{Pr}_\infty(1-\Gamma) + 2/(1+z)$$

Integration of Eqs. (4.40) and (4.41) yields respectively

$$F_2\psi = (\zeta - \zeta_0)(1 - \Gamma) \quad (4.44)$$

and

$$F_3\psi = (\zeta - \zeta_0)(w_\infty - w_c) \quad (4.45)$$

In Eqs. (4.43) through (4.45)  $\zeta_0 (= x^* \phi^2)$  is the dimensionless distance along the plate at which the injection of the coolant begins, and  $\lambda_{v,0}$  is the corresponding dimensionless thickness of the boundary layer. The parameter  $\zeta_0$  can be determined by going to the limit  $\phi \rightarrow 0$  [49]. More simply, the limiting case of  $\phi \rightarrow 0$  corresponds identically to that of an impermeable wall for which the boundary layer thickness is [50]

$$\delta(x_0)/x_0 = 5.67/\sqrt{u_\infty x_0/\nu_\infty} \quad (4.46)$$

Therefore the beginning of the injection region is given by the following expression

$$\zeta_0 = \phi^2(u_\infty x_0/\nu_\infty) = 1.056\lambda_{v,0}^2 \quad (4.47)$$

Equations (4.43), (4.44) and (4.45) together with the equations for the F's, Eq. (4.36) through Eq. (4.40), complete the solution for  $\psi$ ,  $T_w/T_\infty$  and  $w_w$  as functions of  $x$ , i.e.,  $\psi = \zeta(\psi)$ ,  $T_w/T_\infty = T_w(\zeta, \psi)/T_\infty$ , and  $w_w = w_w(\zeta, \psi, T_w/T_\infty)$ . The velocity, temperature and mass fraction distributions can be computed from Eqs. (4.30) - (4.32). The solutions corresponding to the starting conditions illustrated in Fig. 24b can be given in a similar manner.

#### 4.1.6 Prediction of Attenuation

As already discussed, difficulties were encountered in making a direct comparison between the predicted and measured attenuation when using the total band absorptance model since the band width parameters could not be adjusted to correspond with those of the wide band path filter. For this reason the spectral absorption coefficient instead of the band absorptance is used to predict the band attenuation as discussed below.

Since the intensity of the external radiation,  $I_{e\lambda}$ , is much smaller than the intensity of radiation emitted from the plate,  $\epsilon_\lambda I_{b\lambda}(T_p)$ , the second term on the right-hand-side of Eq. (2.2) can be neglected. With this approximation the radiation leaving a diffusely emitting and reflecting plate reduces to

$$I_{\lambda\lambda}(0, \theta) = \epsilon_\lambda I_{b\lambda}(T_p) + \rho_\lambda \int_0^\delta I_{b\lambda}(y) e^{-\int_0^y \kappa_\lambda dy / \cos \theta} \kappa_\lambda dy / \cos \theta \quad (4.48)$$

and for a specularly reflecting plate having both directional dependent emissivity and reflectivity the spectral intensity leaving becomes

$$I_{\lambda\lambda}(0, \theta) = \epsilon_\lambda(\theta) I_{b\lambda}(T_p) + \rho_\lambda(\theta) \int_0^\delta I_{b\lambda}(y) e^{-\int_0^y \kappa_\lambda dy / \cos \theta} \kappa_\lambda dy / \cos \theta \quad (4.49)$$

With  $I_{\lambda}(0, \theta)$  determined, the spectral normalized intensity  $I_{\lambda}^*(\delta, \theta)$  and the band intensity  $I^*(\delta, \theta)$  can be predicted from Eqs. (2.4) and (2.5), respectively, if the spectral absorption coefficient is known.

Since the integration is along a nonisothermal and non-homogeneous path, the spectral absorption coefficient  $\kappa_{\lambda}$  must be known as a function of temperature and composition. The values of  $\kappa_{\lambda}$  were therefore taken from the computations of Malkmus [51] who presented spectral emissivity data as a function of temperature for the weak and strong line limits. Briefly, he assumed a harmonic oscillator for the  $\text{CO}_2$  molecule and a random Elsasser array for the line structure. The assumptions and the models are more completely discussed elsewhere [2, 52]. In general, the weak and strong line limits are valid when the emissivity (or absorptivity) of the band center is well below and near unity, respectively. The use of the results of Malkmus is somewhat arbitrary. However, due to the lack of experimental data in the temperature range of interest, the fact that other computations [53-54] differ little from his results and they compare well with the available experimental data [55] the values of  $\kappa_{\lambda}$  should be quite adequate.

## 4.2 Experiment

### 4.2.1 Description of Experimental Facility

The principal equipment used in the experimental work of this research program was a continuously operating, open circuit, subsonic wind tunnel with a design capacity of approximately  $M = 0.2$  at a volumetric flow rate of 12,000 cubic feet per minute. A sketch of the subsonic wind tunnel is shown in Fig. 25. The wind tunnel consists of a blower, numerous flow straighteners, a test section, an intake bypass valve (butterfly gate) and a blower control gate.

The blower comprises an air compressor and an electric motor. The compressor is a Spencer Turbo-Compressor. It is a high capacity, low pressure differential fan. The electric motor is of the line start induction type and is manufactured by Allis Chalmers. This motor is designed for 300 HP at 1760 RPM while drawing 70 amperes of 3 phase 60 cycle current at 2300 volts.

The flow straighteners are made of cardboard tubes that have been bound together and placed at the tunnel entrance section. They are necessary to reduce entrance turbulence which could propagate and produce undesirable effects in the test section.

The wind tunnel test section is located on the intake side of the tunnel and is one foot square (the same dimensions as the intake duct) and has three sides constructed from plexiglass to facilitate visual and photographic observation. One

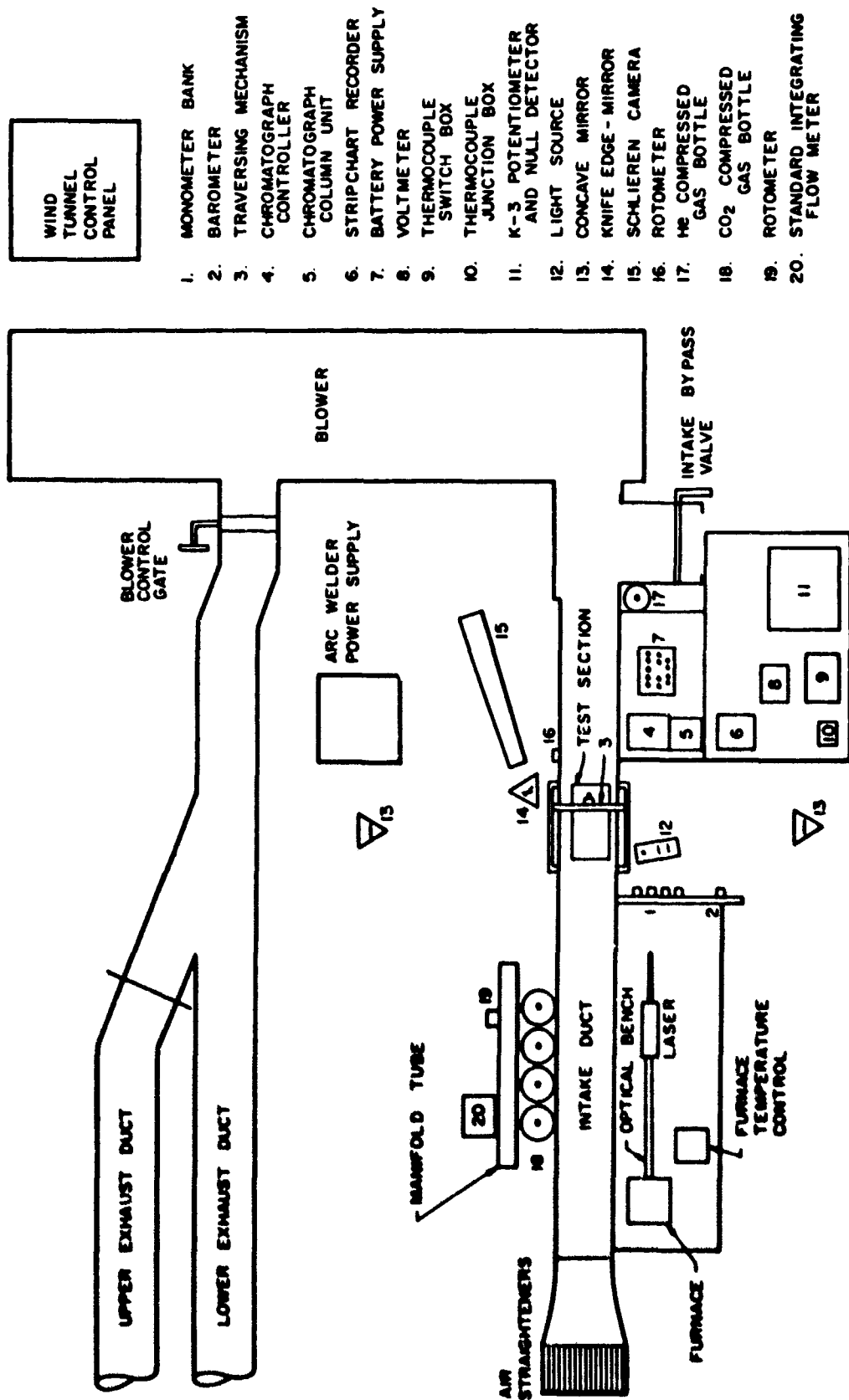


Figure 25. Schematic Diagram of the Facility

side wall is made of sliding plexiglass mounted on gear racks and serves as an access to the test section as well as pitot-static tube scanner support in both the horizontal and vertical directions. The plexiglass plate in the top panel of the test section has a viewing port for the radiometer and is also provided with access ports for velocity, temperature and gas sampling probes.

The intake bypass valve serves for the control of the flow rate and consequently the velocity in the test section while operating the blower at rated capacity. The blower control gate is used primarily for bringing the flow rate up to a desired capacity during the starting cycle. Starting of the motor must be done at minimum load; hence the blower control gate has to be kept closed until the motor starter has deactivated. The gate is then slowly opened to achieve the desired flow capacity. Figure 26 is an overall photograph of the test facility.

#### 4.2.2 Test Assembly

The test assembly consists of the traversing mechanism, support stand, and test section. A photograph of the test apparatus is shown in Fig. 27.

The traversing mechanism is the same yoke-shaped one used in the near-stagnant experiments and straddles the test section. Both the radiation detector and the gas sampling probe were mounted on the yoke. The design and the functions of the traversing have already been described in Section 3.2.1. The traversing mechanism was again mounted on a suitable support stand, see Fig. 27.

Two plate configurations were considered in the experimental investigation. The first plate arrangement was made of a one-inch-long starting length followed by a three-inch-long porous heated plate. A schematic sketch of this system is shown in Fig. 24a. The second configuration comprised a three-inch-long porous starting length joined to a three-inch-long solid heated plate. The sketch of this arrangement is shown in Fig. 24b.

The plates were electrically heated with two DC arc welders connected in parallel. The radiation-absorbing gas was supplied from a cylinder equipped with a suitable metering system which has already been described in Section 3.2.3.

#### 4.2.3 Instrumentation and Calibration

The techniques for the measurement of the plate surface temperature, gas temperature, injection flow rate, power and the radiative flux have already been described in Sections 3.2.2 and 3.2.3 and will not be repeated here.

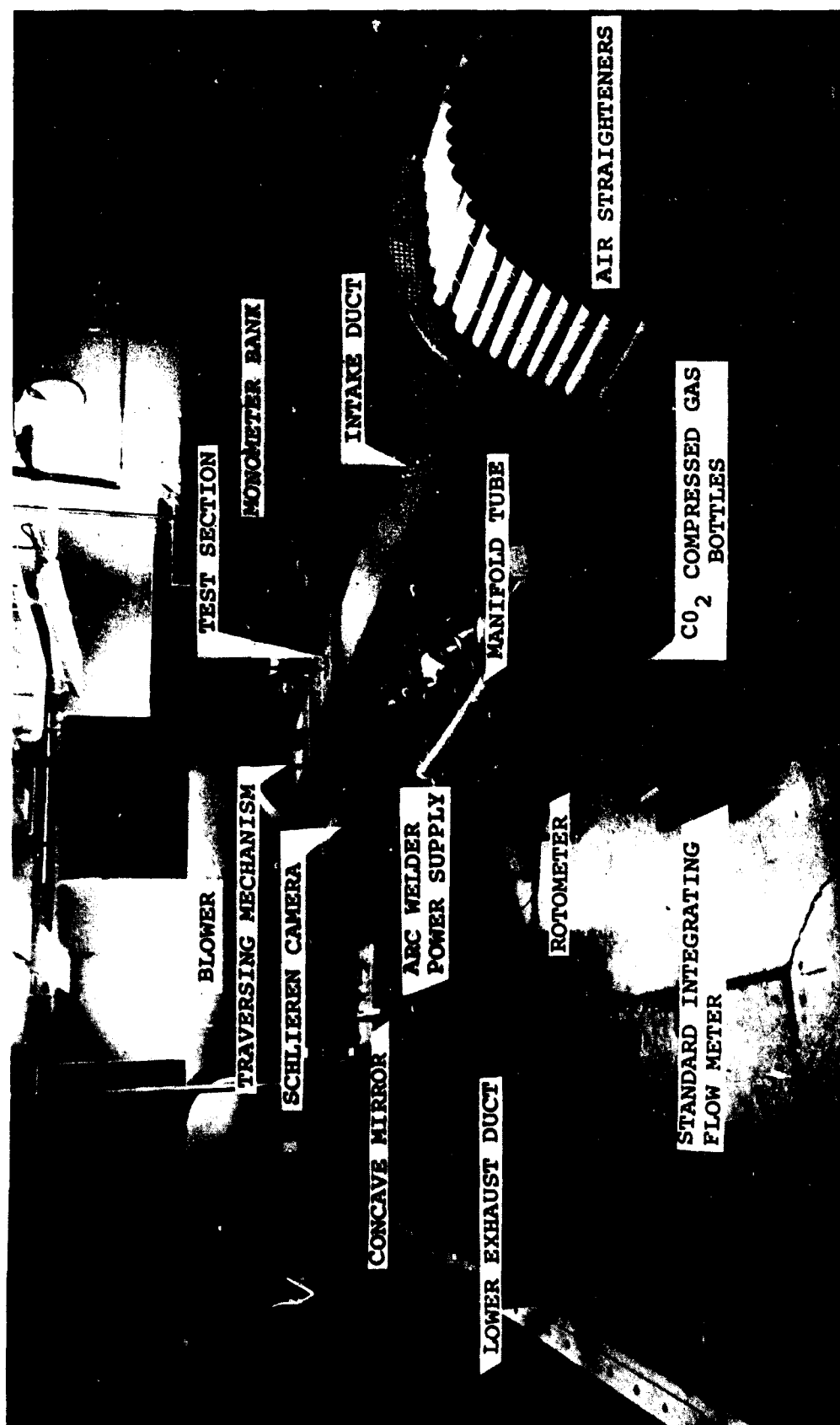


Figure 26. Photograph of the Intake Side of the Wind Tunnel

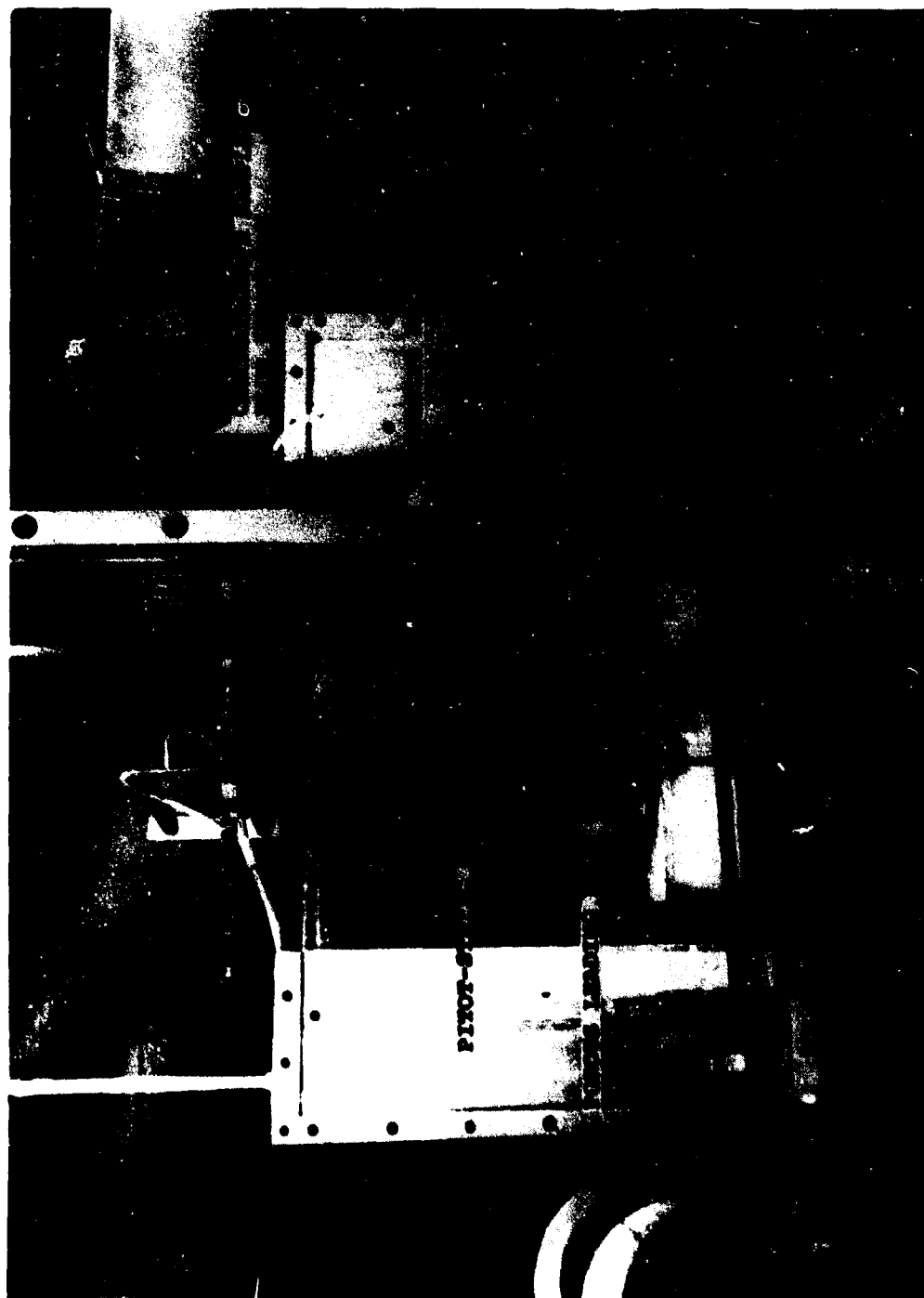


Figure 27. Photograph of the Test Section

The aspirating probe for the gas temperature measurements was adapted to a gas chromatograph to determine the concentration of the injected species. For this reason, this probe is also referred to as the gas sampling probe. It was mounted on the traversing mechanism and could be accurately positioned in the boundary layer with an adjustable rod.

Standard pitot-static probes were used in conjunction with water filled manometers to determine velocity profiles in the test section. The performance characteristics of the wind tunnel were determined and it was found that the velocity profiles in the test section were sufficiently uniform under all conditions investigated.

Schlieren photographs were taken in the vicinity of the plates under various injection rates and wind-tunnel operating conditions. The Schlieren apparatus provides a qualitative picture representative of the variation of density throughout the flow field of interest [56]. The arrangement of the particular Schlieren apparatus used in this investigation is schematically illustrated in Fig. 25.

The concentration of carbon dioxide was measured with a thermal conductivity vapor phase fractometer, commonly referred to as a gas chromatograph [57]. It is similar in its design features to a Perkin-Elmer Model 154-B Vapor Fractometer. A schematic diagram of the gas chromatograph is depicted in Fig. 28. The concentration measurements were made by withdrawing samples of the gas mixture from different locations above the test plate. The sampling technique is illustrated in Fig. 29. The instrument was calibrated with three different air-carbon dioxide mixtures of known composition supplied by the Matheson Gas Co. A conventional procedure [57] was employed to calibrate the instrument.

#### 4.2.4 Test Procedure

The velocity, temperature and concentration fields as well as attenuation of radiation leaving the test plate were measured in a series of experiments. Depending on the particular quantity measured, the pertinent equipment was properly arranged, aligned and the wind tunnel started. As soon as the desired test conditions were achieved, the specific measurements were initiated.

For instance, the structure of the boundary layer for various free stream, injection and heating conditions was studied with a Schlieren apparatus. In case of adiabatic experiments,  $\text{CO}_2$  was injected into the free stream at a preselected rate. The development of concentration boundary layer was observed visually on a frosted glass screen in the image plane of the camera lens. Upon final adjustments of the position of the knife edge for maximum contrast of the image, Polaroid film was exposed, developed and fixed in standard manner.



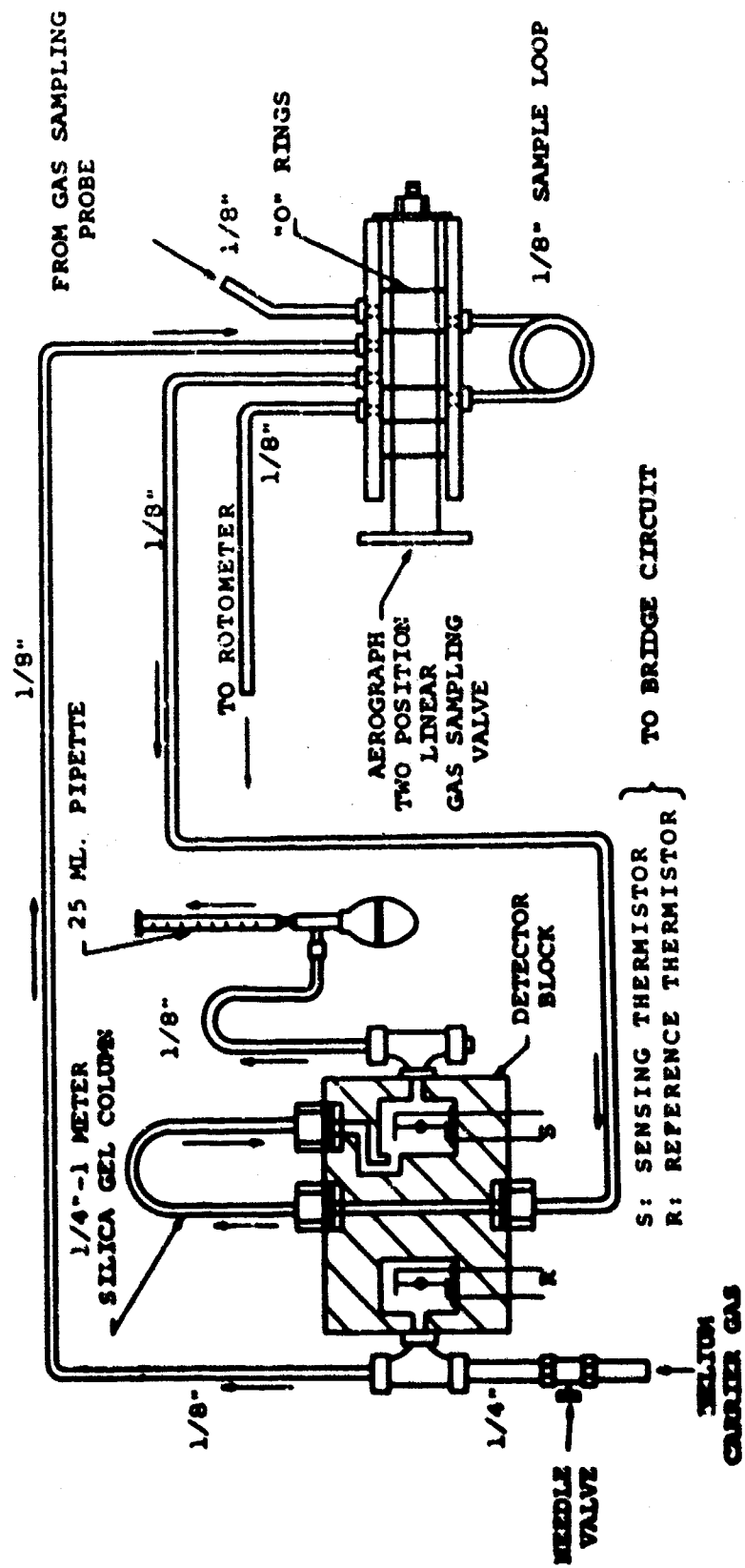


Figure 28. Schematic Diagram of the Gas Chromatograph

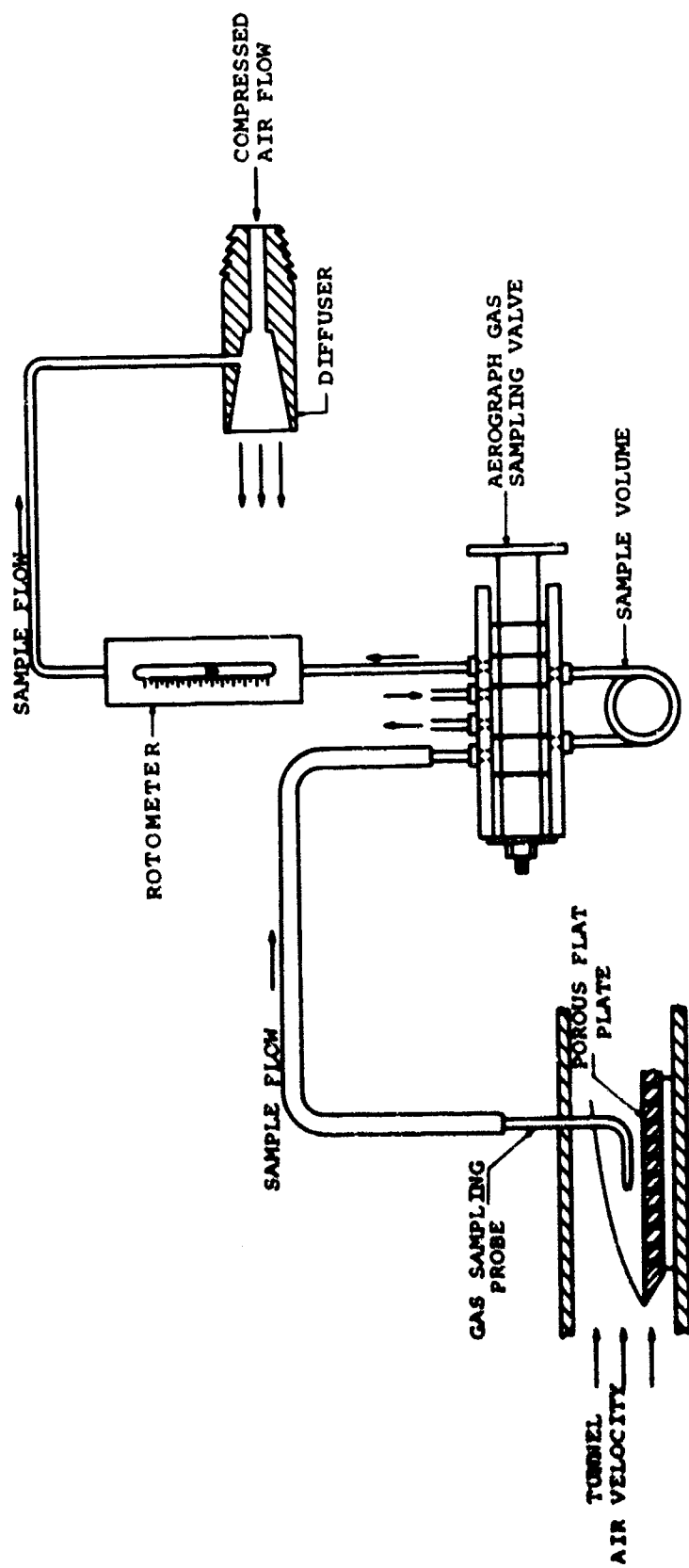


Figure 29. Flow Diagram of the Gas Chromatograph

The carbon dioxide concentration measurements in the boundary layer were made subsequently. The gas sampling probe which is similar in construction to the Pitot probe with 1/16 inch diameter opening was attached to the top panel of the test section and could be positioned vertically. An air diffuser which is an integral part of the gas chromatograph was activated causing a small sample of gas to flow from the boundary layer through the instrument. The flow rate of the sample gas was measured with a rotometer, see Fig. 29, and adjusted to the desired level by controlling the discharge rate of the compressed air flowing through the diffuser. The sample was isolated and passed with the carrier gas (He) through the column of the gas chromatograph. Finally, the fractogram was recorded with a strip chart recorder and analyzed.

The gas sampling probe was also used as an aspirating probe for temperature measurement in the boundary layer. After a desired plate surface temperature was achieved by proper adjustment of the electrical power supply (Westinghouse DC arc welders) the temperature and velocity profiles in the boundary layer were measured at a given distance from the leading edge. Unfortunately, the plate surface temperature was limited by the inadequate power available at the wind tunnel which prevented the study of attenuation over a wide enough range at experimental conditions.

Upon completion of the desired velocity and temperature measurements the probe was removed and the radiation detector described earlier was positioned above the plate without interfering with the flow field. As a consequence of the construction features of the wind tunnel only near normal ( $\theta < 20^\circ$ ) radiation flux measurements were feasible. Once it was decided upon plate configuration, free stream, injection and surface temperature conditions, attenuation measurements were first made with a nonabsorbing gas (air) and then repeated under otherwise identical conditions by injecting an absorbing gas ( $\text{CO}_2$ ).

#### 4.3 Results and Discussion

##### 4.3.1 Analytical Results

Since there is an even larger number of independent parameters than for the near-stagnant gas layer [i.e.,  $\text{Re}_x$ ,  $\phi$ ,  $\zeta$ ,  $\text{Pr}$ ,  $\text{Sc}$ ,  $\Gamma$ ,  $\zeta_0$ ,  $T_w$ ,  $T_c$ ,  $T_s$ ,  $w_c$ , plate arrangement, radiation characteristics of the plate, incident radiation, radiation characteristics of the gas, physical properties of the fluids (constants  $a$ ,  $b$ , and  $c$ ), etc.], it is impractical to cover a complete range of parameters which may be of possible interest. For this reason only sample results are presented for the diffusely emitting and reflecting plate in the absence of external radiation with air as the free stream fluid ( $\text{Pr}_\infty = 0.70$ ) and carbon dioxide ( $\text{Sc}_\infty = 0.5$ ) as the injected fluid. The effects of plate emissivity and emergent direction have already been discussed at some length in Section 3.1.3 and therefore will not be repeated.

In the ensuing discussion only the effects of flow and injection variables upon the attenuation for given heating conditions will be emphasized since the mass fraction and temperature of the absorbing gas in the boundary layer are functions of these parameters.

The solutions as calculated from Eqs. (4.44), (4.45), (4.46) and (4.47) are shown in Figs. 30 and 31 for starting length parameters of  $\zeta_0 = 0$  and  $\zeta_0 = 5$ , respectively. In Figs. 30a and 31a the dimensionless parameter  $\psi$  which is a blowing Reynolds number based on  $\delta$  as the characteristic dimension is plotted against the parameter  $\zeta$  ( $= Re_x \phi^2$ ). Inspection of the figures reveals that the relation between  $\psi$  and  $\zeta$  is linear except for  $\zeta < 1$ . The variation of the parameters  $\lambda_v$ ,  $\lambda_t$  and  $\lambda_m$  with  $\zeta$  is illustrated in Figs. 30b, 30c and 30d, respectively. These parameters characterize the velocity, temperature and concentration boundary layer thicknesses, see Eq. (4.34). It is seen from the figures that the dimensionless boundary layer thicknesses  $\lambda_v$ ,  $\lambda_t$  and  $\lambda_m$  all increase with the increase in the dimensionless heat flux parameter  $\Gamma$ . We note that  $\Gamma = 1$  corresponds to adiabatic flow over a plate which is maintained at the same temperature as the main free stream gas. When the injection of fluid begins at a certain distance from the leading edge of a plate the boundary layer thickness at the beginning of the porous section is taken to be that at the end of the impermeable section. This explains the difference between the results in Figs. 30 and 31.

The variation of the temperature and the mass fraction of the injected species along the wall are illustrated in Figs. 32a and 32b, respectively. Both the wall temperature and the wall mass fraction of  $CO_2$  increase with  $\zeta$ . The mass fraction at the wall,  $w_w$ , for  $\Gamma = 4$  was very close to that for  $\Gamma = 2$  and separate curves could not be drawn. As expected the effect of  $\Gamma$  is much greater on  $T_w$  than on  $w_w$ . As  $\zeta$  becomes large,  $T_w/T_\infty \rightarrow \Gamma$  and  $w_w \rightarrow 1$ . This limiting behavior is expected on physical grounds.

The variation of the temperature profiles in the boundary layer is illustrated in Fig. 33. The dimensionless velocity ( $u/u_\infty$ ) and mass fraction  $[(w-w_w)/(w_\infty-w_w)]$  profiles in this type of plot are within a fraction of a percent from those of the temperature for corresponding values of  $\phi$  and  $Re_x$ , and hence separate curves are not presented. The abscissa  $y\psi/\delta\phi$  instead of  $y/\delta$  was purposely chosen so that the profiles for different values of parameter  $\phi$  would be separated. The results show that the boundary layer thickness increases with  $\phi$  and  $\Gamma$ , see Figs. 33a and 33b. Even though direct comparison is not possible because of different boundary conditions and temperature dependence of physical properties considered, the trends in the results presented in the figure agree with those of previous investigators [49, 58, 59]. It is noted that because of injection of the fluid along the plate, inflection points appear in the temperature (velocity and mass fraction) profiles. It is

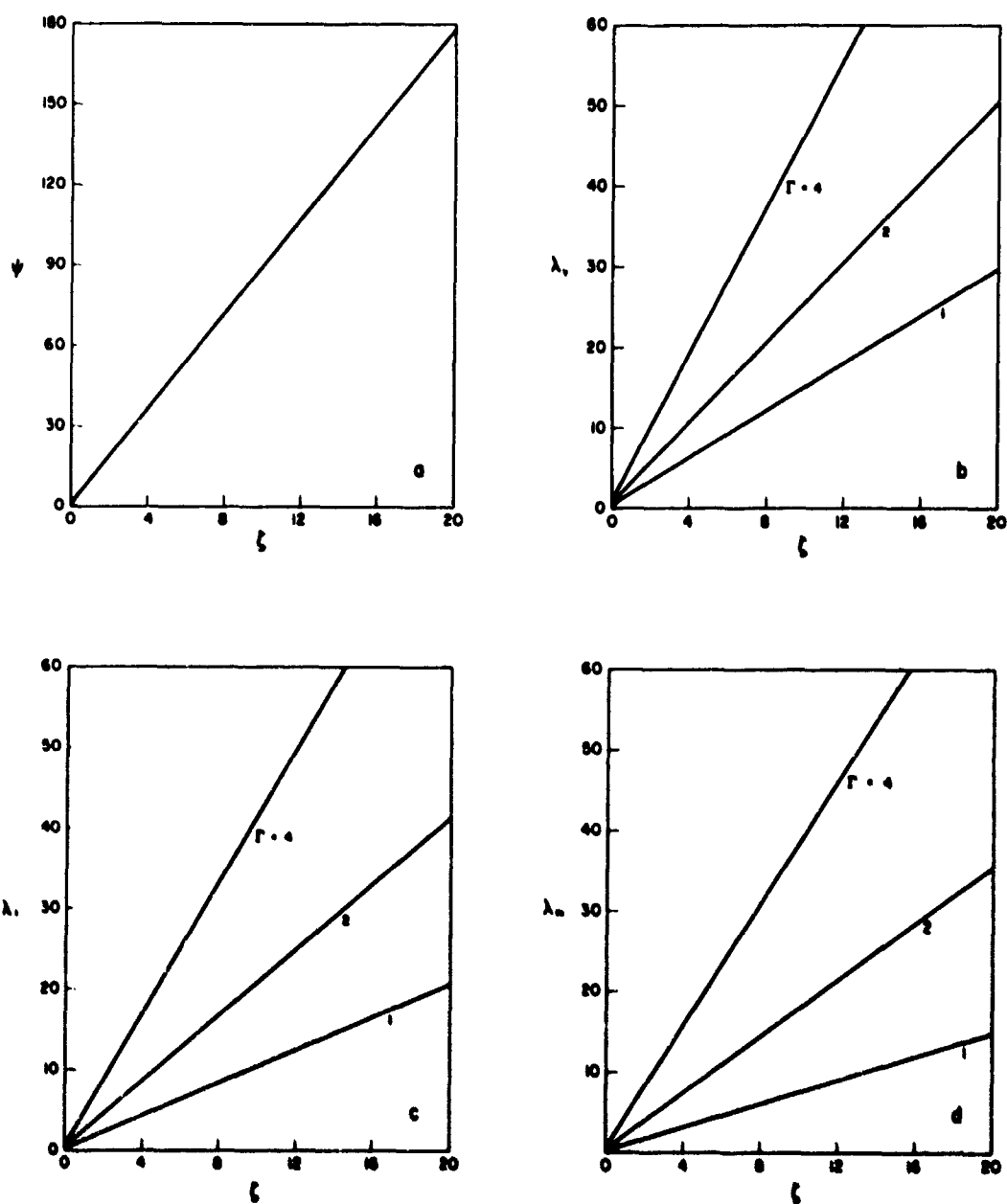


Figure 30. Variation of the Parameters  $\psi$ ,  $\lambda_v$ ,  $\lambda_t$  and  $\lambda_m$  with  $\zeta$  for Different  $\Gamma$ ;  $\zeta_0 = 0$ ,  $Pr = 0.7$ ,  $Sc = 0.5$

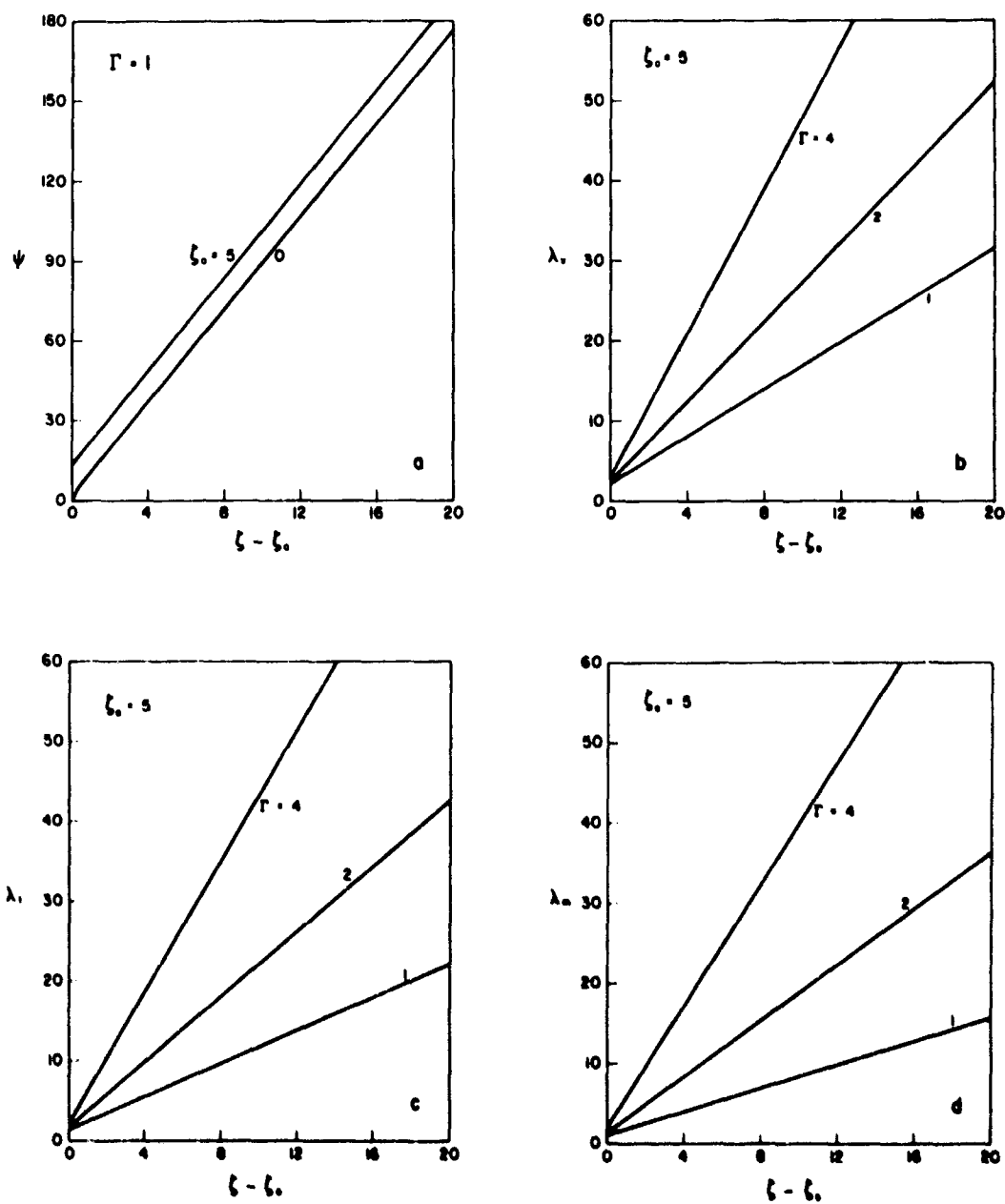


Figure 31. Variation of the Parameters  $\psi$ ,  $\lambda_v$ ,  $\lambda_t$  and  $\lambda_m$  with  $\zeta - \zeta_0$  for Different  $\Gamma$ ;  $\zeta_0 = 5.0$ ,  $Pr = 0.7$ ,  $Sc = 0.5$

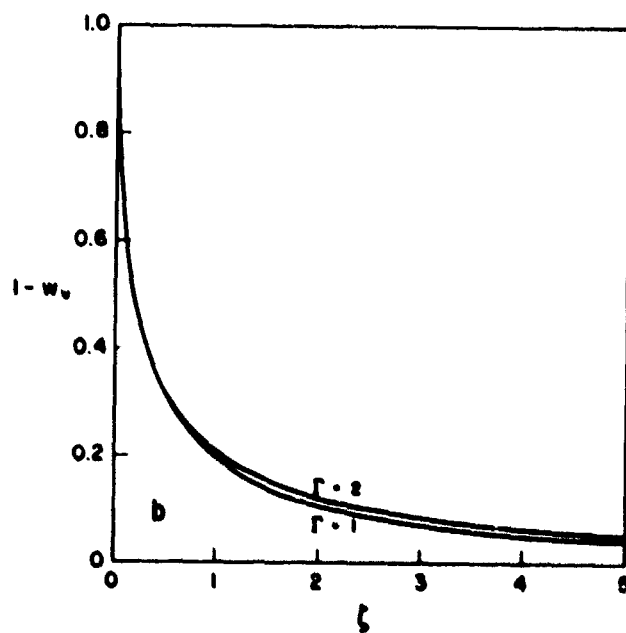
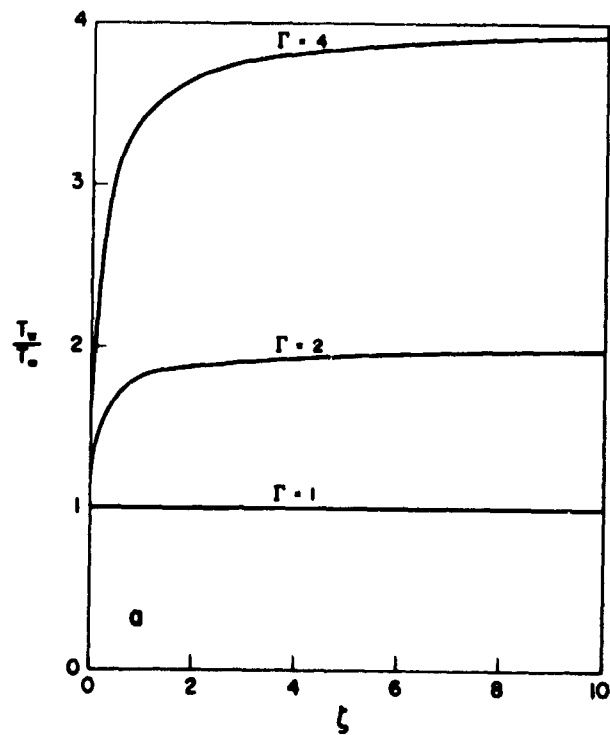


Figure 32. Variation of Wall Temperature and Wall Mass Fraction Along the Plate for Different  $\Gamma$ ;  $\zeta_0 = 0$ ,  $Pr = 0.7$ ,  $Sc = 0.5$

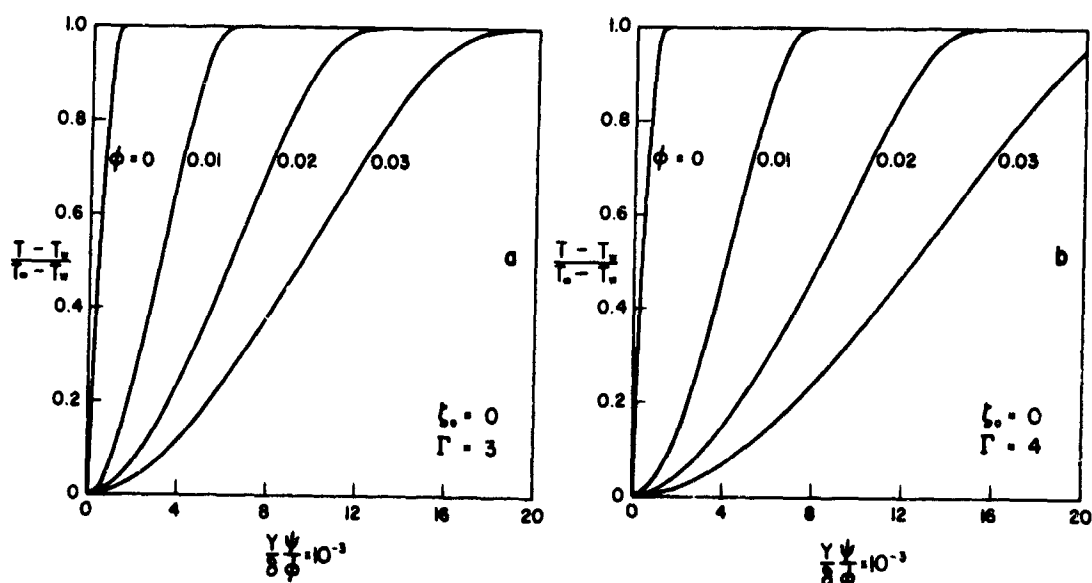


Figure 33. Temperature Distribution in the Boundary Layer for Different  $\phi$ ;  $\zeta_0 = 0$ ,  $Pr = 0.7$ ,  $Sc = 0.5$

found that the larger the value of  $\phi$  the further the inflection point moves outwards from the plate. The instability of the laminar boundary layer may be interpreted from the inflection points occurring in these curves.

The effect of injection parameter,  $\phi$ , and the temperature (parameter  $\Gamma$ ) on the attenuation of radiation in the  $4.3\mu$  band of  $CO_2$  is illustrated in Figs. 34a and 34b based on the weak-line and strong-line approximations, respectively. The spectral attenuation was computed by numerically integrating Eq. (2.5) and using the spectral absorption coefficients from the weak- and strong-line limits as discussed in Section 4.1.6. The attenuation based on the weak-line approximation is greater at all wavelengths than the strong-line approximation which is consistent with the definition of  $\kappa_\lambda$  [51]. The parameters  $\Gamma = 3$  and  $\Gamma = 4$  correspond to the plate surface temperature of about  $T_w = 1500^\circ R$  and  $T_w = 2000^\circ R$ , respectively. It is seen that in this temperature level range the broadening of the band by temperature is small. The band attenuation is larger for  $\Gamma = 4$  than for  $\Gamma = 3$ . The effect of the injection parameter,  $\phi$ , on the attenuation is as expected. With the increase in mass of  $CO_2$  in the boundary layer the attenuation also increases.

The dependence of the integrated band intensity  $I^*$  on the parameter  $\zeta$  is shown in Figs. 35a, 35b, 35c, and 35d for  $Re_x = 2.5 \times 10^4$  with  $\Gamma = 3$  and 4 as well as for  $Re_x = 10 \times 10^4$  with  $\Gamma = 3$  and 4. The effects of direction  $\theta$  on attenuation have already been discussed at some length in Section 3.3.1 and the results are given therefore only for the normal ( $\theta = 0$ ) direction. This of course is the most critical since the



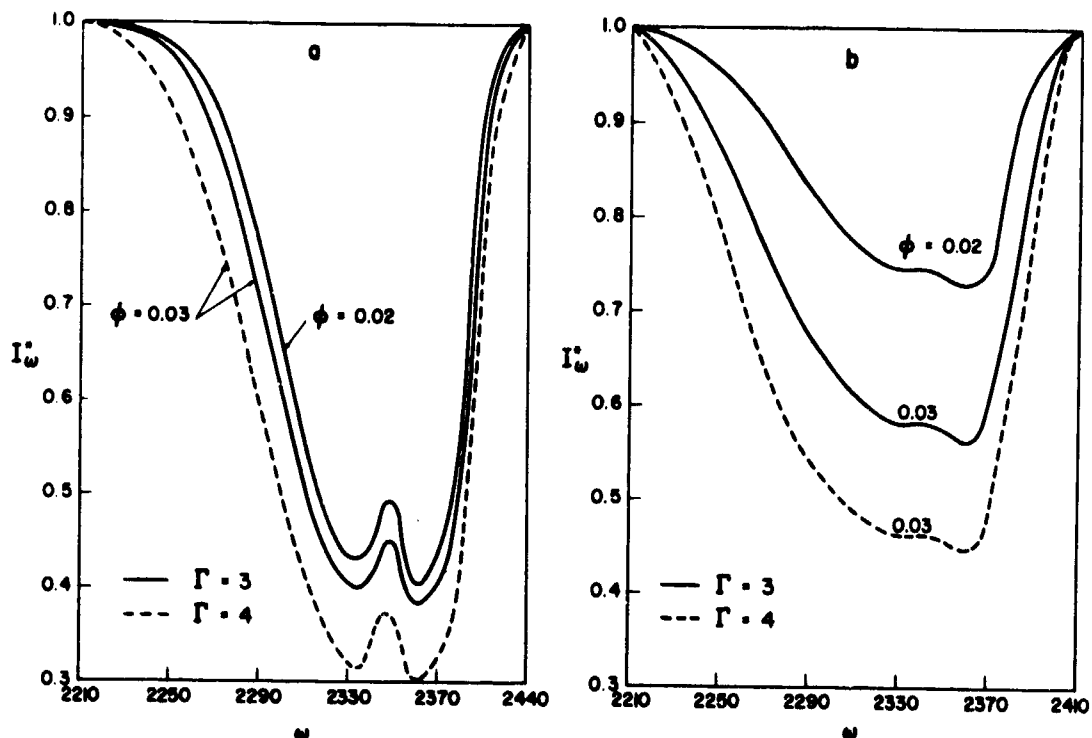


Figure 34. Effect of  $\phi$  and  $\Gamma$  on the Normalized Emergent Spectral Intensity with  $\text{CO}_2$  Injection;  $x_0 = 0$ ,  $\text{Re}_x = 10 \times 10^4$ ,  $T_\infty = 530^\circ\text{R}$ ,  $\epsilon = 1$

attenuation is minimum. It is seen from the figure that for  $\epsilon = 1$  and small  $\zeta$  the attenuation increases (weak-line approximation) rapidly with  $\zeta$  but then it levels off and the additional mass of  $\text{CO}_2$  in the boundary layer becomes rather ineffective in attenuating radiation as was the case for the near-stagnant layer. The strong-line approximation predicts, on the other hand, a more gradual increase in  $I^*$  with  $\zeta$ . It is noted that for  $\epsilon = 0.5$  there is a maximum in  $I^*$  with  $\zeta$ . This is due to the emission as well as reflection by the plate of the radiation emitted by  $\text{CO}_2$  in the boundary layer and is consistent with the definition of  $I^*$ , see Eqs. (2.1), (4.48) and (2.5). Comparison of results presented in Figs. 35a and 35b with those given in Figs. 35c and 35d show that for a given  $\zeta$ , radiation is attenuated more effectively for lower  $\text{Re}_x$ . That is, for smaller free stream velocities, smaller injection is needed to achieve the same attenuation. The attenuation is larger for  $\Gamma = 4$  than for  $\Gamma = 3$ . The effects of plate emissivity on  $I^*$  agree with those for the near-stagnant layer; however, the influence of  $\epsilon$  on  $I^*$  is stronger than that illustrated in Fig. 18 but the trends are still the same.

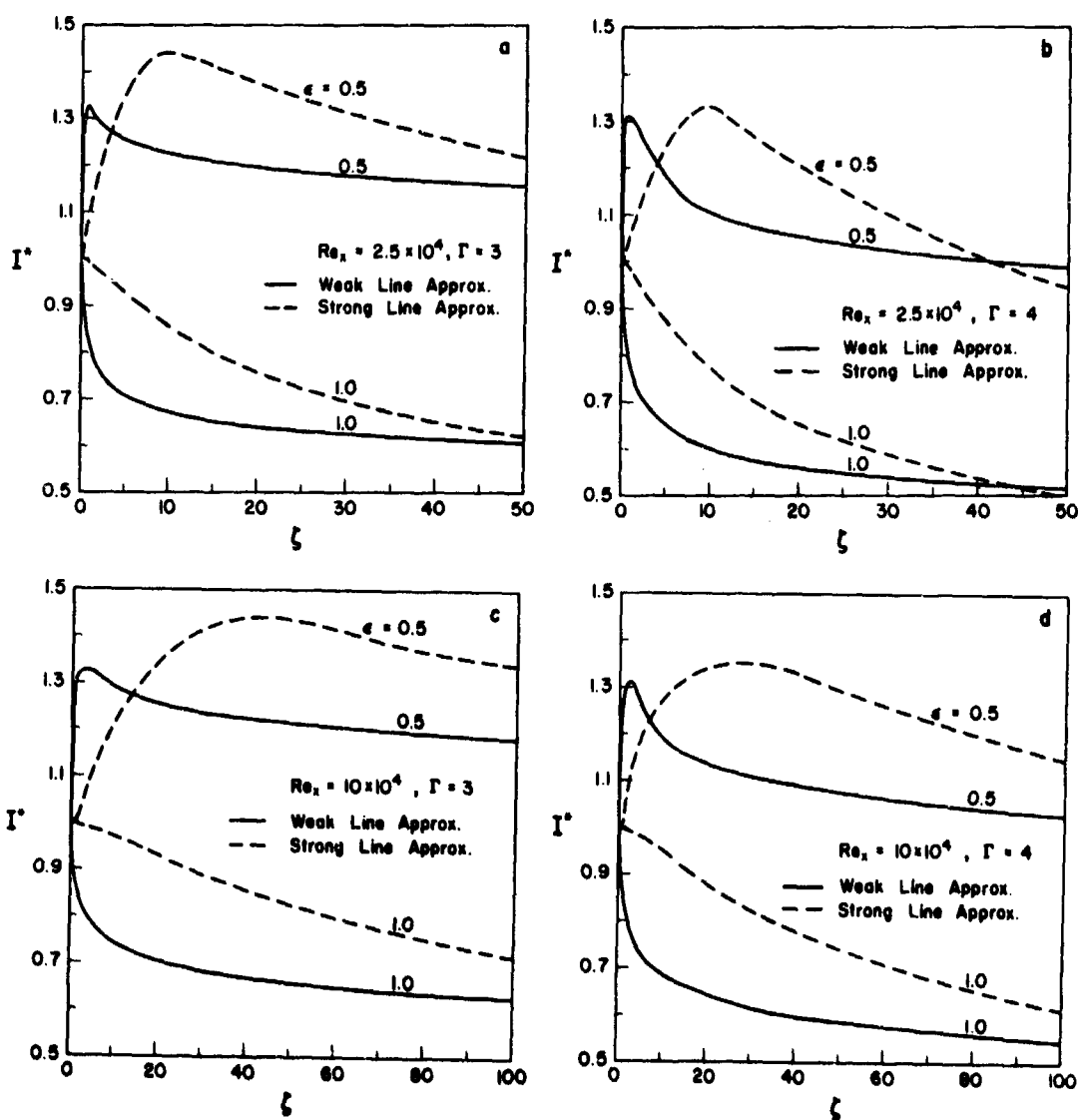


Figure 35. Effect of Injection on the Normalized Emergent Band Intensity;  $x_0 = 0$ ,  $T_\infty = 530^\circ R$

#### 4.3.2 Experimental Results

The development of concentration boundary layers due to mass injection through a cold porous plate is illustrated in Figs. 36 and 37. The effect of injection mass flux  $\rho_w v_w$  with  $u_\infty = 50$  ft/sec is depicted in Figs. 36a and 36b. As expected the boundary layer thickness decreases as the free stream velocity is increased, see Figs. 36a and 36c and Figs. 37a and 37b. The photographs in Fig. 37 show the increase of the boundary layer thickness with decrease in free stream velocity for a constant injection mass flux.

(a)



$$\rho_w v_w = .0167 \text{ lb/ft}^2 \text{ sec}$$
$$u_\infty = 50 \text{ ft/sec}$$

(b)



$$\rho_w v_w = .0067 \text{ lb/ft}^2 \text{ sec}$$
$$u_\infty = 50 \text{ ft/sec}$$

(c)



$$\rho_w v_w = .0067 \text{ lb/ft}^2 \text{ sec}$$
$$u_\infty = 100 \text{ ft/sec}$$

Figure 36. Schlieren Photographs of Boundary Layer Development with CO<sub>2</sub> Injection through a Cold Porous Plate

(a)

$$\rho_w v_w = .0167 \text{ lb/ft}^2\text{sec}$$

$$u_\infty = 100 \text{ ft/sec}$$



(b)

$$\rho_w v_w = .0167 \text{ lb/ft}^2\text{sec}$$

$$u_\infty = 100 \text{ ft/sec}$$



(c)

$$\rho_w v_w = .0167 \text{ lb/ft}^2\text{sec}$$

$$u_\infty = 25 \text{ ft/sec}$$



Figure 37. Schlieren Photographs Illustrating the Effect of Free Stream Velocity on Boundary Layer Development with  $\text{CO}_2$  Injection through a Cold Porous Plate

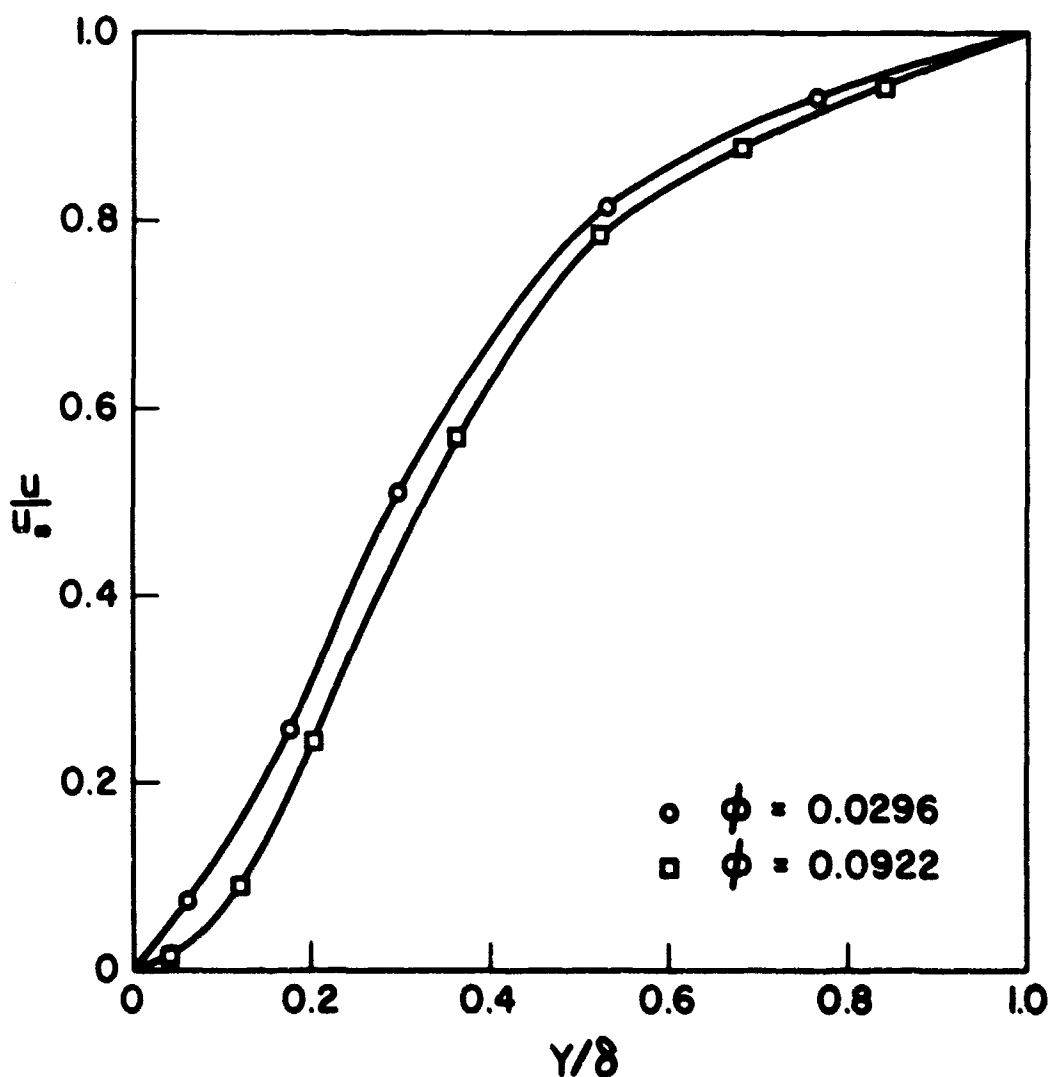


Figure 38. Measured Velocity Profile in the Boundary Layer with  $\text{CO}_2$  Injection through a Heated Porous Plate;  $x_0 = 1$  in,  $x = 2\text{-}1/2$  in,  $\text{Re}_x = 5.75 \times 10^4$ ,  $T_\infty = 530^\circ\text{R}$ ,  $T_w = 1460^\circ\text{R}$

Sample results of the velocity, temperature and mass fraction profiles in the boundary layer are displayed in Figs. 38, 39 and 40, respectively. Because of the probe dimensions and slight vibrations of the wind tunnel to which the probe was attached the closest that the velocity, temperature and concentration could be measured was  $1/16$  in. from the plate. There is some scatter in the data but the trends are consistent. The mass fraction at the wall  $w_w$  could not be measured and the values were obtained by extrapolation. The temperature profiles show expected trends, but the gradients near the wall appear to be high. The large near-isothermal region in the boundary layer is characteristic of turbulent rather than laminar flow even

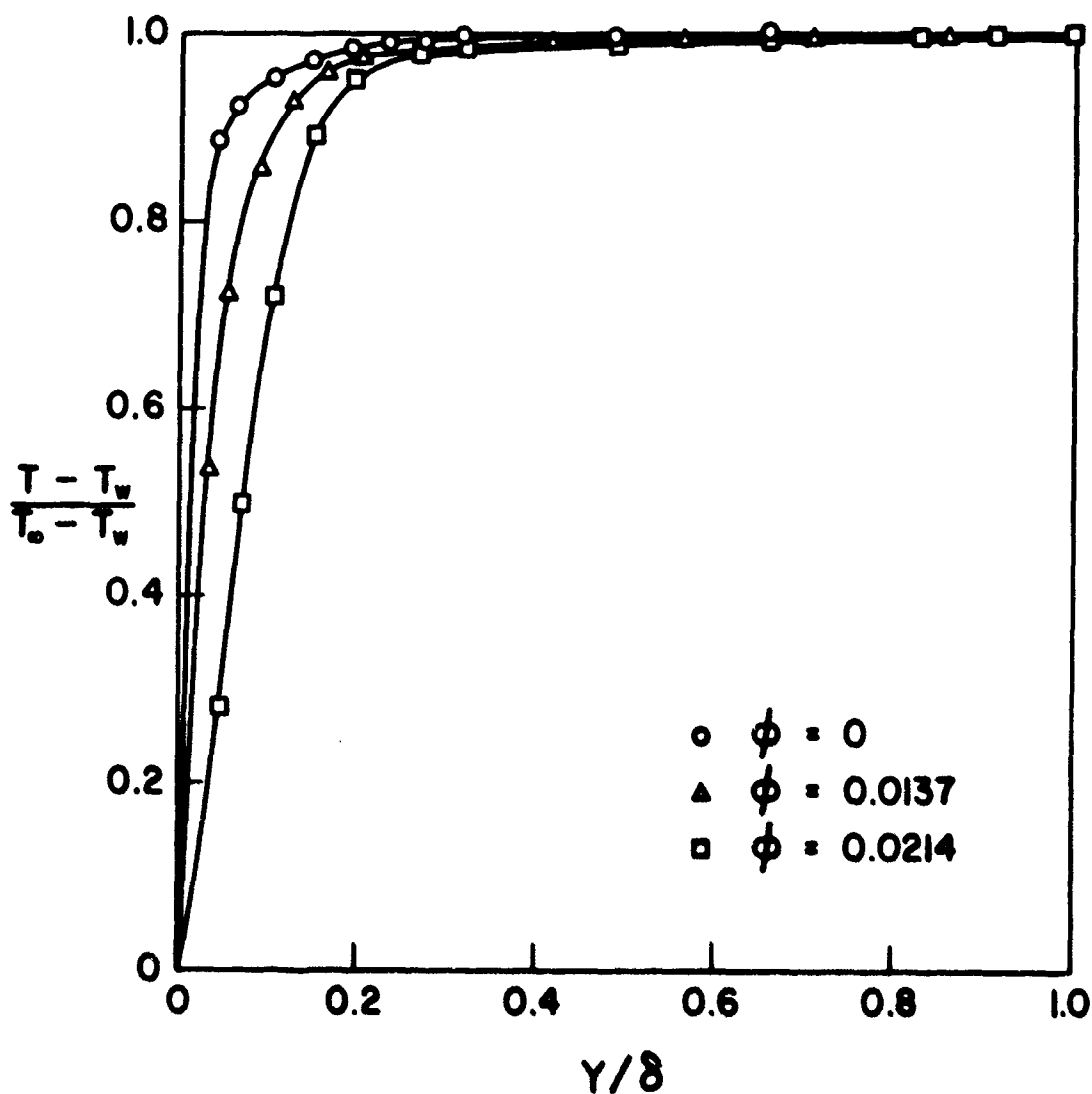


Figure 39. Measured Temperature Profile in the Boundary Layer with  $\text{CO}_2$  Injection through a Heated Porous Plate;  $x_0 = 1$  in,  $x = 2\text{-}1/2$  in,  $\text{Re}_x = 5.75 \times 10^4$ ,  $T_\infty = 530^\circ\text{R}$ ,  $T_w = 1460^\circ\text{R}$

though  $\text{Re}_x$  is considerably smaller than the transition Reynolds number. The boundary layer was also found to be considerably thicker than expected. Some possible reasons for these findings may be the following. The heat exchange effectiveness of the porous plate, i.e., the compactness of the plate, was not high enough to assure that the coolant injected into the stream was at the plate temperature. Heating caused some expansion of the plate which resulted in a small buckling away from the stream, and the joint between the cold solid leading edge and the heated porous plate was not smooth and may have caused turbulence.

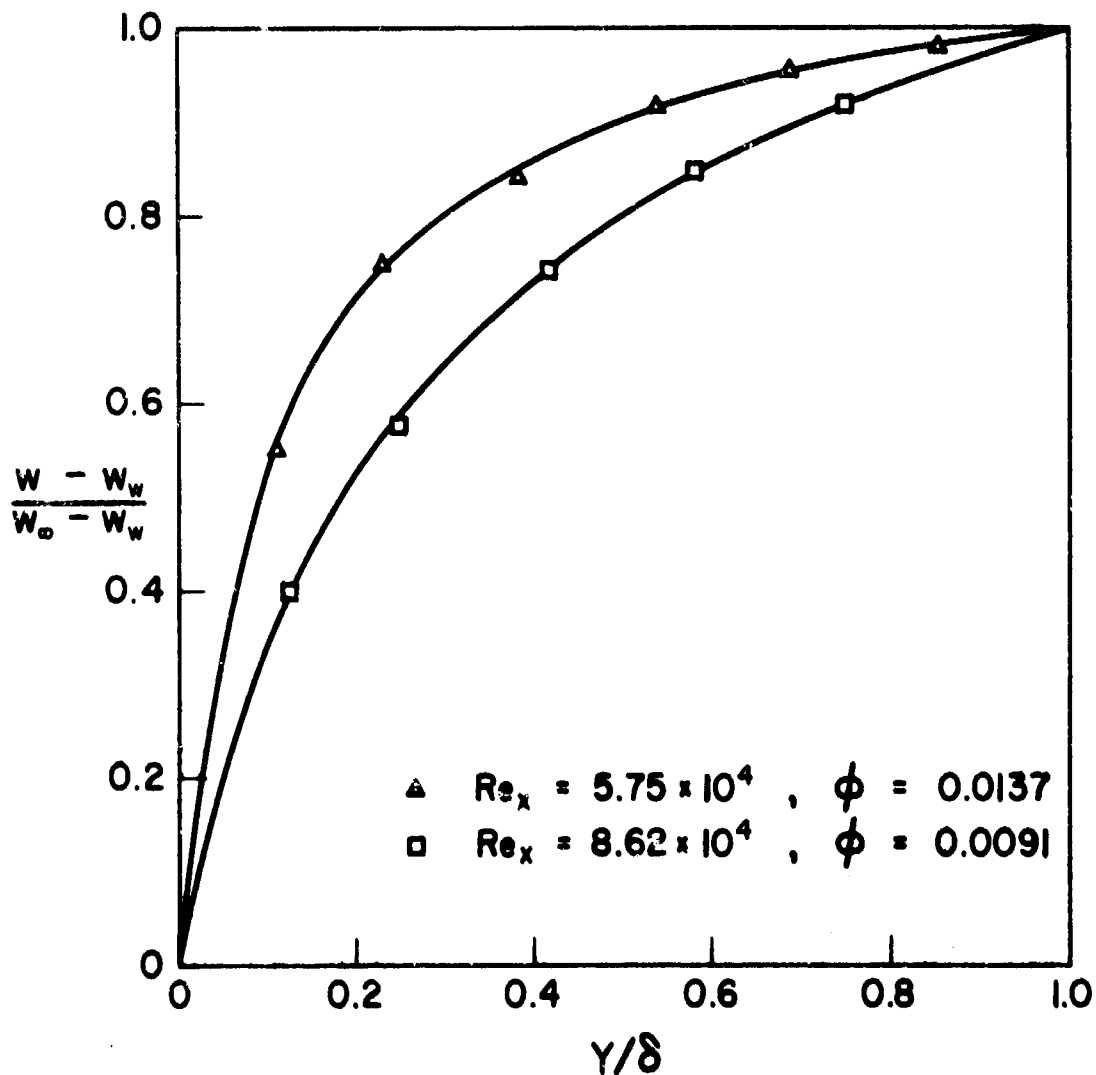


Figure 40. Measured Mass Fraction Profile in the Boundary Layer with  $\text{CO}_2$  Injection through a Heated Porous Plate;  $x_0 = 1$  in,  $x = 2\text{-}1/2$  in,  $T_\infty = 530^\circ\text{R}$ ,  $T_w = 1460^\circ\text{R}$

The normalized band intensities for the case of injection through a porous heated plate having a starting length of  $x_0 = 1$  in. are presented in Table 6 and are plotted in Fig. 41 as a function of  $\zeta$ . Meaningful attenuation results for larger values of injection parameter  $\phi$  could not be obtained because the temperature of the plate became too nonuniform over the area viewed by the radiometer. We note that the measured attenuation at a fixed position along the plate is correlated well by parameter  $\zeta$ . This of course is somewhat surprising since the optical thickness of the boundary layer, Eq. (2.1), is not only a function of the total mass of the absorbing species but also of the concentration and temperature distribution in the boundary

Table 6. Effect of Injected Mass Flux (lbs/ft<sup>2</sup>sec) on Attenuation ( $I^*$ ) for Porous Heated Plate with  $x_0 = 1$  in,  $x = 2\frac{1}{2}$  in,  $T_w \approx 1460^\circ\text{R}$ ,  $\theta = 0^\circ$

$\rho_w v_w \backslash Re_x$	0.050	0.075	0.100
$2.88 \times 10^4$	0.828	0.813	0.795
$5.75 \times 10^4$	0.857	0.821	0.811
$8.62 \times 10^4$	0.864	0.833	0.818

Table 7. Effect of Injected Mass Flux (lbs/ft<sup>2</sup>sec) on Attenuation ( $I^*$ ) for Solid Heated Plate with  $x_0 = 3$  in,  $x = 5$  in,  $T_w \approx 1460^\circ\text{R}$ ,  $\theta = 0^\circ$

$\rho_w v_w \backslash Re_x$	0.033	0.072	0.126	0.224
$2.88 \times 10^4$	0.880	0.800	0.745	0.700
$5.75 \times 10^4$	0.862	0.806	0.746	0.701



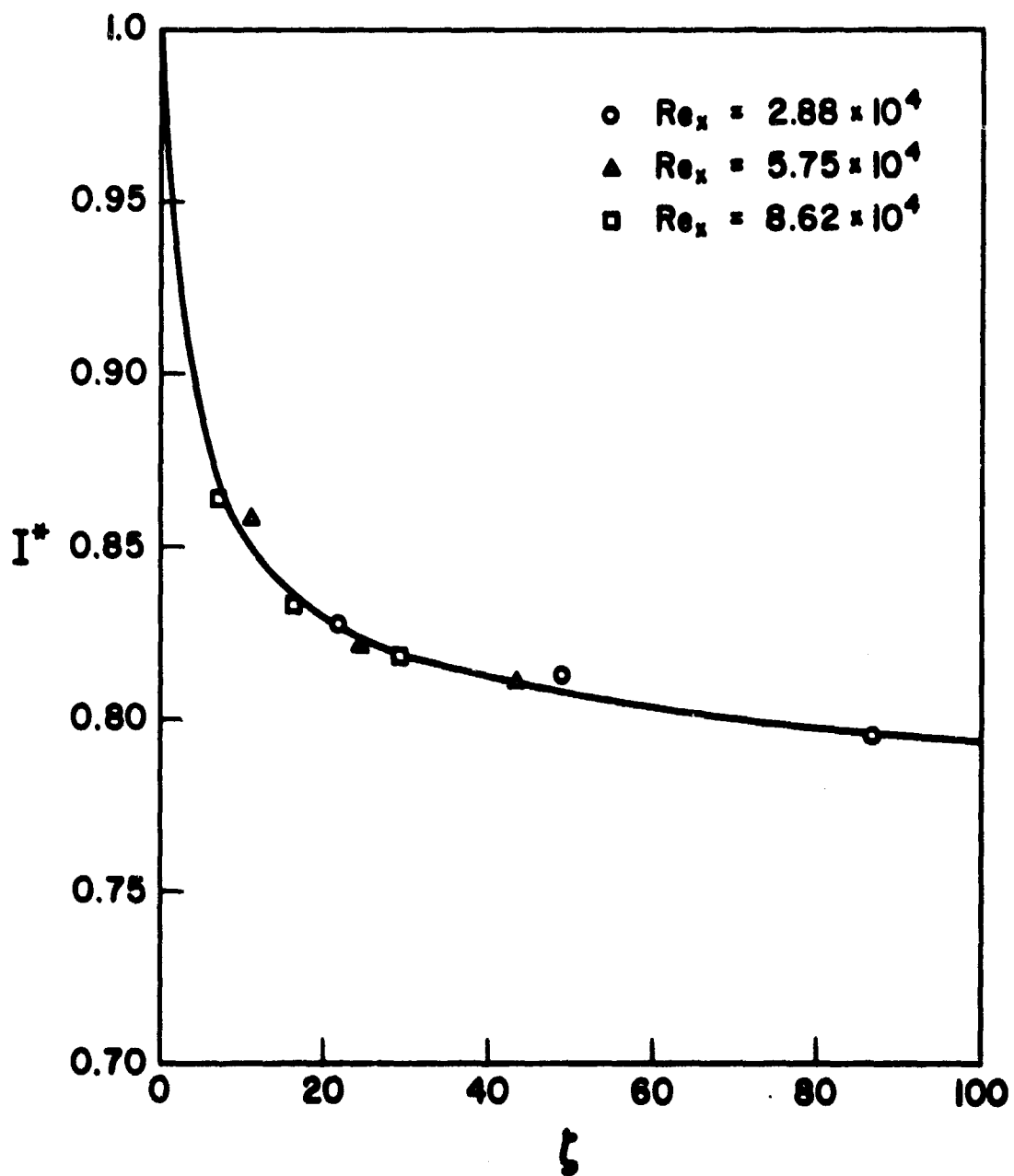


Figure 41. Effect of  $CO_2$  Injection on Measured Band Attenuation with a Heated Porous Plate;  $x_0 = 1$  in,  $x = 2-1/2$  in,  $T_\infty = 530^\circ R$ ,  $T_w = 1460^\circ R$

layer. The results for the normalized band intensity for injection through a cold porous plate joined to a solid heated plate having a starting length of  $x_0 = 3$  in. are presented in Table 7 and are plotted in Fig. 42. In this case the data are not correlated as well against the parameter  $\zeta$ . The results of both Figs. 41 and 42 show that for a given injection parameter  $\phi$  the effect of increasing local Reynolds number is to increase the attenuation, but the effect is small. The reason for this is that for a given blowing rate the mass of  $\text{CO}_2$  in the boundary layer increases with  $\text{Re}_x$ .

#### 4.3.3 Comparison of Analysis and Experiment

A comparison of predicted and measured temperature profiles is shown in Fig. 43. The measured temperature gradients in the vicinity of the porous plate were higher than those predicted, and the measured boundary layer thickness was much thicker than the calculated one. It is clear from the figure that the mathematical equations did not properly model the physical phenomenon. A cause for higher temperature gradients in the vicinity of the surface is believed to be the effectiveness of the Poroloy plate which was not sufficiently large enough resulting in the coolant being injected into the stream at a lower temperature than the plate. Measured boundary layers were thicker than those predicted since the Poroloy plate used was not compact enough, and the  $\text{CO}_2$  was injected into the main stream through a large number of small holes rather than uniformly. The injected mass flux  $\rho_w V_w$  was based on the total area rather than area of the pores. Based on an unoxidized plate the latter was estimated to be about a factor of 25 times smaller. The pore area of an oxidized plate was even smaller. The velocity of the  $\text{CO}_2$  gas emanating from the pores based on the actual pore area was estimated to be high, i.e., in the range from 15 to 60 percent of the free stream velocity. Hence it is justifiable to say that  $\text{CO}_2$  was injected into the boundary layer through a large number of discrete holes and the flow was not uniform but formed a large number of small interacting jets. These jets entered the stream at an angle of about  $45^\circ$ . As the emerging jet of hot  $\text{CO}_2$  gas enters the stream it dissipates, spreads, mixes with the gas in the boundary layer and its momentum carries the injected species further away from the plate. This thickens the boundary layer and may even cause it to become completely turbulent. The injection could have possibly made the boundary layer unstable and increased its thickness considerably beyond what is predicted by the analysis.

The predicted mass fraction distributions differ appreciably from the measured ones. The analytical profiles for the conditions shown in Fig. 44 were very close and two separate curves could not be drawn. Again, the measured concentration boundary layer thickness is much larger than the calculated one. This discrepancy is believed to be the same as for the thermal boundary layer.

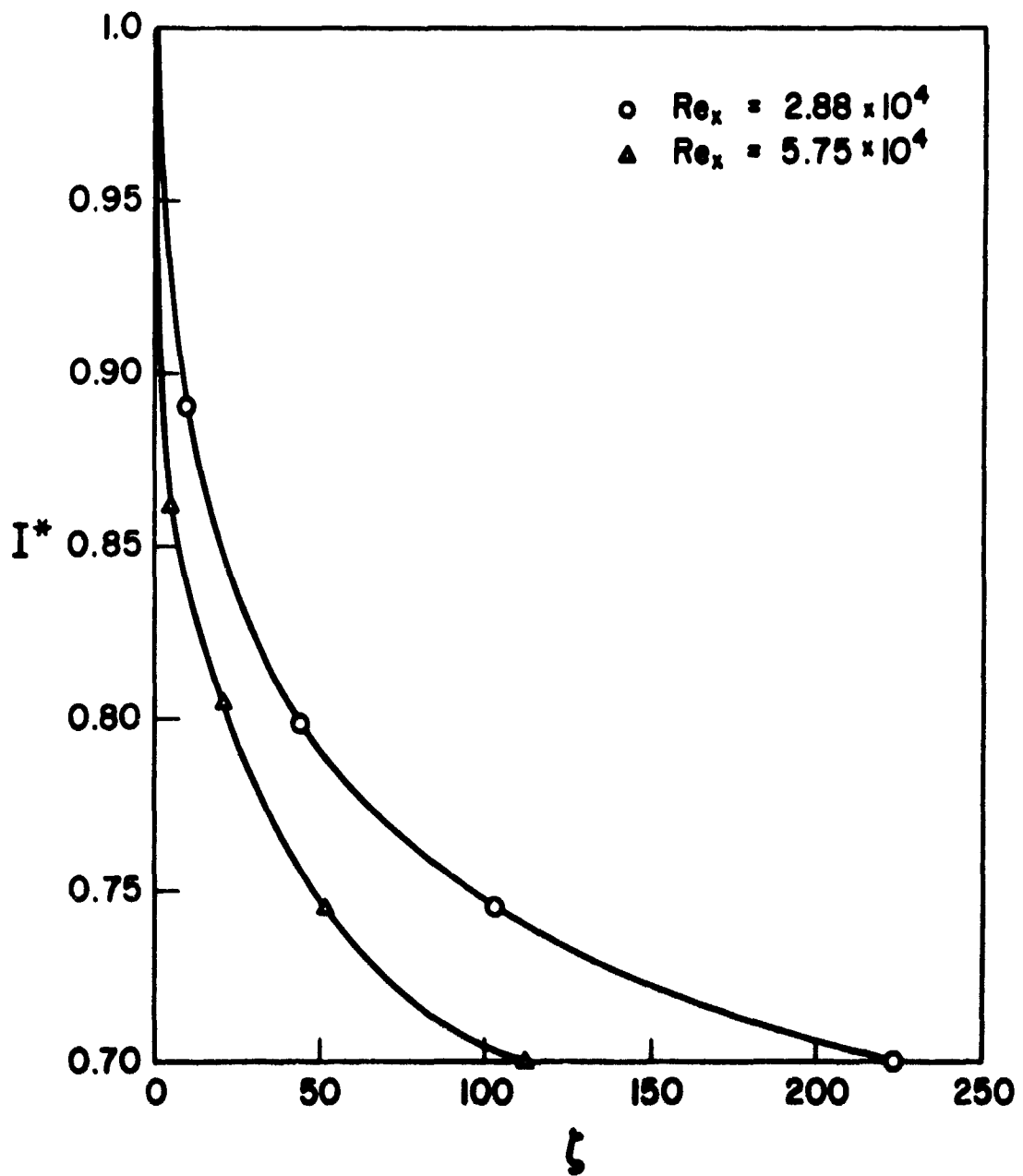


Figure 42. Effect of  $CO_2$  Injection through a Cold Porous Leading Edge on Measured Band Attenuation with a Solid Heated Plate;  $x_0 = 3$  in,  $x = 5$  in,  $T_\infty = 530^\circ R$ ,  $T_w = 1460^\circ R$

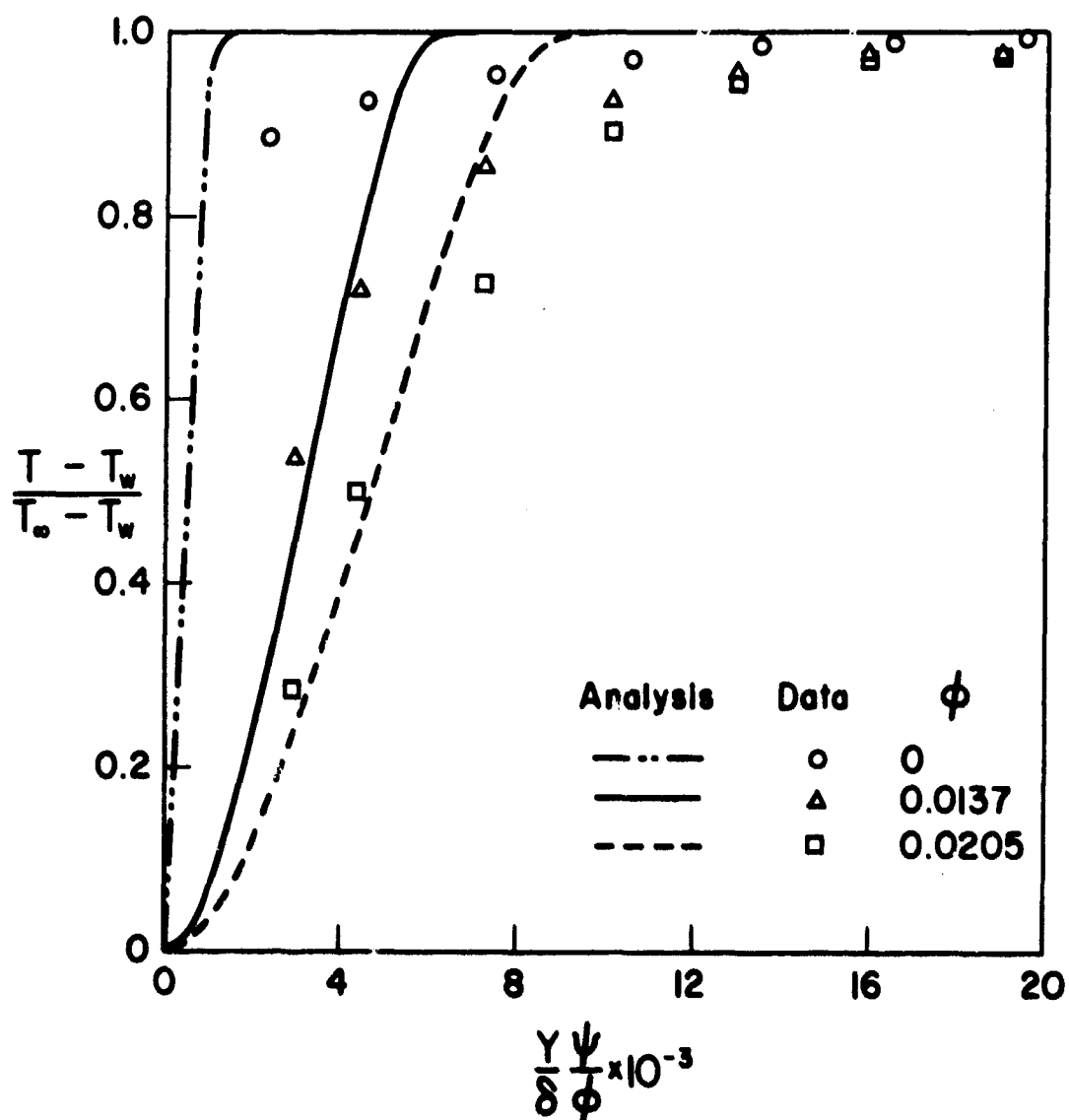


Figure 43. Comparison between Analysis and Experiment of Temperature Profiles in the Boundary Layer with  $\text{CO}_2$  Injection through a Heated Porous Plate;  $x_0 = 1$  in,  $x = 2\text{-}1/2$  in,  $\text{Re}_x = 5.75 \times 10^4$ ,  $T_\infty = 530^\circ\text{R}$ ,  $T_w = 1460^\circ\text{R}$

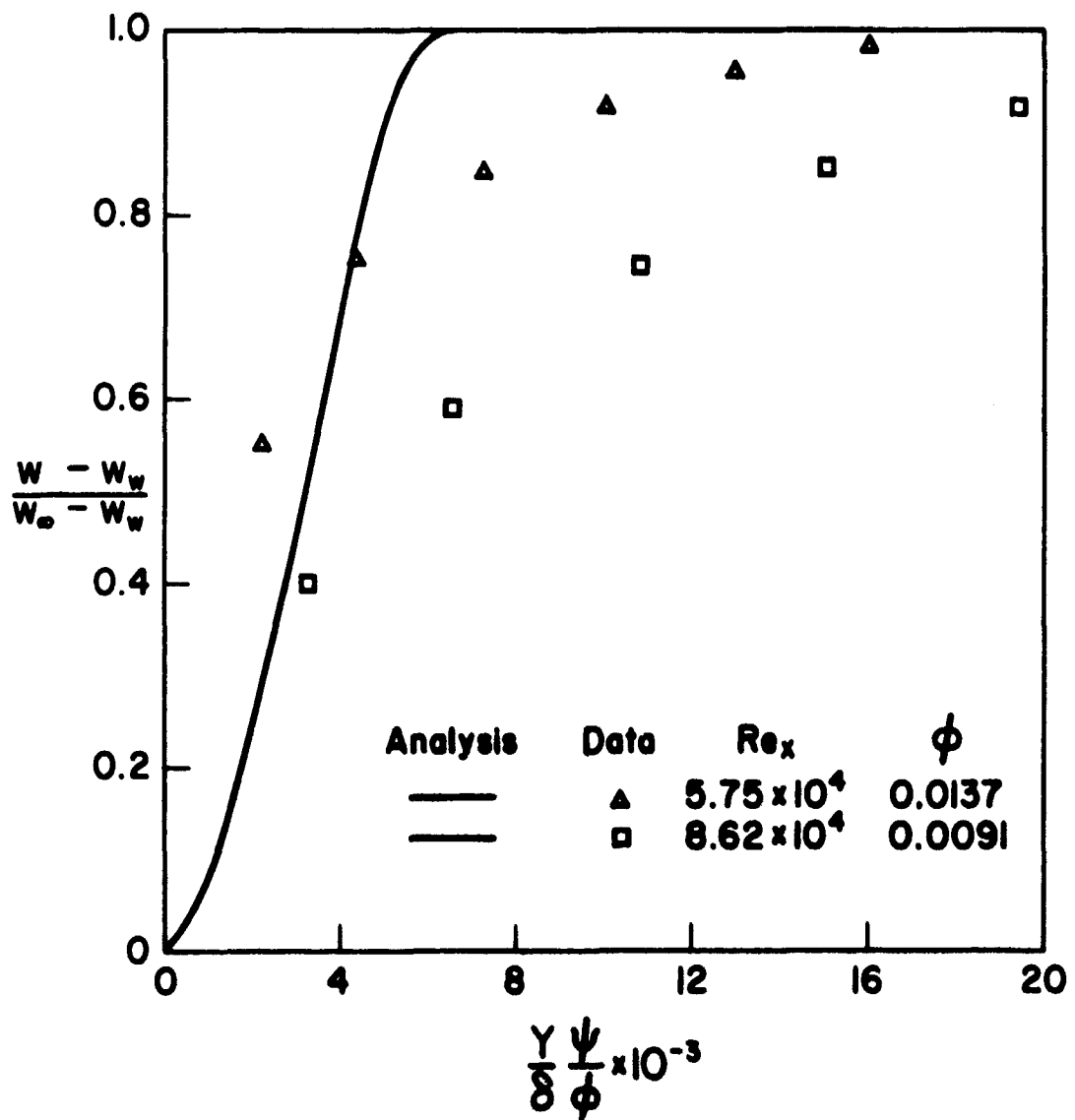


Figure 44. Comparison between Analysis and Experiment of Mass Fraction Profiles in the Boundary Layer with  $CO_2$  Injection through a Heated Porous Plate;  $x_0 = 1$  in,  $x = 2-1/2$  in,  $T_\infty = 530^\circ R$ ,  $T_w = 1460^\circ R$

A comparison of measured and predicted attenuation is shown in Fig. 45. The predicted  $I^*$  is based on a plate emissivity of 0.7. This is a few percent higher than the results of Fig. 23 indicate at  $\lambda = 4.3\mu$  for a less porous plate. This somewhat higher value is justified because of the larger cavity effect of the more porous Poroloy plate. The predicted attenuation was also corrected for the transmission of the filter, Fig. 13. This correction, however, increased  $I^*$  only by less than one percent from the value predicted without the filter. As in the case of the near stagnant layer and other investigators [43, 60] the measured attenuation is slightly larger than the predicted but the trends are in agreement.

The prediction of the absorptivity of a nonisothermal gas has been the subject of much current research effort [43, 60-65]. Detailed calculations using the Curtis-Godson [61, 62] or box model [63] have been made to predict the spectral absorptivity and the Curtis-Godson approximation has been used to predict nonisothermal total band absorptance [43, 64, 65]. Agreement between predicted and observed results ranges from 20% [60] to less than 10% [62, 63, 64]. On this basis the comparison of the analytical with the experimental results of this investigation are considered relatively good.

As Fig. 34 shows, the center of the band is not yet opaque, hence the weak-line is the more appropriate approximation. This is in agreement with the observed results. There is uncertainty in the emissivity as it was impossible to measure the values of the spectral emissivity in situ. As has been shown an error of 10% in the emissivity has a considerable effect on the value of attenuation predicted. Also, the discrepancy between the predicted and measured temperature and  $\text{CO}_2$  concentration profiles would be reflected in the optical thickness of the layer as well as Planck's function. The larger measured than predicted values of attenuation  $I^*$  are consistent with the measured concentration boundary layers being thicker than those predicted.

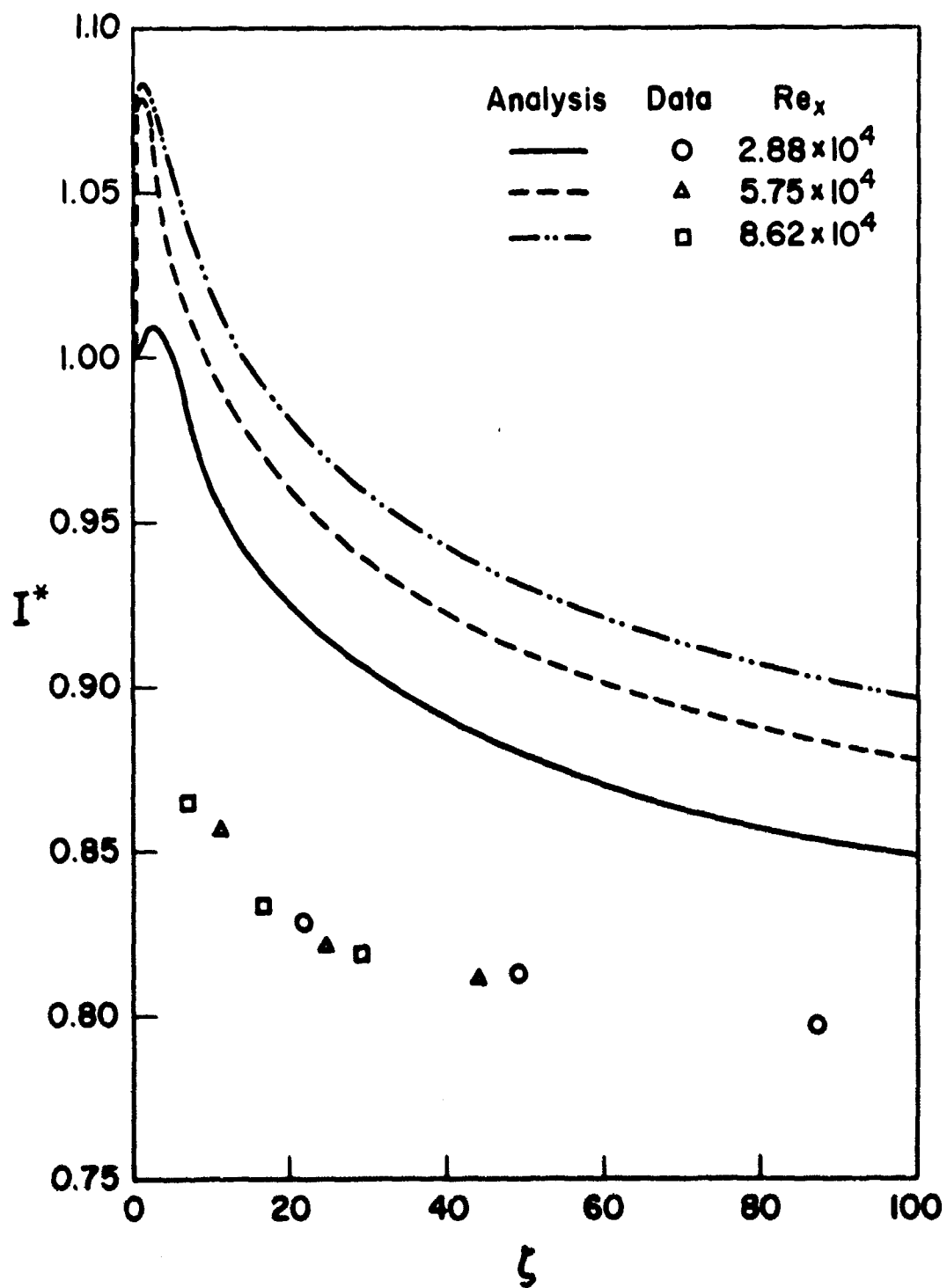


Figure 45. Comparison between Analysis and Experiment of Normalized Band Attenuation with  $CO_2$  Injection through a Porous Heated Plate;  $x_0 = 1$  in,  $x = 2-1/2$  in,  $T_\infty = 530^\circ R$ ,  $T_w = 1460^\circ R$ ,  $\epsilon = 0.7$

## 5. CONCLUSIONS AND RECOMMENDATIONS

In this section conclusions and recommendations are presented which are based on analyses and somewhat limited measurements of preliminary nature conducted in assessing the effectiveness of an absorbing gas in attenuating infrared radiation emitted from hot surfaces.

An apparatus for the investigation of attenuation of infrared radiation emitted from a hot porous surface through which an absorbing-emitting gas was transpired was designed and constructed. Instrumentation and measurement techniques were developed for the determination of attenuation, flow and state variables in a near stagnant layer of gas and boundary layer flow over a surface. In a parallel study analyses were performed to predict the attenuation.

Specifically, carbon dioxide was transpired through a porous (Poroloy) plate into a near stagnant layer of air and the attenuation of radiation measured in the  $4.3\mu$  band. The effects of the injected mass flow rate, plate temperature, gas layer thickness and angle of observation were investigated and it was found that  $\text{CO}_2$  attenuated between 54 and 44 percent of radiation in the wavelength band studied. Although the analysis did not completely simulate the experimental conditions it nevertheless predicted the experimentally observed trends correctly.

The velocity, temperature and concentration distributions in a boundary layer over a flat plate under specified free stream and injection conditions were measured and were in poor agreement with predictions based on an approximate integral method of solution of the conservation equations. The attenuation of infrared radiation for some conditions reached up to 30%. The analytical predictions were in qualitative agreement with experimental results.

Based on the results obtained for the near stagnant gas and the gas flow situations it can be concluded that in a specified wavelength range the radiation can be significantly attenuated, provided the participating gas or gas mixture strongly absorbs radiation in this region. At high free stream velocities the transpiration of an absorbing gas into a boundary layer may not be sufficiently effective to produce the desired attenuation. In order to enhance attenuation under these conditions particulate matter and/or strongly absorbing gases, such as metal vapors could be employed.



Although the feasibility of the attenuation technique has been demonstrated, a number of problem areas remain and should be further explored. In particular it is recommended that the following work be done:

1. Transpiration cooling studies should be extended to situations where the coolant is injected into the boundary layer through discrete holes in a porous structure (such as Poroloy) instead of uniformly to determine the fluid flow and heat transfer characteristics of the boundary layer as well as of the heat exchange effectiveness of the material.
2. An improved experimental apparatus and instrumentation should be developed with which a much wider range of experimental conditions, geometries and injected fluids can be investigated.
3. Since data on the spectral absorption characteristics of gases or gas mixtures as a function of pressure and temperature are very limited these data should be acquired. Especially it is recommended that the properties of mixtures of gases and particulate matter be studied.
4. Measurement of the attenuation of radiation on a spectral bases in nonhomogeneous media in which large temperature gradients prevail should be performed.

## 6. REFERENCES

1. R. Viskanta, Radiation Transfer and Interaction of Convection with Radiation Heat Transfer, in Advances in Heat Transfer, (T. F. Irvine, Jr. and J. P. Hartnett, Eds.), Vol. 3, pp. 175-251, Academic Press, New York (1966).
2. S. S. Penner, Quantitative Molecular Spectroscopy and Gas Emissivities, Addison-Wesley, Reading, Mass. (1959).
3. C. L. Tien, "Thermal Radiation of Gases," in Advances in Heat Transfer (T. F. Irvine, Jr. and J. P. Hartnett, Eds.), Vol. 5, pp. 253-324, Academic Press, New York (1968).
4. F. H. Howard, J. L. Novotny and K. T. Yang, "Infrared Radiative Heat Transfer in Gases, An Annotated Bibliography," Technical Report No: THEMIS-UND-69-9, University of Notre Dame, September 1969 (AD 699873).
5. Wm. L. Wolfe, Handbook of Military Infrared Technology, Office of Naval Research, Department of the Navy, Washington, D. C. (1965).
6. R. H. Pierson, A. N. Fletcher, and E. S. Gantz, "Catalog of Infrared Spectra for Qualitative Analysis of Gases," Analytical Chemistry 28, 1218 (1956).
7. N. Sax, Dangerous Properties of Industrial Materials, 3rd Edition, Reinhold Book Corp., New York (1968).
8. J. F. Gross, J. P. Hartnett and C. Gazley, Jr., "A Review of Binary Laminar Boundary Layer Characteristics," Int. J. Heat Mass Transfer 3, 198 (1961).
9. D. A. Nealy, "An Approximate Treatment of Heat Transfer in Plane Laminar and Turbulent Flows Over Arbitrary Surfaces with Arbitrary Surface Injection--Including Wall Effects," Ph.D. Thesis, Purdue University (1968).
10. E. M. Sparrow and R. D. Cess, Radiation Heat Transfer, Brooks/Cole Publishing Co., Belmont, Calif. (1966).
11. R. Viskanta and R. L. Merriam, "Shielding of Surfaces in Couette Flow Against Radiation by Transpiration of an Absorbing-Emitting Gas," Int. J. Heat Mass Transfer 10, 641 (1967).

12. J. L. Novotny, Y. Taitel and J. P. Hartnett, "Mass Transfer Cooling in High Speed Couette Flow of an Absorbing-Emitting Gas" in Proceedings of the 1965 Heat Transfer and Fluid Mechanics Institute, (A. F. Charwart, Editor), pp. 70-86, Stanford University Press, Stanford, California (1965).
13. J. L. Novotny, Y. Taitel and J. P. Hartnett, "Equilibrium Temperature of Mass Transfer Cooled Walls in High Speed Flow of an Absorbing-Emitting Gas," Vol. 5, pp. 138-145, in Proceedings of the Third International Heat Transfer Conference, ATChE, New York (1966).
14. R. D. Cess, "Radiation Effects Upon Boundary Layer Flow of an Absorbing Gas," Trans. ASME, Series C, J. Heat Transfer 86, 469 (1964).
15. C. C. Oliver and P. W. McFadden, "The Interaction of Radiation and Convection in the Laminar Boundary Layer," Trans. ASME, Series C, J. Heat Transfer 88, 205 (1966).
16. H. R. Jacobs, "Radiation Absorption in High-Speed Laminar Boundary Layers Including the Effects of External Sources," AIAA Journal 5, 1337 (1967).
17. Y. Taitel and J. P. Hartnett, "Equilibrium Temperatures in a Boundary-Layer Flow Over a Flat Plate of Absorbing-Emitting Gas," Trans. ASME, Series C, J. Heat Transfer 90, 257 (1968).
18. L. A. Kennedy, "The Effects of Mass Addition on the Laminar Boundary Layer Flow of Absorbing-Emitting Gas," Int. J. Heat Mass Transfer 11, 775 (1968).
19. N. A. Macken and J. P. Hartnett, "Interaction of Convection and Radiation in Axisymmetric and Two-Dimensional Stagnation Point Flow," in Proceedings of the 1967 Heat Transfer and Fluid Mechanics Institute (P. A. Libby, et al., Eds.), pp. 115-140, Stanford University Press, Stanford, Calif. (1967).
20. J. T. Howe and J. R. Viegas, "Solutions of the Ionized Radiating Shock Layer, Including Reabsorption and Foreign Species Effects and Stagnation Region Heat Transfer," NASA TR R-159 (1963).
21. J. T. Howe and Y. S. Sheaffer, "Mass Addition in the Stagnation Region for Velocity up to 50,000 Feet per Second," NASA TR R-207 (1964).
22. R. D. Cess, P. Mighdoll and S. N. Tiwari, "Infrared Radiant Heat Transfer in Nongray Gases," Int. J. Heat Mass Transfer 10, 1521 (1967).

23. R. D. Cess and S. N. Tiwari, "The Effect of Surface Emissivity upon Infrared Gaseous Radiation," Int. J. Heat Mass Transfer 11, 1731 (1968).
24. R. Grief and I. J. Habib, "Infrared Radiation Transport: Exact and Approximate Results," Trans. ASME, Series C, J. Heat Transfer 91, 282 (1969).
25. J. L. Novotny, "Radiation Interaction in Non-Gray Boundary Layers," Int. J. Heat Mass Transfer 11, 1823 (1968).
26. W. P. Schimmel, J. L. Novotny and S. Kast, "Effect of Surface Emittance and Approximate Kernels in Radiation-Conduction Interaction," Wärme-und Stoffübertragung 3, 1 (1970).
27. A. M. Smith and H. A. Hassan, "Nongrey Radiation Effects on the Boundary Layer at Low Eckert Numbers," ASME Paper No. 66-WA/HT-35.
28. W. S. Rigdon, R. B. Dirling, Jr. and M. Thomas, "Stagnation Point Heat Transfer During Hypervelocity Atmospheric Entry," McDonnell Douglas Astronautics Co. Report DAC-63243, July 1969.
29. W. B. Olstad, "Nongray Radiating Flow About a Smooth Symmetric Bodies with Large Blowing," AIAA Paper No. 69-637.
30. J. Gille and R. M. Goody, "Convection in a Radiating Gas," J. Fluid Mech. 20, 47 (1964).
31. J. L. Novotny and F. A. Olsofka, "The Influence of a Non-Absorbing Gas in Radiation-Conduction Interaction," AIAA Paper No. 70-836 (1970).
32. E. M. Sparrow, W. J. Minkowycz, E. R. G. Eckert and W. E. Ibele, "The Effect of Diffusion Thermo and Thermal Diffusion for Helium Injection into Plane and Axisymmetric Stagnation Flow of Air," Trans. ASME, Series C, Heat Transfer 86, 311 (1964).
33. J. P. Chiou and M. M. El-Wakil, "Heat Transfer and Flow Characteristics of Porous Matrices with Radiation as a Heat Source," Trans. ASME, Series C, J. Heat Transfer 88, 69 (1966).
34. D. K. Edwards and W. A. Menard, "Comparison of Models for Correlation of Total Band Absorption," Applied Optics 3, 621 (1964).
35. C. L. Tien and J. E. Lowder, "A Correlation for Total Band Absorption of Radiating Gases," Int. J. Heat Mass Transfer 9, 698 (1966).

36. W. A. Vincenti and B. S. Baldwin, Jr., "Effect of Thermal Radiation on the Propagation of Plane Accoustic Waves," J. Fluid Mech. 12, 449 (1962).
37. S. S. R. Murty, "Approximations on Angular Distribution of Intensity of Thermal Radiation," Int. J. Heat Mass Transfer 8, 1203 (1965).
38. J. A. Jamieson, R. H. McFee, R. H. Grube and R. G. Richards, Infrared Physics and Engineering, McGraw-Hill, New York (1963).
39. F. E. Nicodemus, "Calibration Techniques for Radiometers," Lecture 16 in Precision Radiometry - Calibration and Instrumentation, Univ. of Michigan Engineering Summer Conferences, Univ. of Michigan, Ann Arbor (1965).
40. F. S. Simmons, "Band Models for Nonisothermal Radiation Gases," Appl. Optics 5, 1801 (1966).
41. S. H. Chan and C. L. Tien, "Infrared Properties of Sulfur Dioxide," J. Quant. Spectrosc. Radiat. Transfer (in press).
42. TRW Systems, Inc., Redondo Beach, Calif. (1969) (personal communication).
43. S. H. Chan and C. L. Tien, "Total Band Absorptance of Non-isothermal Infrared-Radiation Gases," J. Quant. Spectrosc. Radiat. Transfer 9, 1261 (1969).
44. R. B. Bird, W. E. Stewart and E. N. Lightfoot, Transport Phenomenon, Wiley, New York (1960).
45. E. S. Mazanek, Jr., "Grey and Nongrey Interaction Effects in the Self-Absorbing Boundary Layer on a Flat Plate," Ph.D. Thesis, Purdue University (1968).
46. R. W. Crossley, "The Effects of Radiation on Temperature and Heat Transfer in Laminar Boundary Layer Flow Over a Flat Plate," Ph.D. Thesis, Purdue University (1967).
47. P. A. Libby and A. Pallone, "A Method for Analyzing the Heat Insulating Properties of the Laminar Compressible Boundary Layer," J. Aerospace Sci. 21, 825 (1954).
48. P. A. Libby and M. A. Morduchov, "A Method for Calculation of the Compressible Laminar Boundary Layer with Axial Pressure Gradient and Heat Transfer," NACA TN 3157 (1954).
49. S. W. Yuan, "Heat Transfer in a Laminar Boundary Layer on a Partially Sweat Cooled Plate," Project SQUID Report PlB-19R, Polytechnic Institute of Brooklyn (1949).

50. H. Schlichting, Boundary Layer Theory, 6th Ed., McGraw-Hill, New York (1968), p. 192.
51. W. Malkmus, "Infrared Emissivity of Carbon Dioxide (4.3 $\mu$  Band)," J. Opt. Soc. 53, 951 (1963).
52. G. N. Plass, "Models for Spectral Band Absorption," J. Opt. Soc. Am. 48, 690 (1968).
53. Y. Ben-Aryeh, "Spectral Emissivity Calculations by the Statistical Model Applied to the 4.3 $\mu$  Bands of CO<sub>2</sub> at High Temperatures," Appl. Optics 6, 1049 (1969).
54. L. D. Gray, "Spectral Emissivity Calculations for the Parallel Bands of Carbon Dioxide at 4.3 Microns," J. Quant. Spectrosc. Radiat. Transfer 5, 569 (1965).
55. R. H. Tourin, "Measurements of Infrared Spectral Emissivities of Hot Carbon Dioxide in the 4.3- $\mu$  Region," J. Opt. Soc. Am. 51, 175 (1961).
56. R. W. Landenberg (Editor), Physical Measurements in Gas Dynamics and Combustion, Princeton University Press, Princeton, N. J. (1954).
57. E. Heftmann, Chromatography, Reinhold Publishing Co., New York (1961).
58. S. W. Yuan, "Heat Transfer in Laminar Compressible Boundary Layer on a Porous Flat Plate with Fluid Injection," J. Aerospace Sci. 16, 741 (1949).
59. N. Ness, "On the Temperature Distribution Along a Semi-Infinite Swept Cooled Plate," J. Aerospace Sci. 19, 760 (1952).
60. D. K. Edwards, L. K. Glassen, W. C. Hauser and J. S. Tuchscher, "Radiation Heat Transfer in Nonisothermal Nongray Gases," Trans. ASME, Series C, J. Heat Transfer 89, 219 (1967).
61. F. S. Simmons, "Band Models for Nonisothermal Radiating Gases," Appl. Optics 5, 1801 (1966).
62. M. M. Weiner and D. K. Edwards, "Non-isothermal Gas Radiation in Superposed Vibration-Rotation Bands," J. Quant. Spectrosc. Radiat. Transfer 8, 1171 (1968).
63. S. S. Penner and O. P. Sharma, "Procedures for Approximate Calculations of Radiant-Energy Emission from Non-isothermal Molecular Emitters," Proceedings of the Fourth Symposium on Thermophysical Properties, ASME, New York (1968), pp. 9-20.

64. D. K. Edwards and S. J. Morizumi, "Scaling of Vibration-Rotation Band Parameters for Nonhomogeneous Gas Radiation," J. Quant. Spectrosc. Radiat. Transfer 10, 175 (1970).
65. R. D. Cess and L. S. Wang, "A Band Absorptance Formulation for Nonisothermal Gaseous Radiation," Int. J. Heat Mass Transfer 13, 547, (1970).

UNCLASSIFIED

Security Classification

DOCUMENT CONTROL DATA - R & D		
(Security classification of title, body of abstract and indexing annotation must be entered when the overall report is classified)		
1. ORIGINATING ACTIVITY (Corporate author) Heat Transfer Laboratory School of Mechanical Engineering Purdue University, Lafayette, Indiana		2a. REPORT SECURITY CLASSIFICATION UNCLASSIFIED
		2b. GROUP
3. REPORT TITLE Attenuation of Infrared Radiation Emitted from Hot Surfaces by Transpiration of Absorbing Gas		
4. DESCRIPTIVE NOTES (Type of report and inclusive dates) FINAL REPORT (3 September 1968 - 31 August 1970)		
5. AUTHOR(S) (First name, middle initial, last name) David H. Quick, Captain, USAF Robert W. Bergstrom, Jr. Edward E. Anderson, et al.		
6. REPORT DATE September 1970	7a. TOTAL NO. OF PAGES 94	7b. NO. OF REF. 65
8a. CONTRACT OR GRANT NO. F 33615-68-C-1642	9a. ORIGINATOR'S REPORT NUMBER(S) AFAPL-TR-70-60	
b. PROJECT NO. 3066		
c. Task No. 306606	9b. OTHER REPORT NO(S) (Any other numbers that may be assigned this report)	
10. DISTRIBUTION STATEMENT This document is subject to special export controls and each transmittal to foreign governments or foreign nationals may be made only with prior approval of the Air Force Aero Propulsion Laboratory (APTC), Wright-Patterson Air Force Base, Ohio.		
11. SUPPLEMENTARY NOTES	12. SPONSORING MILITARY ACTIVITY Air Force Aero Propulsion Laboratory Wright-Patterson Air Force Base Ohio 45433	
13. ABSTRACT Analyses and measurements of attenuation of thermal radiation leaving a heated plate caused by a layer of absorbing gas are discussed. Both a near stagnant fluid and flow over a flat plate were investigated by analysis and experiment. An apparatus in which various porous plates were heated electrically was designed and constructed so that it could be adopted to either the stagnant or flow systems. Radiant energy fluxes in specified wavelength bands leaving the plate were measured with an infrared radiometer developed and built for this purpose.  Specifically, radiometric measurements for the $4.3\mu$ band of carbon dioxide were made for various plate surface temperatures, injection rates, thicknesses of the absorbing gas layer and viewing angles. In addition to the above parameters the Reynolds number was varied and the effect of the starting length investigated for flow over a flat plate. It was found that the gas is capable of attenuating a significant fraction of the radiation leaving the hot plate. Increases in the plate temperature and gas layer thickness increased the attenuation. For a given mass injection rate of an absorbing gas the attenuation increased with an increase with the Reynolds number. The analyses and experiments show that in order to obtain significant attenuation over large spectral regions a mixture of selected gases or gas-particulate mixtures would have to be injected.		

DD FORM 1473

UNCLASSIFIED

Security Classification



UNCLASSIFIED

Security Classification

14. KEY WORDS	LINK A		LINK B		LINK C	
	ROLE	WT	ROLE	WT	ROLE	WT
1. Attenuation of infrared radiation 2. Boundary layer flow of radiating gas 3. Interaction of convection and radiation 4. Radiating gases 5. Thermal radiation transfer 6. Transpiration cooling						

UNCLASSIFIED

Security Classification